Measuring the Environmental Dependence of Galaxy Haloes with Weak Lensing

by

Bryan Gillis

A thesis
presented to the University of Waterloo
in fulfilment of the
thesis requirement for the degree of
Doctor of Philosophy
in
Physics

Waterloo, Ontario, Canada, 2013

Author's declaration

I hereby declare that I am the sole author of this thesis. This is a true copy of the thesis, including any required final revisions, as accepted by my examiners.

I understand that my thesis may be made electronically available to the public.

Abstract

We investigate the uses of gravitational lensing for analysing the dark matter haloes around galaxies, comparing galaxies within groups and clusters to those in the field. We consider two cases: when only photometric redshift data is available, and when spectroscopic redshift data is available for a sufficiently large sample of galaxies.

For the case of data with photometric redshifts, we analyse the CFHTLenS dataset. This dataset is derived from the CFHTLS-Wide survey, and encompasses 154 deg^2 of high-quality shape data. Using the photometric redshifts to estimate local density, we divide the sample of lens galaxies with stellar masses in the range $10^9 M_\odot$ to $10^{10.5} M_\odot$ into those likely to lie in high-density environments (HDE) and those likely to lie in low-density environments (LDE). Through comparison with galaxy catalogues extracted from the Millennium Simulation, we show that the sample of HDE galaxies should primarily ($\sim 61\%$) consist of satellite galaxies in groups, while the sample of LDE galaxies should consist of mostly ($\sim 87\%$) non-satellite (field and central) galaxies. Comparing the lensing signals around samples of HDE and LDE galaxies matched in stellar mass, we show that the subhaloes of HDE galaxies are less massive than those around LDE galaxies by a factor 0.65 ± 0.12, significant at the 2.9σ level. A natural explanation is that the haloes of satellite galaxies are stripped through tidal effects in the group environment. Our results are consistent with a typical tidal truncation radius of ~ 40 kpc.

For the case of data with spectroscopic redshifts, we analyse the GAMA-I and the ongoing GAMA-II surveys. We demonstrate the possibility of detecting tidal stripping of dark matter subhaloes within galaxy groups using weak gravitational lensing. We have run ray-tracing simulations on galaxy catalogues from the Millennium Simulation to generate mock shape catalogues. The ray-tracing catalogues assume a halo model for galaxies and groups, using various models with different distributions of mass between galaxy and group haloes to simulate different stages of group evolution. Using these mock catalogues, we forecast the lensing signals that will be detected around galaxy groups and satellite galaxies, as well as test two different methods for isolating the satellites' lensing signals. A key challenge is to determine the accuracy to which group centres can be identified. We show that with current and ongoing surveys, it will possible to detect stripping in groups of mass $10^{12} M_\odot$–$10^{15} M_\odot$.

Acknowledgements

Contents

List of Figures

List of Tables

Chapter 1

Introduction

The evolution and growth of galaxies is not a simple process. It depends not only on the intrinsic properties of the galaxy, but also on the environment the galaxy resides within. While many galaxies in the universe are relatively isolated, so-called "field" galaxies, and experience "secular" evolution, most galaxies are gravitationally bound to one or more other galaxies. These structures of galaxies are termed "groups" or "clusters," depending on their masses.

While there is no clear dividing line between groups and clusters, there is evidence that various properties of their constituent galaxies depend on the total mass of the structure in which they reside. In particular, the mass-to-light ratios, morphologies, and colours of galaxies show a strong dependence on the mass of the structure in which they reside. This is illustrated for the mass-to-light ratios of central galaxies in Fig. 1.1, which is taken from Figure 13 of Velander et al. (2013). While there is disagreement among different datasets about the exact nature of the trend, the data do agree on the overall trend in mass-to-light ratio for red galaxies: for low-stellar-mass galaxies, the mass-to-light ratio decreases as the stellar mass increases, reaching a minimum at a stellar mass of $\sim 5 \times 10^{10} M_\odot$. The ratio then begins to increase with increasing stellar mass.

The implication of these data is that, at the low-mass end, galaxies become more efficient at forming stars as they increase in mass. However, galaxies with stellar mass greater than $\sim 5 \times 10^{10} M_\odot$, which typically reside in the centres of groups or clusters, appear to become less efficient at forming stars as their stellar mass increases. This implies that some effect within a group environment efficiently quenches star formation. However, an open question remains as to how steep this change in mass-to-light ratio is with respect to mass; while data compiled by Leauthaud et al. (2012a), shown as the shaded region in Fig. 1.1, imply a steep rise in mass-to-light ratio, other weak-lensing measurements
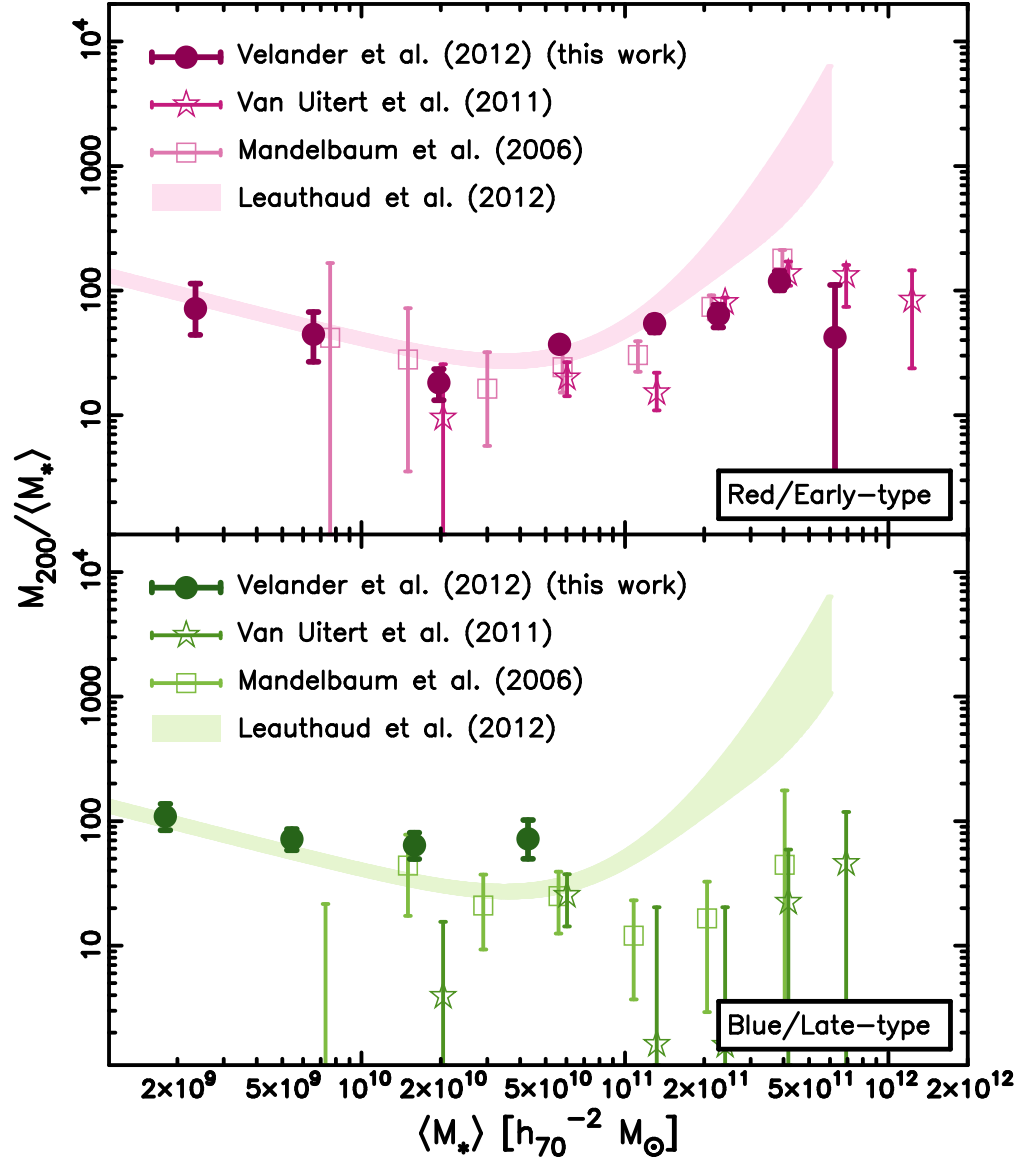
FIGURE 1.1: Figure 13 from Velander et al. (2013), illustrating mass-to-light ratios measured through weak gravitational lensing for red/early-type central galaxies (top panel) and blue/late-type central galaxies (bottom panel). Note that the COSMOS dataset makes no distinction between red and blue galaxies, so the same points are illustrated in both panels.

presented by Velander et al. (2013) imply a shallower rise. More data will be needed to assess which of these results is correct.

At present, it is still unknown what mechanism may be behind this star-formation quenching of galaxies near the centres of groups and clusters. Possibilities include galaxy mergers, which will cause an initial burst of star formation followed by a long period of quiescence; supernova feedback, in which the energy output of supernova activity slows or prevents future star formation; and AGN feedback, in which the energy output of an active galactic nucleus (AGN) slows or prevents star formation. Of these factors though, only mergers are likely to strongly depend on environment.

In addition to the lower rates of star formation exhibited by central galaxies within groups and clusters, this effect can also be seen in satellite galaxies. The population of satellite galaxies is significantly redder than for field galaxies (Dressler, 1980, Butcher and Oemler, 1984, Moore et al., 1996, Balogh et al., 1999, 2004), which implies that something quenches their star formation in a group environment which is not active for field galaxies. As with central galaxies, mergers can contribute to this for satellite galaxies. Additionally possibilities include ram pressure stripping, in which a galaxy passes through a dense region of the intra-cluster medium (ICM), and the gas in it is stripped away by pressure from the ICM; and tidal stripping, in which a galaxy passes near a more massive galaxy, and the massive galaxy pulls gas away from the less-massive galaxy. In either of the latter cases, the loss of gas, termed "strangulation," results in the galaxy's star formation being quenched (Abadi et al., 1999, Balogh and Morris, 2000, Quilis et al., 2000, Kawata and Mulchaey, 2008). All of these processes are believed to take place, but it is not known which might be the dominant cause of star-formation quenching, and if the dominant factor depends on group mass.

In this thesis, we focus on tidal stripping. Tidal stripping affects not only the baryonic content of galaxies, but also their dark matter haloes (Hayashi et al., 2004, Kazantzidis et al., 2004, Springel et al., 2008). As neither of the other possible quenching mechanisms in groups affects dark matter haloes, investigation of the dark matter haloes of galaxies in groups of varying mass can in principle indicate whether or not tidal stripping is occurring in galaxy groups, and in which group mass range it occurs. To do this, we use weak gravitational lensing to measure the profiles of galactic dark matter haloes, and compare these to the haloes of galaxies of similar stellar mass in the field. We design our lens catalogues to maximize the fraction of satellite galaxies within them, which will allow us a much cleaner picture of tidal stripping than previous datasets which included all galaxies, making no distinction between satellites and centrals.

In the introduction to this thesis, we will present an overview of the evolution of small- and large-scale structure in the universe, and how this affects the structure observed

today. We go on to discuss how galaxies form and evolve, and how this depends on the environment in which they reside. We then discuss the tools and techniques relevant to our analysis: gravitational lensing, photometric redshift estimation, and methods for identifying galaxy groups.

1.1 Dark Matter Structure

In this section, we discuss the role of dark matter in forming structure in the universe. Since dark matter comprises $\sim 85\%$ of all matter in the universe, it dominates the gravitational potential. It can thus be considered alone, without reference to baryonic physics, in a first-order approximation. The structure that forms from dark matter will then provide the gravitational potential in which baryonic physics can act. In Section 1.1.1, we will discuss the physics behind the collapse of dark matter structures, in Section 1.1.2, we will discuss models commonly used for the density profiles of dark matter haloes, and in Section 1.1.3 we will discuss substructure within dark matter haloes, and the mechanism of tidal stripping and its effects.

1.1.1 Structure Formation

Through cosmic inflation, quantum fluctuations in the early universe were expanded to cosmic scales at early times ($\sim 10^{-43} - 10^{-36}$ s), resulting in primordial density fluctuations. Since these quantum fluctuations were roughly Gaussian and nearly scale-invariant, single-field inflation models predict that the same will hold true for primordial fluctuations in the immediate aftermath of inflation. This leads to a Gaussian random distribution of density fluctuations, which can be characterized as a density field in which the following holds true:

$$p(\delta, V) = \frac{1}{\sqrt{2\pi}\delta_*(V)} \exp\left(-\frac{1}{2}\delta^2/\delta_*(V)^2\right) \tag{1.1}$$

(Press and Schechter, 1974), where δ is the overdensity of a region of space, $p(\delta, V)$ is the probability that a region of space with volume V will have overdensity δ, and δ_* is the standard deviation of δ for a region of space of volume V.

Alternatively, structure fluctuations can be expressed in terms of the power spectrum $P(k)$, where $P(k)$ is the Fourier transform of the autocorrelation function of the overdensity (Bertschinger, 1987). For a Gaussian random field, $P(k)$ will have the form:

$$P(k) \propto k^n, \tag{1.2}$$

where n is of order unity. This form is typically more useful for calculations involving the clustering of structure.

These primordial density fluctuations presented the groundwork for the growth of structures over the life of the universe. Under the standard cosmological model (Lambda Cold Dark Matter, or LCDM) for describing structure formation, these fluctuations grew in magnitude over cosmic time, eventually forming the structures we observe today.

The growth of structure is not a simple process, but it benefits analysis to look at simplified scenarios in which the equations are analytically solvable. In the radiation-dominated era of expansion, density fluctuations of small magnitude grew as $\delta \propto t$ for scales larger than the particle horizon, and stagnated for smaller scales. During the matter-dominated phase of expansion, small-magnitude density fluctuations grew as $\delta \propto t^{2/3}$ on all scales. Eventually, these structures reached a non-linear scale, collapsing into self-bound structures. For dark matter, which comprised $\sim 85\%$ of the universe, and is unable to radiate away its energy, the final state is a halo, supported by the random motion of its constituent particles.

Let us consider the simplified case of a spherical overdensity at the time of matter-radiation equality, having overdensity δ and radius r_0. Since this overdensity is denser than its surroundings, and its surroundings can be expected to be isotropic, the gravitational influence of all matter outside of the overdensity can be expected to cancel out and have no effect on the evolution of this overdensity. Similarly, the LCDM model predicts that dark matter, which composes the majority of matter in the universe, is non-interactive, it will exert no pressure. The exterior to this overdensity will then have no influence on what happens inside of it. We can thus treat this region as a self-contained universe, and safely ignore the exterior.

For the sake of mathematical simplicity, let us treat this overdensity with a spherical top-hat model, where the overdensity is δ for all points within distance r_0 of the centre of the sphere, and 0 for all points outside of this sphere. Imagine a single dark matter particle at distance $r < r_0$ from the centre of this region. Per Birkhoff's theorem, it will experience no net gravitational acceleration from matter at larger radii. Its acceleration can then be calculated as:

$$\begin{aligned}
\frac{d^2 r}{dt^2} &= -\frac{G_c \left(\frac{4}{3}\pi r^3 \rho \left[1 + \delta\right] \right)}{r^2} \\
&= -\frac{4}{3}\pi G_c r \rho \left(1 + \delta\right),
\end{aligned} \tag{1.3}$$

(White, 2009) where ρ is the background density of the universe. For comparison, the evolution equation for the scale factor of a mass-dominated universe is:

$$\frac{d^2a}{dt^2} = -\frac{4}{3}\pi G \rho a. \tag{1.4}$$

(White, 2009)

From the comparison of Equation (1.3) and Equation (1.4), we can see that this overdense region behaves exactly like a universe in its own right, with the same initial time and expansion rate as the surrounding universe, but different scale factor and density. We can then apply the same philosophy as in calculating the time-behaviour of a mass-dominated universe to determine the behaviour of this overdensity. Since the background density of the universe is close to the critical density, and $\delta > 0$, this overdensity will behave as a positively-curved universe. It will initially expand, reach a maximum size at some time, and eventually collapse to a point. As previously discussed, dark matter cannot perfectly collapse, however, as it cannot radiate away its energy, and so this discussion is valid only prior to the time at which the halo is supported by its own virial energy (until it is "virialized").

Let us first consider the parameterization of a matter-dominated universe:

$$a/a_{\mathrm{m}} = \frac{1}{2}(1 - \cos \eta)$$
$$t/t_{\mathrm{m}} = (\eta - \sin \eta)/\pi, \tag{1.5}$$

where a is the scale factor of the universe, a_{m} is the maximum scale factor, t is the time, t_{m} is the time at which the scale factor a is a maximum, and η is a parameter. This universe will collapse when $a = 0$, which implies $\eta = 2\pi$, which in turn implies that $t = 2t_{\mathrm{m}}$. We can then relate this to the linear approximation, which is valid when η is close to zero, by considering the Taylor expansion of the parameterization for small η. This gives us the relation:

$$\delta_{\mathrm{linear}} = \frac{3}{20} \left(6\pi t/t_{\mathrm{m}}\right)^{2/3}. \tag{1.6}$$

(White, 2009) At the time of collapse $t = 2t_{\mathrm{m}}$, we get:

$$\delta_{\mathrm{linear}} = \frac{3}{20} \left(12\pi\right)^{2/3} \approx 1.686. \tag{1.7}$$

Using this result, we can then use the linear approximation for all calculations, and assume that by the time this approximation predicts an overdensity will reach $\delta_{\mathrm{c}} = 1.686$, the overdensity will in fact have collapsed. Since the time at which a structure collapses depends only on when, in the linear approximation, it reaches this overdensity, the time

of collapse depends only on the initial overdensity of the structure. Additionally, since the initial overdensity δ is only a small perturbation to the background density, the total mass of the structure depends only on the initial size. However, the initial overdensity and initial size are statistically related: Large regions are less likely to be very overdense than are small structures, per Equation (1.1), which implies that low-mass structures will tend to collapse before high-mass structures.

Press and Schechter (1974) then show that the number density of collapsed structures at present day, with mass between M and $M + dM$ is:

$$N(M)dM \approx \frac{1}{\sqrt{\pi}} \left(1 + \frac{n}{3}\right) \frac{\rho}{M^2} \left(\frac{M}{M_*}\right)^{(3+n)/6} \exp\left(-\left(\frac{M}{M_*}\right)^{3+n/3}\right) dM, \qquad (1.8)$$

where n is the slope of the power spectrum (see Equation (1.2)) and M_* is a characteristic mass below which structures will typically have collapsed, which increases over time.

From this, we can put together a qualitative picture of structure formation. Structures collapse at a wide variety of times, but lower-mass structures tend to collapse first. As time proceeds, higher-mass structures will begin to collapse. These higher-mass structures, which comprise larger regions of space, will typically contain many lower-mass structures within them, which have already collapsed. The collapse of this massive structure can then be seen as a merger of low-mass structures.

The situation becomes significantly more complicated when baryonic physics is considered, as galaxies do not merge as readily as dark matter haloes. The general picture is that galaxies form in the first structures to collapse, and the larger collapsing structures form groups and clusters of galaxies. The exact physics of how and when galaxies in groups and clusters interact with each other and merge remains an open question, which this thesis aims to investigate.

1.1.2 Halo Models

Under the LCDM paradigm, dark matter consists of non-relativistic, non-interacting,[1] massive particles. Since the particles are noninteracting, dark matter haloes cannot be supported by pressure. One naive model for a halo is the singular isothermal sphere (SIS), which is characterized by the velocity dispersion, and thus temperature, being the same at any radius from the centre. It has the density profile:

$$\rho(r) = \frac{\sigma_{\mathrm{V}}^2}{2\pi G_{\mathrm{c}} r^2}, \qquad (1.9)$$

---

[1]Except through gravity, and possibly weak nuclear interactions.

where σ_V is the velocity dispersion. While this profile in fact provides a reasonable fit to many measurements of halo densities (through kinematics and gravitational lensing), it has a few problems. Notably, the total mass of the profile diverges; since the density at a given radius is proportional to r^{-2}, the total mass in a spherical shell is independent of radius. This can be solved by truncating the profile at some radius, through a truncated profile such as:

$$\rho(r) = \frac{\sigma_V^2}{2\pi G_c r^2} \frac{r_t^2}{r^2 + r_t^2}. \tag{1.10}$$

While the SIS profile provides a reasonable fit to most haloes, it was found in simulations that haloes typically have a shallower slope near the core, $\rho \propto r^{-1}$, and a steeper slope at the edges, $\rho \propto r^{-3}$) (Frenk et al., 1988, Efstathiou et al., 1988, Hernquist, 1990). Thus, Navarro et al. (1997) (NFW) proposed the following density profile, which shows this behaviour:

$$\rho(x) = \frac{M_0}{4\pi r_s^3} \frac{1}{x(1+x)^2}, \tag{1.11}$$

where r_s is the scale radius of the halo and $x = r/r_s$. This profile requires an additional parameter, the scale radius (or alternatively, the concentration $c = r_{200}/r_s$), but it does a significantly better job than the SIS profile at fitting simulated mass distributions. However, like the SIS profile, the NFW profile's total mass diverges. At large radii, its density obeys $\rho \propto r^{-3}$, and so the mass in a spherical shell is $\propto r^{-1}$, which diverges when integrated to infinity. This can be solved similarly to the SIS profile, giving the truncated NFW profile:

$$\rho(x) = \frac{M_0}{4\pi r_s^3} \frac{1}{x(1+x)^2} \frac{\tau^2}{\tau^2 + x^2}, \tag{1.12}$$

(Baltz et al., 2009) where $\tau = r_t/r_{200}$, and r_t is the truncation radius.

Unlike the SIS profile, the NFW profile has no theoretical basis for its functional form; it is purely an empirical fit to halo density profiles found in simulations of structure formation. The reason for this form remains an open question, but it is most commonly believed to be an consequence of the halo's accretion history (Wechsler et al., 2002, Zhao et al., 2003, Lu et al., 2006, Ludlow et al., 2013).

1.1.3 Halo Substructure

The above profiles all treat dark matter haloes as smooth and spherically-symmetric, but neither is the case in reality. Haloes are in fact more commonly triaxial (Jing and Suto, 2002), and they exhibit a large amount of substructure, caused by remnants of smaller haloes that merged with the larger halo. In the limit of galaxy clusters, most of the mass is contained within a single dark-matter halo, with the constituent galaxies and

their surrounding subhaloes contributing only small perturbations to the density profile (Mandelbaum et al., 2006a, Natarajan et al., 2007, Mandelbaum et al., 2008, Natarajan et al., 2009). Tidal interactions will strip both the stellar content and dark matter haloes of galaxies near the cores of clusters to $\lesssim 50\,\mathrm{kpc}$ (Richstone, 1976, Merritt, 1983). Gravitational lensing measurements have shown that the haloes around individual galaxies within clusters are significantly smaller than the haloes around comparably-luminous field galaxies, and this effect is more extreme with galaxies closer to the centres of clusters (Limousin et al., 2007, Natarajan et al., 2009). At the other extreme of the mass spectrum, namely field galaxies, gravitational lensing measurements have confirmed that the surrounding haloes can be well-approximated by an NFW density profile (Hoekstra et al., 2004, Kleinheinrich et al., 2006, Mandelbaum et al., 2008).

However, between the extremes of field galaxies and rich clusters, the picture is less clear. Since multiple galaxies must merge together to eventually form clusters, at some point the mass in the galaxies' individual haloes must migrate into a shared halo. This process most likely occurs through tidal stripping: when two galaxies pass near each other, the particles in the halo of the less massive galaxy will tend to be "stripped" from it and thus join the more massive galaxy's halo. We discuss this process in more detail in Section 1.1.3.1. Tidal stripping, along with ram pressure stripping, is also expected to remove hot gas from less massive galaxies, which will have the effect of cutting off their supply of cold gas and quenching their star formation in a process known as "strangulation" (Tinsley and Larson, 1979, Balogh and Morris, 2000). Galaxies in dense environments are known to be significantly redder on average than field galaxies (Dressler, 1980, Butcher and Oemler, 1984, Moore et al., 1996, Balogh et al., 1999, 2004), and both tidal and ram pressure stripping may contribute to the quenching of star formation (van den Bosch et al., 2008, Kawata and Mulchaey, 2008), so there is a strong motivation to understand the mechanics and timing of tidal stripping, to determine how much of a role it plays relative to ram pressure stripping and other mechanisms. While the mechanics of tidal stripping on individual satellites have been well-studied in simulations (Hayashi et al., 2004, Kazantzidis et al., 2004, Springel et al., 2008), its aggregate effects on a population of satellite galaxies, including whether the aggregate stripping of satellites is rapid or gradual, remains unclear. This can in part be investigated through analysis of the group and cluster scales on which tidal stripping can be observed to occur.

In this thesis, we focus on galaxy groups, an intermediate mass scale between field galaxies and clusters (typically structures in the mass range $10^{12}\,M_\odot \lesssim M_\mathrm{halo} \lesssim 10^{14}\,M_\odot$ are considered groups, and more massive structures are considered clusters). Weak gravitational lensing provides the only practical tool to measure the density profiles and masses of dark matter haloes around satellite galaxies within groups, as tracers such as

globular clusters and planetary nebula are rare at distances $\gtrsim 50\,\mathrm{kpc}$ and difficult to detect in distant groups (Gavazzi et al., 2007, van de Ven et al., 2009). Lensing analyses of groups (Hoekstra et al., 2001, Parker et al., 2005, Mandelbaum et al., 2006a, Johnston et al., 2007, Hamana et al., 2009, Leauthaud et al., 2010, Ford et al., 2012) have shown that the group lensing signal can be measured and is on average consistent with an NFW density profile. However, it is unclear how much of this signal results from a central halo, and how much is due to the contributions of satellites (Gillis et al., 2013b). As such, it is necessary to measure the lensing signals around satellites themselves to get a full picture of the mass distribution. Only limited work has been done in the group regime to date. For example, Suyu and Halkola (2010) studied a strong-lensing system and determined that tidal stripping did seem to occur around the satellite studied, which lies in a group of mass on the order of $10^{12} M_{\odot}$. While this result is promising, a broader base of data will be needed to develop a general understanding of the dark matter properties of satellite galaxies in galaxy groups.

1.1.3.1   Tidal Stripping of Dark Matter

In this section we present a basic analysis of the process of tidal stripping. Let us start with a simplified scenario, in which a satellite travels in a circular orbit around the centre of a galaxy group. We start by modelling both the satellite and group as point masses, and assume that the satellite is much less massive than the group. Let M be the mass of the group, m be the mass of the satellite, and R be the separation between the group and the satellite.

Consider a dark matter particle in the satellite's halo. Since the mass of this particle is negligible compared to the satellite and group masses, we can treat the group-satellite-particle system as the "restricted three-body problem" (Szebehely and Grebenikov, 1969). The satellite and group in this problem will rotate about their centre-of-mass at angular speed:

$$\Omega = \sqrt{\frac{G\,(M + m)}{R^3}}, \tag{1.13}$$

and we can thus rotate our frame of reference along with this frame. Under this frame, the Jacobi integral will be conserved for the dark matter particle:

$$E_{\mathrm{J}} = \frac{1}{2}v^2 + \Phi(\vec{r}) - \frac{1}{2}\left|\vec{\Omega} \times \vec{r}\right|^2, \tag{1.14}$$

(Binney and Tremaine, 2008) where v is the velocity of the dark matter particle, $\vec{r}$ is the position within this rotating frame of reference, and $\Phi(\vec{r})$ is the gravitational potential at position $\vec{r}$.
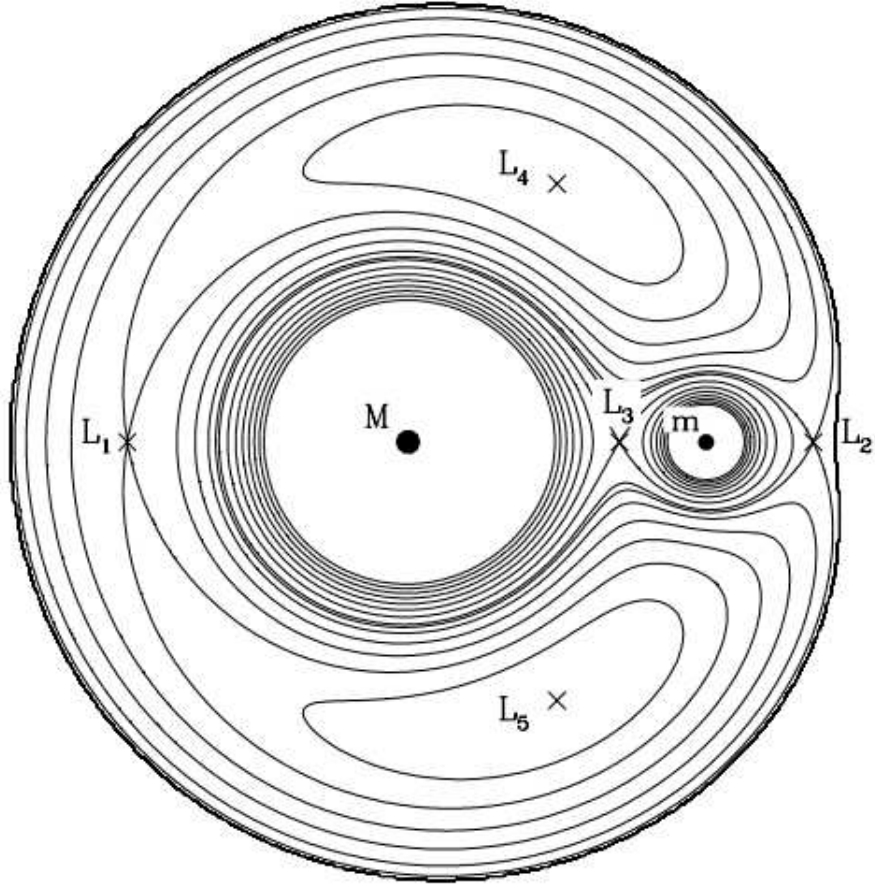
FIGURE 1.2: Figure 8.6 from Binney and Tremaine (2008), illustrating the effective gravitational potential in a rotating frame of reference for the restricted three-body problem. Lines illustrate contours of equal effective potential, and L_n illustrate the positions of the five Lagrange points, where the potential has an extremum or saddle point. The two masses, M and m, lie at minima of the effective potential.

Equation (1.14) thus gives us a constraint on the positions in which the dark matter particle may be found, since we must have $v^2 > 0$. As such, we have the constraint:

$$\Phi_{\text{eff}}(\vec{r}) \equiv \Phi(\vec{r}) - \frac{1}{2}\left|\vec{\Omega} \times \vec{r}\right|^2 \leq E_{\text{J}}. \tag{1.15}$$

The form of Φ_{eff} can be seen in Fig. 1.2. If a dark matter particle is initially constrained by one of the nearly-circular contours surrounding only m, it will remain in this region for the indefinite future. Otherwise, it will be bound to either M alone or the system as a whole. The subset of particles bound strictly to m can thus be characterized as those which lie within a contour that surrounds only m. The largest such contour is the one which passes the the L_3 Lagrange point, which represents a saddle point in the effective potential between M and m.

We can thus approximate the tidal radius of the satellite in this scenario as the distance

11

between it and the L_3 point, as no particle which is at any point found outside this radius will be bound strictly to the satellite. In the approximation that $m \ll M$, the distance from the satellite to the L3 point can be approximated as:

$$r_{\text{tidal}} = \left(\frac{m}{3M}\right)^{1/3} R \qquad (1.16)$$

(Binney and Tremaine, 2008). In the point-mass approximation, we can calculate the mean density of the satellite and group contained within spheres of radii r_{tidal} and R respectively as $\overline{\rho_{\text{sat}}} = m/\left(\frac{4}{3}\pi r_{\text{tidal}}^3\right)$ and $\overline{\rho_{\text{group}}} = m/\left(\frac{4}{3}\pi R^3\right)$. This then gives us the relation between these two mean densities:

$$\overline{\rho_{\text{sat}}} = 3\overline{\rho_{\text{group}}} \qquad (1.17)$$

(Binney and Tremaine, 2008).

From Equation (1.17), we can state that, under the approximations made here, a satellite will be stripped to a radius such that its mean density is within order unity of the mean density of the host group within the satellite's orbital radius. This result is independent of the satellite and group masses, as well as the relative velocity of the satellite and group. From the form of Equation (1.16), we can see stripping increases in strength (the tidal radius lowers) with decreasing satellite mass, increasing group mass, and decrease orbital radius, and has no explicit dependence on the relative velocities of the satellite and group. However, the assumptions made thus far differ from the a more realistic model of dark matter subhaloes orbiting a larger group or cluster halo:

1. Satellites and groups are not point masses, which affects the effective potential.

2. Satellites do not follow circular orbits within groups, and so they aren't stripped at a constant radius. Stripping is strongest when the satellite passes pericentre and weaker at other times. Satellites also experience dynamical friction, causing their orbits to decay over time. This results in the satellites passing closer to the group centre every orbit (Taylor and Babul, 2004).

3. Satellites interact not only with the group centre, but also with other satellites. A typical satellite in a rich cluster will have had one close encounter with another satellite before passing pericentre (Binney and Tremaine, 2008). This effect, known as harassment, will also contribute to mass loss from the satellite's halo, as each encounter will typically inject energy into the satellite's halo, allowing some particles to escape (Moore et al., 1996, Gnedin et al., 1999, Kravtsov et al., 2004).

To properly account for the eccentricities of satellite orbits, we first must identify the satellite-group separation in Equation (1.16) with the pericentre distance of the satellite

from the group centre. In addition to this, each pass of the satellite near the group centre will result in a tidal shock, which adds energy to the satellite's halo and allows some particles to escape. The energy added for a close encounter can be calculated to be:

$$\Delta E \propto \frac{M^2 m^2}{V^2 R^4} U(R/r_{\rm h}) \tag{1.18}$$

(Binney and Tremaine, 2008), where ΔE is the energy input, $r_{\rm h}$ is the half-mass radius of the group halo, and $U(R/r_{\rm h})$ is a factor which corrects for the fact that the group's halo has an extended mass distribution, which can be calculated numerically for a given halo model. For a typical halo model, $U(R/r_{\rm h})$ converges to zero for $R \to 0$ and converges to 1 for $R \gg r_{\rm h}$. The energy input, and thus the strength of tidal shocks, increases with increasing group mass, decreasing relative velocity, and it peaks at $R \sim r_{\rm h}$. As the binding energy of the satellite's halo varies with m^2, the efficacy of tidal shocks in removing dark matter shows no strong reliance on satellite mass.

Taking these factors into consideration, numerical simulations are able to model individual stripping events to high accuracy (Hayashi et al., 2004, Kazantzidis et al., 2004, Springel et al., 2008). Observational constraints are needed, however, to test the predictions of these simulations, and in particular the aggregate effects of tidal stripping on the populations of satellite galaxies within groups.

1.1.4 Outstanding Issues in LCDM

While the LCDM paradigm has done a very good job at explaining most cosmological observations, and the existence of dark matter has received direct evidence from the Bullet Cluster (Clowe et al., 2004), there remain some open questions about the model. In this section we will briefly discuss some of the biggest open questions in the LCDM model: the nature of dark matter (Section 1.1.4.1), the missing satellites problem (Section 1.1.4.2), and the cusp-core problem (Section 1.1.4.3).

1.1.4.1 Nature of Dark Matter

Firstly, there is the question of the nature of dark matter. Many particles have been hypothesized which could correspond to dark matter, and there has recently been tentative evidence for direct detection of some such particles from DAMA (Bernabei et al., 2008, 2010) and CDMS (CDMS Collaboration et al., 2013), both of which found evidence for dark matter particles with mass of $\sim 1 - 10$ GeV. This mass is sufficiently large to qualify as "cold" dark matter, as opposed to "warm" or "hot" dark matter. However, these detections are inconsistent with other negative results (CDMS II Collaboration

et al., 2010, Ahmed et al., 2011, Angle et al., 2011, Aprile et al., 2012). These results are all relatively new, though, and it is quite possible that a consensus will emerge before too long.

The most well-motivated candidate dark matter particles include:

- **Axions:** Particles proposed to explain the lack of CP-violation in strong nuclear processes, with expected mass in the range of μeV. While this mass would not typically correspond to a "cold" dark matter particle, axions are not expected to have ever been in thermal equilibrium, and would have formed a Bose-Einstein condensate at the time of decoupling (Sikivie, 2010).

- **Neutralinos:** Particles predicted under supersymmetry, with a predicted mass range of 45 GeV $< M_\chi < 7$ TeV (Martin, 1998).

- **Sterile neutrinos:** A class of neutrinos motivated by the fact that all observed neutrinos have left-handed chirality, while all other known fermions have been observed with both left- and right-handed chirality. Sterile neutrinos have a very wide range of allowed masses, from ~ 1 eV to $\sim 10^{15}$ GeV (Drewes, 2013).

1.1.4.2 Missing Satellites Problem

A significantly more longstanding problem in the LCDM paradigm is the "missing substructure" problem (Klypin et al., 1999, Moore et al., 1999a). In the LCDM model, the structures formed by dark matter are self-similar; a galaxy should have as much substructure as a cluster, only scaled down. This has been confirmed repeatedly by N-body simulations of dark matter, but it is difficult to test in reality, as we cannot directly observe dark matter structure. We can see the luminous galaxies which populate dark matter haloes, however, and these show evidence for significantly less substructure around galaxies than around clusters. For example, in the Local Group, there are only between a tenth and half as many visible satellites (depending on the mass range examined) as would be expected if every dark matter halo were populated with a galaxy (Kauffmann et al., 1993, Klypin et al., 1999, Moore et al., 1999a). This problem is particularly notable among the more massive substructures found in N-body simulations, which are deemed "too big to fail" at forming galaxies, and for which cold dark matter simulations also overpredict their abundance. The recent discoveries of low-surface brightness dwarf galaxies in the Local Group (Willman, 2010) have somewhat, but not entirely mitigated this problem (Bullock, 2010), however, and it is possible that future such discoveries will resolve the issue.

One possible explanation for this problem is that feedback or environmental effects inhibit the formation of low-mass galaxies, which results in the low number of dwarf galaxies observed in the Local Group relative to the expected number of dark matter subhaloes. These effects, and their possible roles in the missing substructure problem, are discussed further in Section 1.2.3 and Section 1.2.5.

Alternatively, it is possible that the Local Group is simply an extreme outlier, with an unusually low number of dark matter subhaloes in it. To determine whether or not this is the case, it is necessary to search for dwarf galaxies in other groups. However, identifying dwarf galaxies within the Local Group is already quite difficult, and so it is not an easy task at all to detect dwarfs in other groups. It is, however, in principle possible to use distortions in strong lensing detections to estimate the typical substructure abundance (Vegetti et al., 2010), but this will require significantly more strong lensing detections than are presently available to generate a significant result. This methodology notably can detect even dark substructure, and so could in principle help discern whether the cause of this problem is due to some aspect of baryonic physics, or otherwise a problem with the LCDM model.

Finally, it is possible that this problem represents a flaw in the LCDM model. One possible solution would be if dark matter were "warm" - that is, non-relativistic, but with a non-negligible free-streaming distance. This would smooth out dark matter haloes, and decrease the amount of substructure present on scales less than the free-streaming distance (Bode et al., 2001, Lovell et al., 2012). However, the problem with this hypothesis is that it may eliminate substructure too well: It is difficult to tune the mass of the dark matter particle to predict the abundance of substructure accurately on all scales in the Local Group (Polisensky and Ricotti, 2011). Nevertheless, warm dark matter models typically do a better job than cold dark matter models at fitting the observed structure in the Local Group; the abundance of substructure in the Local Group observed to-date is best fit by a warm dark matter particle with mass on the order of $\sim 4 - 10$ keV (Polisensky and Ricotti, 2011, Viel et al., 2013). However, this dark matter particle mass may not fit with measured masses. For instance, CDMS (CDMS Collaboration et al., 2013) finds a best-fit particle mass of 8.6 GeV, which is inconsistent with warm dark matter, if this result turns out to be sound. This does not rule out mixed dark matter, however, which would allow for a cold particle in this mass range, in addition to a warm particle (Davis et al., 1992, Borgani et al., 1996, Boyarsky et al., 2009b,a).

1.1.4.3 Cusp-Core Problem

In dark matter simulations, dark matter is observed to form arbitrarily dense cusps at the centres of haloes, limited only by the simulation resolution. However, rotation curves near the centres of galaxies show significantly flatter profiles; they form "cores," rather than cusps (Moore et al., 1999b, Alam et al., 2002, Kuzio de Naray et al., 2008). This problem is not easily solved by appealing to baryonic physics. Unlike dark matter, baryons can cool through radiating away energy, and so they typically form even denser structures, which would be the opposite of what is needed to solve this problem.

However, this naive argument neglects the effects of supernova feedback (see Section 1.2.3). Periodic bursts of supernova activity can pump energy into not only the surrounding baryons, but also into the dark matter haloes through suddenly making the potential more shallow, allowing dark matter particles to escape. This could have the effect of smoothing out dark matter haloes near the centres of galaxies, and advanced hydrodynamical simulations have been able to accurately reproduce the observed rotation curves near the centres of galaxies, when they allow for a sufficiently high density threshold for star formation and efficient feedback (Pontzen and Governato, 2012, Governato et al., 2012, Teyssier et al., 2013).

As with the missing satellites problem, it is possible that the cusp-core problem might be solved by warm dark matter. Warm dark matter could in principle flatten the density profiles near the centres of haloes and better fit observations (Avila-Reese et al., 2001, Bode et al., 2001). However, this explanation is controversial, and some authors argue that it cannot explain observed data (Macciò et al., 2012). As with the missing satellites problem, a measured mass for the dark matter particle could potentially rule out this scenario.

1.2 Galaxy Formation

In comparison to dark matter physics, baryonic physics is vastly more complicated and more difficult to simulate. The primary difficulty arises due to the fact that, while dark matter interacts only through gravity, which is scale-independent, baryons additionally experience electromagnetic, nuclear, and chemical interactions, all of which typically take place on significantly smaller scales than gravitational interactions. This makes it prohibitively expensive to accurately simulate all possible interactions at once. However, unlike dark matter, baryonic matter is much more easily observable, and the physics of its interactions is much better understood. This allows baryonic simulations to model various possible interactions, conserving computer time to focus on aspects which are

more difficult to model (such as hydrodynamics). The results of these simulations can then be compared with observables to test the accuracy of the physical assumptions behind them.

The observable light in distant galaxies is due almost entirely to their constituent stars, and hot gas within galaxy clusters (the intracluster medium, or ICM) radiates light in the X-ray spectrum. This section will discuss the history of star formation within galaxies, while the applications and interpretations of ICM detections will be discussed in Section 1.5. In Section 1.2.1, we will discuss the cooling and collapse of galaxies, and how this leads to star formation. In Section 1.2.3, we will discuss feedback effects within galaxies which may slow or prevent star formation, and in Section 1.2.5, we will discuss the role that environmental effects play on galaxy evolution.

1.2.1 Cooling

One of the primary differences between baryons and dark matter is that, while dark matter haloes readily merge with each other and wash out substructure given sufficient time, the same does not appear to be the case with baryons. While in a cluster, most of the dark matter will merge into a single, unified halo over time, galactic mergers are significantly rarer. Some galactic mergers do indeed happen in groups and clusters, forming larger galaxies (Bright Cluster Galaxies, or BCGs), which lie at the centre of the dark matter potential, but these are the minority.

The reason that galactic mergers are rarer than dark matter mergers is that galaxies are more tightly-bound than are dark matter haloes. This is due to the fact that, unlike dark matter, baryonic matter is able to radiate away its thermal energy, allowing it to cool and contract, becoming more tightly bound in the process. The behaviour of a gas cloud as it cools depends on the relative length of its cooling timescale and its collapse timescale. If the cooling timescale is shorter than the timescale for collapse, the galaxy will be able to cool efficiently and begin to form stars. Alternatively, if the collapse timescale is shorter than the cooling timescale, the gas cloud will collapse until it is supported by its internal pressure. If the cooling timescale is shorter than the age of the galaxy, the cloud will collapse and begin forming stars, but otherwise the cloud will be observable today in an uncooled state as it gradually cools.

In order to calculate the cooling timescale of a gas cloud, we must consider the physics behind cooling. The primary cooling mechanisms in gas clouds are thermal Bremsstrahlung radiation and recombination radiation. Let us first consider thermal Bremsstrahlung radiation. Bremsstrahlung radiation occurs when charged particles accelerate, and is proportional to the acceleration of these particles. Gas clouds will typically consist

of an ionized plasma, which contains ionized particles in the form of electrons and ions. Since electrons are orders of magnitude less massive than ions, the thermal Bremsstrahlung radiation of this plasma will be dominated by the radiation caused by accelerating electrons.

We can estimate the intensity of thermal Bremsstrahlung radiation by considering the frequency of electron-ion interactions. The more electrons are present, the more frequent interactions will be, and similarly for ions. Therefore, we can say:

$$f \propto n_\mathrm{e} n_\mathrm{i}, \tag{1.19}$$

where f is the frequency of interactions, n_e is the number density of electrons, and n_i is the number density of ions. Additionally, the frequency of interactions will depend on the relative velocities of electrons and ions. Assuming that the cross-section for interactions is, to first order, independent of the relative velocities of the particles, then the frequency of interactions will also be proportional to the typical relative velocity between an electron and an ion. Since electrons are significantly less massive than ions and assuming the electrons and ions are at the same temperature, the electrons' velocities will be the primary determinants of the frequency of interactions. The typical velocity of an electron is proportional to $T^{1/2}/m_\mathrm{e}$, where T is the temperature of the plasma, and m_e is the electron mass.

Putting this together, and accounting the fact that some ions will produce more than one electron each, we obtain the density of Bremsstrahlung radiation per unit volume as:

$$\epsilon = 1.4 \times 10^{-27}\,\mathrm{erg\,cm^{-3}\,s^{-1}\,K^{-1/2}}\,T^{1/2} n_\mathrm{e} n_\mathrm{i} Z^2 g_\mathrm{B}, \tag{1.20}$$

(Rybicki and Lightman, 1986) where Z is the proton number of the ion, and g_B is the Gaunt factor, which is of order unity.

In addition to Bremsstrahlung radiation, gas can cool through recombination radiation. This occurs when atoms within a gas collide, exciting or freeing electrons. When these electrons recombine with ions, they release energy in the form of radiation. The intensity of recombination radiation, similar to Bremsstrahlung radiation, will be proportional to the number density of ions in the gas. Since it is primarily ion-ion interactions that enable recombination radiation, we can say the frequency of interactions is:

$$f \propto n_\mathrm{b}^2, \tag{1.21}$$

where n_b is the number density of baryons in the gas. In addition to the density, the frequency will also depend on the temperature of the gas, but the reliance on temperature

is non-trivial. For most astrophysical systems, however, it can be fairly approximated as $f \propto T^{-1/2}$ (Padmanabhan, 1993).

Since both Bremsstrahlung and recombination radiation depend on the square of the number density of particles, we can thus express the total radiative power as:

$$P \propto \left(A_{\mathrm{B}} T^{1/2} + A_{\mathrm{R}} T^{-1/2} \right) n_{\mathrm{b}}^2, \tag{1.22}$$

where A_{B} and A_{R} are coefficients, dependent on the composition of the gas, which determine the exact strengths of Bremsstrahlung and recombination radiation respectively. From this, we can see that Bremsstrahlung radiation will typically dominate at high temperatures, and recombination radiation will dominate at lower temperatures.

The cooling time of a gas will be proportional to the total energy in the gas, and inversely proportional to the total radiative power, $t_{\mathrm{cool}} \propto n_{\mathrm{b}} T / P$. Inserting the proper constants, we thus find the cooling time to be:

$$t_{\mathrm{cool}} = 8 * 10^6 \, \mathrm{year} \left(\frac{n_{\mathrm{b}}}{\mathrm{cm}^{-3}} \right)^{-1} \left[\left(\frac{T}{10^6 \, \mathrm{K}} \right)^{-1/2} + 1.5 f_m \left(\frac{T}{10^6 \, \mathrm{K}} \right)^{-3/2} \right]^{-1}, \tag{1.23}$$

(Padmanabhan, 1993) where f_m is a constant which depends on the composition of the gas. For a primordial composition of hydrogen and helium, f_m is of order unity. For typical solar metallicity, $f_m \approx 30$. This equation uses a temperature of 10^6 K, above which Bremsstrahlung will be the dominant source of radiative cooling, and below which recombination will be the dominant source, although the exact temperature is dependent on the metallicity of the gas. Typically, galaxies will have temperatures lower than this threshold, and will thus be dominated by recombination cooling.

To determine whether a galaxy will be able to cool efficiently, we must compare the calculated cooling time to the time it takes for the galaxy to collapse. If a galaxy is going to collapse as efficiently as possible, we can model the collapse as the free-fall of a particle at the edge of the spherically-symmetric gas cloud, giving the relation:

$$t_{\mathrm{freefall}} = \sqrt{\frac{3\pi}{32 G_{\mathrm{c}} \rho_0}}, \tag{1.24}$$

where ρ_0 is the initial density of the gas cloud, including its dark matter content. Since $\rho_0 = M / \left(\frac{4}{3} \pi R_0^3 \right)$, where M is the mass of the gas cloud, and R_0 is its initial radius, we then obtain the relation $t_{\mathrm{freefall}} \propto M_0^{-1/2} R_0^{3/2}$. In units typical of gas clouds, we then obtain the equation:

$$t_{\mathrm{freefall}} = 1.5 * 10^9 \, \mathrm{yr} \left(\frac{M}{10^{12} \, \mathrm{M}_\odot} \right)^{-1/2} \left(\frac{R_0}{200 \, \mathrm{kpc}} \right)^{3/2}. \tag{1.25}$$

(Padmanabhan, 1993)

In order to relate this timescale to the cooling timescale calculated in Equation (1.23), we must relate the mass and radius of the gas cloud to its initial temperature. We can do this through application of the Virial Theorem, which gives us the relation:

$$\frac{3}{5}\frac{G_c M}{R} = \frac{3}{2}\frac{k_B T}{m_p},\tag{1.26}$$

where k_B is Boltzmann's constant and m_p is the typical particle mass in the gas. Using this, and assuming that a fraction F of the total mass of the structure is baryonic (the rest being dark matter), and with the constraint that a galaxy will be able to cool efficiently only if its cooling timescale is lower than its collapse (freefall) timescale, we thus obtain the constraint for efficient cooling:

$$M < 6.4 * 10^{11}\,\mathrm{M_\odot} f_m \left(\frac{F}{0.1}\right).\tag{1.27}$$

(Padmanabhan, 1993)

Equation (1.27) tells us that there is an effective upper limit to the mass of a gas cloud that can cool efficiently. This depends on both the baryon fraction and the metallicity of the cloud, and implies that more massive galaxies will be able to form in more metal-rich regions (since the presence of metals allows more cooling channels through recombination), or regions with a higher fraction of baryonic matter. While the latter scenario is not as likely, the former is possible in regions that have a history of star formation.

Notably, while these considerations explain why there is an effective upper limit to the masses of galaxies (which is only surpassed through mergers, which are relatively rare), there is no justification here for a lower limit on the mass. If these were the only considerations, then we would expect arbitrarily small galaxies to form, in a hierarchy of substructure down to the mass where there is insufficient gas to form any stars. However, as discussed in Section 1.1.4, there are fewer low-mass galaxies in the Local Group than expected. In Section 1.1.4, we discussed possible alterations to the LCDM model which may contribute to this, and in Section 1.2.3, Section 1.2.4, and Section 1.2.5, we will discuss mechanisms within galaxies and groups which can inhibit star formation.

1.2.2 Star Formation

Once a gas cloud has collapsed to the point where star formation is possible, it is no longer valid to assume that the cloud is reasonably smooth and spherically-symmetric. In particular, spherical symmetry is not at all a valid assumption, as star-forming galaxies

often have a disk shape due to conservation of angular momentum (usually with a bulge in the centre which is not presently forming stars). Additionally, galaxies are not smooth. Even before the formation of spiral arm structure, gas clouds will have regions of high- and low-density, and these will not all be aligned radially.

Galactic gas also cannot be considered to be a single fluid. Galaxies typically have two different types of gas: a reservoir of hot, atomic hydrogen; and smaller local regions of cold, molecular hydrogen (Schaye, 2004, Krumholz et al., 2011). The transition between these two phases of hydrogen is relatively rapid, due to a positive feedback loop that forms in regions with sufficiently high densities, including thermal instability at inter- mediate temperatures and self-shielding from UV radiation, so these components can typically be considered separately (Schaye, 2004).

The gas in a galaxy also cannot be considered to be a fixed mass. Galaxies constantly accrete gas throughout their lifetimes. Hot gas is slowly added to the galaxy's reservoir, and it is also commonly believed that "cold flows" directly replenish the galaxy's cold gas (Dutton et al., 2010, Genzel et al., 2010). Additionally, environmental interactions (see Section 1.2.5) can strip away a galaxy's hot or cold gas, inhibiting future star formation.

Overall, star-forming galaxies must be seen as active processes, and their appearance will thus depend not only on their current activity, but on their history (mergers, interactions with other galaxies, etc.). In Section 1.2.3, Section 1.2.4, and Section 1.2.5 we will continue this discussion, with reference to how star-formation can be affected by feedback effects and by environment.

1.2.3   Stellar Feedback

In order to form a full picture of star formation, we also must understand the processes that can inhibit or prevent it. One class of these processes is the effects of feedback. These are effects which are caused by star formation, but which slow or stop further star formation in the region. Two important classes of feedback are stellar feedback and AGN feedback. We will discuss stellar feedback in this section, and AGN feedback in Section 1.2.4.

Stellar feedback is due to the fact that, once stars form, they emit significant amounts of energy into the surrounding gas. For most stars, this is a negligible effect, but super- novae, although rare, are significantly energetic to provide a significant amount of energy to the surrounding gas. This is particularly notable during starburst events, which are typically triggered by galaxy mergers, and which result in regions of extremely dense gas and rapid star formation (Martin, 1999, Springel et al., 2005a). Since gas needs to

cool and contract to form stars, this extra energy will slow down the process of star formation.

The feedback from supernovae can be approximated relatively easily. If we assume that for a unit mass of gas, ϵ_0 of energy will be added back to the gas through supernova feedback, then we can estimate the decrease in the star formation rate $\dot{M}_0$ as:

$$\frac{\Delta \dot{M}}{\dot{M}_0} = \frac{1}{1 + v_c^2/\epsilon_0},\tag{1.28}$$

(White, 2009) where v_c is the mean circular velocity of the galaxy. If feedback is maximally-efficient, then ϵ_0 will be $(\sim 700\,\mathrm{km/s})^2$. A typical star forming galaxy will have $v_c \lesssim 300\,\mathrm{km/s}$, and so if feedback is near its maximum efficiency, it can almost completely inhibit star formation in a galaxy with a low circular velocity (and thus low mass). This discussion gives an effective lower limit for the circular velocity of $\sim 100\,\mathrm{km/s}$, depending on how efficient feedback is, as below this threshold, stars will form too slowly to form a visible galaxy. However, numerous galaxies below this threshold can be observed in the Local Group, and so it is apparent that this elementary analysis is insufficient at properly characterizing supernova feedback. Other considerations, such as how the efficiency of supernova feedback varies with gas density, must also be considered to properly account for the observed mass distribution of galaxies.

In addition to the energy that supernovae add into the surrounding gas, it is also possible that, in smaller galaxies, supernova activity might completely eject gas from the galaxy, preventing all future star formation. This could in principle explain why there is a dearth of low-mass galaxies in the Local Group. If galaxies are not sufficiently massive, then after they begin to form a small number of stars, supernovae may eject all gas from the potential well, preventing any other stars from forming. The resulting "galaxy" will often be undetectable.

From the above discussion, it might seem that supernova feedback would do a good job at inhibiting galaxy formation, and perhaps account for the missing substructure problem (see Section 1.1.4.2). However, recall that the problem is not due simply to a lower limit in the mass of observed satellite galaxies, but an underabundance of galaxies in all mass ranges below the Milky Way's mass. Such galaxies do exist, but there are not as many as would be predicted if all dark matter haloes are populated. While supernova feedback might explain why low-mass haloes are not populated at all (at least visibly), it does not explain why only a fraction would be populated, unless one postulates a greatly-varying efficiency of feedback.

1.2.4 AGN Feedback

An active galactic nucleus (AGN) consists of a black hole and its accretion disk near the centre of a galaxy. The deep potential well at the black hole's event horizon allows infalling matter to gain a large amount of energy. However, since the infalling matter cannot easily shed its angular momentum, it forms a dense accretion disk around the black holes. This disk is sufficiently dense that friction will occur between concentric rings, and the energy that matter picked up by falling into the potential well will be radiated outward.

If we make the assumption that all of the energy a particle gains by falling into the black hole is radiated out before it crosses the black hole's event horizon, we can estimate how powerful an AGN will be in proportion to the rate at which mass is fed into it. Assume that the black hole has mass M_{BH} and an infalling particle has mass M_{p}. If the black hole is non-rotating, its innermost stable circular orbit (ISCO) can be calculated to be:

$$R_{\mathrm{ISCO}} = \frac{6G_{\mathrm{c}}M_{\mathrm{BH}}}{c^2}. \tag{1.29}$$

The potential energy at this orbit will then be:

$$U_{\mathrm{ISCO}}(M_{\mathrm{P}}) = -\frac{G_{\mathrm{c}}M_{\mathrm{BH}}M_{\mathrm{P}}}{\left(\frac{6G_{\mathrm{c}}M_{\mathrm{BH}}}{c^2}\right)} = \frac{1}{6}M_{\mathrm{P}}c^2. \tag{1.30}$$

From this, a particle would radiate out energy equal to 1/6 of its rest energy if it were to fall into a black hole. In practice, the actual fraction is closer to 1/10, as not all of the energy a particle gains by falling in is radiated out.

This is an extremely large amount of energy per unit gas mass that is accreted by the black hole, and it can in fact be significant enough to shut down all star formation in a galaxy. To obtain actual numbers on how much the AGN will inhibit star formation, we would need to make some assumptions about the size of the black hole. However, black holes found at the centres of galaxies vary over an extremely large mass range, and so the effects of AGN feedback will be highly individualized to each galaxy (Croton et al., 2006).

1.2.5 Environmental Effects

Most galaxies in the universe reside in some sort of large-scale structure, such as a group or cluster of galaxies (Marinoni et al., 2002, Robotham et al., 2011, Velander et al., 2013). In these circumstances, the environment can have a very strong influence

on the evolution of galaxies. Of particular note, red and elliptical (or "early-type")[2] galaxies exist almost exclusively in groups and clusters (Dressler, 1980, Butcher and Oemler, 1984, Moore et al., 1996, Balogh et al., 1999, 2004). It is apparent that some environmental effect in these regions of space triggers the transformation of blue galaxies into red galaxies, and disk galaxies into ellipticals.

There are three main mechanisms through which a galaxy's environment can have an effect on it: mergers, ram pressure stripping, and tidal stripping. Mergers occur when galaxies collide with each other. Most galaxy merges are "minor" mergers, where one galaxy is significantly more massive than the other. These mergers result in little disruption to the larger galaxy, and the smaller galaxy is absorbed into the larger one. Minor mergers can effectively be "cold flows" of gas into larger galaxies, fuelling star formation in them. "Major" mergers, between galaxies of roughly equal mass, will significantly disrupt both galaxies. The resulting galaxy may experience a brief starburst phase, where the extreme gas densities created by the merger fuel rapid star formation, followed eventually by a long period of quiescence. In the aftermath of these mergers, after the starburst phase, the galaxies will typically appear as "red and dead" ellipticals (Padmanabhan, 2002).

Ram pressure occurs when a galaxy passes the dense intracluster medium (ICM) of a galaxy group or cluster. The pressure of the ICM against the galaxy strips away the galaxy's gas, which then joins the ICM. The amount of pressure will be proportional to $\rho_{\mathrm{ICM}} v_{\mathrm{g}}^2$, where ρ_{ICM} is the density of the ICM, and v_{g} is the velocity of the galaxy through the ICM. Both of these values increase with the mass of the group or cluster, so ram pressure stripping will have the most significant effect on galaxies in clusters, and negligible effect on galaxies in groups (Quilis et al., 2000).

Tidal stripping, which is the main focus of this thesis, occurs when galaxies pass near each other. Some of the hot gas in the halo of the less massive of the two galaxies will be "stripped" away when the galaxies pass near each other, and this gas will join the gas of the more massive galaxy. This will prevent the cold gas in the less massive galaxy from being replenished, eventually stopping star formation in a process known as "strangulation." Close interactions of galaxies will also tend to add energy to the gas in both of these galaxies, in what is known as "harassment," which will slow down the process of star formation (Tinsley and Larson, 1979, Moore et al., 1996, Balogh and Morris, 2000, van den Bosch et al., 2008, Kawata and Mulchaey, 2008).

---

[2]The "early-type" description for galaxies does not refer to a temporal relation between "early-" and "late-type" galaxies, nor is it in fact a misnomer based on a perceived temporal relation. When Edwin Hubble classified galaxies on the "Hubble Fork," he took these terms from the spectra classifications of stars, in which the terms referred to positions along the spectral sequence. In the case of galaxies, they refer to positions along the sequence of increasing complexity: "early-type" galaxies, or ellipticals, appear relative simple, while "late-type" galaxies, or spirals, appear much more complex (Baldry, 2008).

Given that ram pressure stripping has less effect in galaxy groups, and major mergers may not be sufficiently frequent to explain the observed abundance of red galaxies in groups, tidal stripping must be considered as a possible reason that galaxies in groups tend to be redder than field galaxies. There is limited evidence of this, however, due to the difficulty of detecting galaxy groups, and then determining whether or not stripping has taken place within them. The approach we adopt in this thesis is to look at the dark matter haloes around galaxies within groups, which will be affected by tidal stripping the same way as gas is stripped (Hayashi et al., 2004, Kazantzidis et al., 2004, Springel et al., 2008). We can thus examine the dark matter haloes around galaxies in groups, and compare them to the haloes around galaxies in the field, to determine whether or not tidal stripping occurs in a group environment.

Tidal stripping has been detected with gravitational lensing in cluster environments previously by Limousin et al. (2007) and Natarajan et al. (2009). In both of these papers, the authors looked at a sample of satellite galaxies within cluster environments. The clusters' mass profiles were fit by previous lensing data, and the satellites' halo profiles were then calculated through a maximum-likelihood analysis and compared to the haloes of comparable field galaxies. Limousin et al. (2007) found that satellite galaxies within clusters typically have more compact dark matter haloes than similar field galaxies (truncation radius of ~ 50 kpc compared to ~ 200 kpc for field galaxies), and Natarajan et al. (2009) found that the masses of satellites within ~ 45 kpc apertures are only $\sim 20\% - 50\%$ as massive as similar field galaxies. Both of these results support the hypothesis that tidal stripping has had a significant effect on the dark matter haloes surrounding satellite galaxies.

Prior to the research presented in this thesis, however, the only detection of stripping in a group environment was performed by Suyu and Halkola (2010). They studied a strong-lensing system and determined that tidal stripping did seem to occur around the satellite studied, which lies in a group of mass on the order of $10^{12} M_\odot$. While this result is promising, a broader base of data is needed in order to develop a general understanding of the dark matter properties of satellite galaxies in galaxy groups. Stripping has also been investigated in galaxy groups by Mandelbaum et al. (2006b) and later van Uitert et al. (2011), who attempted to fit modelled galaxy and group lensing signals to samples from the Sloan Digital Sky Survey (SDSS) and Red Cluster Survey 2 (RCS2). Neither set of authors was able to detect tidal stripping, nor were they able to rule out its presence. Here we aim to improve upon these studies with data from the Canada-France-Hawaii Telescope Lensing Survey (CFHTLenS), which is significantly deeper than the SDSS, and hence should provide a stronger lensing signal. In our investigation we also apply a new environment estimator, which is tuned to work for photometric redshifts
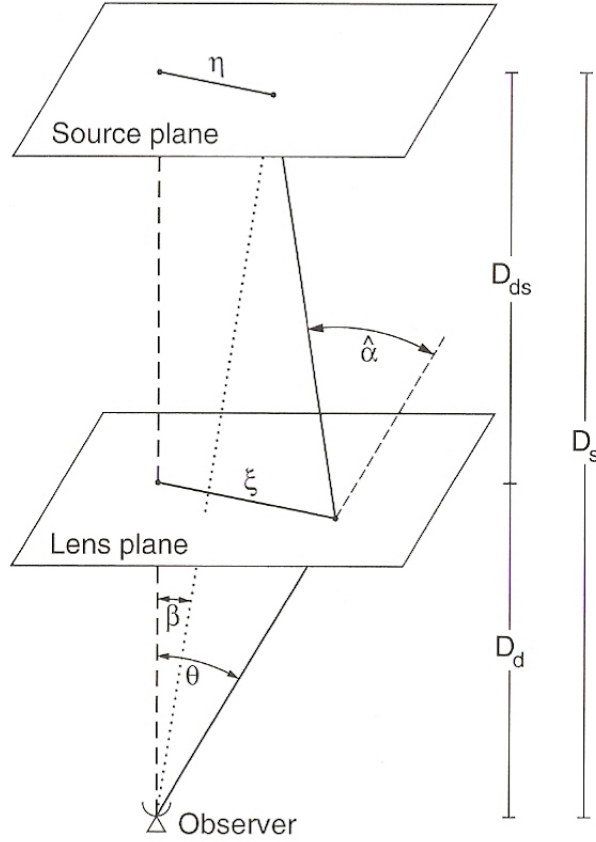
FIGURE 1.3: Figure 12 of Schneider et al. (2006), illustrating the deflection of light due to a gravitational lens, resulting in a change in the source's apparent position. In the diagram, a ray of light from the source is deflected by angle $\hat{\alpha}$ before arriving at the observer. This results in the position angle of the source moving from β, where it would appear if no lensing were present, to θ.

(see Section 2.3.1), and a modified halo model designed to work with this environment estimator (see Section 2.2.2.1).

1.3 Gravitational Lensing

Under Einstein's Theory of General Relativity (GR), gravity operates by curving space-time. As such, it affects not just matter, but all forms of energy, including light. This effect is quite subtle, due to the high speed of light, but the large masses and distances in astronomical surveys allow this effect to be observed via a phenomenon known as "gravitational lensing." The angle of deflection for a light ray travelling past a point mass at a transverse distance from it, $\xi \gg R_{\rm s}$, where $R_{\rm s}$ is the Schwartzschild radius of the mass, can be calculated to be:

$$\hat{\alpha} = \frac{4G_{\rm c}M}{\xi c^2},$$

(1.31)

26

where $\hat{\alpha}$ is the resulting deflection angle and M is the mass of the lensing object. Note that a similar equation can be calculated through classical mechanics, through considering the change in momentum of a photon as it passes near a lens, except with a factor of 2 in the numerator instead of 4. This extra factor of 2 arises purely through GR, and this fact allowed gravitational lensing measurements to be used as some of the earliest empirical evidence for GR by Dyson et al. (1920).

For the purposes of the discussion here, we assume that the source radiation encounters only one lensing event before reaching the observer. In reality, each source will be lensed by multiple objects before reaching the observer, and even in an isotropic universe, the effects of these multiple deflections do not perfectly cancel out Brainerd (2010).

The effects of gravitational lensing can be most easily calculated under the "thin lens" approximation, which assumes that the thickness of the lensing object along the line of sight is negligible compared to the distance from the observer to the lens and the distance from the lens to the source. In this scenario, we can calculate the deflection angle $\hat{\alpha}$ at a position ξ in the lens plane in terms of the surface mass density distribution $\Sigma(\xi')$:

$$\vec{\hat{\alpha}} = \frac{4G_{\mathrm{c}}}{c^2} \int d^2\vec{\xi}' \Sigma(\vec{\xi}') \frac{\vec{\xi} - \vec{\xi}'}{\left|\vec{\xi} - \vec{\xi}'\right|^2} \tag{1.32}$$

(Schneider et al., 2006).

Let us now assume that light is emitted from the source at position η relative to the origin in a plane perpendicular to the line of sight and is deflected by the lens plane at position ξ, as illustrated in Fig. 1.3. Let D_{d} be the angular diameter distance from the observer to the lens, D_{s} be the angular diameter distance from the observer to the source, D_{ds} be the angular diameter distance from the lens to the source, β be the undeflected position angle of the source, and θ be the deflected position angle of the source. If we make the assumptions that all angles are small, and so $\sin\hat{\alpha} \approx \tan\hat{\alpha} \approx \hat{\alpha}$, we can say from geometrical considerations that:

$$\vec{\eta} = D_{\mathrm{s}}\vec{\beta}$$
$$\vec{\xi} = D_{\mathrm{d}}\vec{\theta}$$
$$\vec{\eta} = D_{\mathrm{s}}\vec{\theta} - D_{\mathrm{ds}}\vec{\hat{\alpha}}(\vec{\xi}). \tag{1.33}$$

This then implies that:

$$\vec{\beta} = \vec{\theta} - \frac{D_{\mathrm{ds}}}{D_{\mathrm{s}}}\vec{\hat{\alpha}}(D_{\mathrm{d}}\vec{\theta}). \tag{1.34}$$

This can be rewritten as the lens equation:

$$\vec{\beta} = \vec{\theta} - \vec{\alpha}(\vec{\theta}), \tag{1.35}$$

27

where:

$$\vec{\alpha}(\vec{\theta}) = \frac{1}{\pi} \int d^2\vec{\theta}' \kappa(\vec{\theta}') \frac{\vec{\theta} - \vec{\theta}'}{\left|\vec{\theta} - \vec{\theta}'\right|^2}, \tag{1.36}$$

and $\kappa(\vec{\theta})$ is the "convergence," defined as:

$$\kappa(\vec{\theta}) = \frac{\Sigma(D_{\mathrm{d}}\vec{\theta})}{\Sigma_{\mathrm{cr}}}, \tag{1.37}$$

and where the critical surface density Σ_{cr} is:

$$\Sigma_{\mathrm{cr}} = \frac{c^2}{4\pi G_{\mathrm{c}}} \frac{D_{\mathrm{s}}}{D_{\mathrm{d}} D_{\mathrm{ds}}} \tag{1.38}$$

(Schneider et al., 2006).

Equivalently, we can define a lensing potential:

$$\phi(\theta) = \frac{1}{\pi} \int d^2\vec{\theta}' \kappa(\vec{\theta}') \ln\left|\vec{\theta} - \vec{\theta}'\right|, \tag{1.39}$$

which gives us $\nabla^2\phi = 2\kappa$ (Schneider et al., 2006).

Gravitational lensing can be classified into three regimes: strong lensing, in which distortions in a single light source are detectable with high signal-to-noise (S/N); weak lensing, in which distortions in an ensemble of sources can be detected with statistically significant S/N; and microlensing, in which temporary magnification of a source can be detected as a mass traverses in front of it. Weak lensing is the primary focus of this thesis, and so we will discuss it in-depth in Section 1.3.1, and present a brief overview of strong lensing and microlensing here.

Strong gravitational lensing can appear in a few different forms, depending on the geometry of the structure acting as a lens. A source object with a small enough projected distance from a lens may appear elongated and curved, forming an arc, as can be seen for instance in the background of the cluster Abell 2218 (Kneib et al., 1996). If the lens is axisymmetric, and the source lies behind it at the right distance, the source might even appear as a ring encircling the lens, known as an "Einstein Ring." This can be seen with B1938+666, the first complete ring discovered (King et al., 1998), among others. Rings are relatively rare, though, as they require an axially-symmetric lens mass distribution. However, when the lens can be roughly modeled as a quadrupolar mass distribution (such as an elliptical projected mass density), the source will be multiply imaged, forming a total of three or five images depending on the alignment (though one of these images will often be hidden behind the lens object). This effect can be prominently seen in QSO 2237+0305, the "Einstein Cross" (Crane et al., 1991).

Strong lensing systems can be used to investigate either the mass distributions of the lenses, or, as lensing magnifies background objects, as cosmic telescopes which allow us to investigate the properties of lensed objects at extremely high redshift (up to $z \sim 8-12$). In the former case, the geometry of strong lensing detections provides us with high S/N determinations of the mass distributions of lenses, allowing measurements of cluster masses, as well as evidence for dark matter substructure within clusters (Tyson et al., 1998, among others). In the latter case, strong lensing allows us to observe objects at early stages of the universe, including some quasars near the epoch of reionization, giving us insight into early stages of star and galaxy formation. For instance, MACS0647-JD, a galaxy at estimated redshift ~ 11 is visible because of the magnification from the foreground cluster MACS J0647.7+7015 (Coe et al., 2013).

Microlensing is performed in a greatly different manner from strong or weak lensing. Rather than searching for existing lensing systems, microlensing is performed by monitoring sources over a period of time, and recording the change in their luminosities. When a transient passes in front of the source, the source's luminosity will be temporarily increased. The frequency and amplitude of such events can be used to estimate the number density and masses of typical transients.

Microlensing has proven useful in ruling out one class of dark matter, known as Massive Compact Halo Objects (MACHOs[3]). While the existence of dark matter was strongly suspected for a long time, it was not known if it was composed of baryonic matter which did not radiate light, such as black dwarves, asteroids, and rogue planets (MACHOs), or whether it was composed of exotic particles (WIMPs). In the former case, these objects would be expected to move throughout the Galaxy and occasionally pass in front of luminous sources, magnifying their light through lensing. In the latter case, the distribution of WIMPs would be too smooth for any microlensing detections to be possible from them. Microlensing surveys were able to detect the frequency of MACHO transitions, and they put a firm upper limit on the amount of dark mass which could be explained due to MACHOs, which was much lower than the known amount of dark matter in the galaxy (Alcock et al., 2000). This implied that there had to be some exotic particle which comprised dark matter. More recently, microlensing has also been used to find faint binary companions to stars, and even exoplanets (Bond et al., 2004).

1.3.1 Weak Lensing

In the so-called "weak lensing" regime, the effect of gravitational lensing manifests as a coherent distortion of the shapes of background galaxies, stretching them tangential

---

[3]In contrast to Weakly-Interacting Massive Particles, "WIMPs."

to the foreground object, in an effect known as "shear." Although the variation in the intrinsic shapes of background galaxies is significantly larger than the shear caused by foreground objects, the shape of any given background galaxy will still provide an unbiased, albeit low signal-to-noise, estimate of the local shear. This makes it possible to gather usable data by stacking a sufficient number of lens galaxies together.

In practice, shear is usually observed and measured through the dimensionless parameter $\gamma_{\rm t}$, known as the tangential shear. In the weak regime, the distortion of a source image can be characterized by the Jacobian matrix of the lensing potential (see Equation (1.39)):

$$\frac{\partial \beta}{\partial \theta} = \left(\delta_{ij} - \frac{\partial^2 \phi(\theta)}{\partial \theta_i \partial \theta_j} \right) = \begin{pmatrix} 1 - \kappa - \gamma_1 & -\gamma_2 \\ -\gamma_2 & 1 - \kappa - \gamma_1 \end{pmatrix}, \tag{1.40}$$

where γ_1 and γ_2 are the components of the shear polar (Schneider et al., 2006). For a circularly-symmetric mass distribution, source images will be sheared in a direction perpendicular to the lens-source vector, and so the value of interest is the tangential component of the shear, $\gamma_{\rm t}$.

The tangential shear $\gamma_{\rm t}$ can be estimated from the mean tangential ellipticity $e_{\rm t}$ of source objects in annuli around a sample of lenses, where:

$$e_{\rm t} = -\frac{a - b}{a + b} \cos\left(2\phi\right), \tag{1.41}$$

(Schneider et al., 2006) where a and b are the semimajor and semiminor axes of the source, and ϕ is the relative angle of the source's semimajor axis and the vector from the lens to the source. If we assume that sources are intrinsically randomly-oriented on the sky, we can relate $\gamma_{\rm t}$ to $e_{\rm t}$ through:

$$\gamma_{\rm t} = (1 - \kappa) \langle e \rangle \tag{1.42}$$

(Schneider et al., 2006).

However, as the magnitude of $\gamma_{\rm t}$ depends on the redshifts of both the source galaxy and the lens, for this thesis we will use the measurement $\Delta\Sigma$, which depends only on the surface mass density of the lens objects. The tangential shear γ_t is related to this surface mass density through:

$$\langle \gamma_t \rangle = \frac{\overline{\Sigma(< r)} - \overline{\Sigma(r)}}{\Sigma_{\rm cr}} \equiv \frac{\Delta\Sigma}{\Sigma_{\rm cr}}, \tag{1.43}$$

(Miralda-Escude, 1991a) in a circle of any size r around any given point, where $\Sigma_{\rm cr}$ is defined as in Equation (1.38), $\overline{\Sigma(< r)}$ is the surface density averaged for all points contained within this circle, and $\overline{\Sigma(r)}$ is the surface density averaged for all points on

the edge of this circle. This prescription works even for mass distributions that are not axisymmetric, as long as all points in a given annulus around a lens object are stacked together (Schneider et al., 2006).

Weak lensing can be used in many different mass regimes. Galaxy-galaxy lensing, where both the sources and lenses are galaxies, can be used to measure the mean mass distributions of an ensemble of galaxies, and it is been used to confirm that the dark matter haloes around galaxies follow an NFW-type (Navarro et al., 1997) profile (Hoekstra et al., 2004, Kleinheinrich et al., 2006, Mandelbaum et al., 2008). Weak lensing has also shown that this profile can be used for galaxy clusters (Mandelbaum et al., 2006a, 2008). More generally, weak lensing can be used to estimate mass-to-light ratios of galaxies (Brainerd et al., 1996, Hudson et al., 1998, Guzik and Seljak, 2002, Leauthaud et al., 2010, van Uitert et al., 2011, Velander et al., 2013) and how they evolve over redshift (Hudson et al., 1998, Leauthaud et al., 2012a, Coupon et al., 2012, Tinker et al., 2012), as well as provide insight into the fraction of galaxies which reside in groups and clusters (van Uitert et al., 2011, Velander et al., 2013).

Most dramatically, weak lensing can be used to generate maps of the mass distributions in galaxy clusters. This technique proved particularly valuable with the mass mapping of the Bullet Cluster (Clowe et al., 2004), in which it was demonstrated to high confidence that the mass within this systems was separated from the gas (where most of the mass would be if there were no dark matter). This provided clear and convincing evidence that dark matter was real, and modified gravity theories were likely unnecessary.

Weak gravitational lensing can also be used to measure "cosmic shear." Cosmic shear consists of coherent alignment in the shapes of distant galaxies caused by the coherent weak lensing effects of large-scale structure in the universe. As these effects are a large-scale phenomenon (most prominent on arcminute to degree scales), and it is not *a priori* known which foreground structures cause this lensing, cosmic shear most prominently seen in Fourier space or correlation functions (Blandford et al., 1991, Miralda-Escude, 1991b, Kaiser, 1992). As the lensing signal resulting from large-scale structure is directly related to the extent, mass, and abundance of such structure, cosmic shear measurements allow a direct probe of cosmological constants of the universe (Miralda-Escude, 1991b, Bernardeau et al., 1997, Massey et al., 2007). This effect is an order of magnitude smaller than the shear from galaxy-galaxy lensing, and it is also particularly sensitive to systematic errors. For instance, if there is a systematic elongation of all galaxies in a field along one axis, when lens-source pairs are averaged together, this elongation will cancel out (approximately as many pairs will be parallel to this systematic axis as will be perpendicular to it). However, since cosmic shear measurements use alignment between sources, this systematic error will carry through to the final results. Advanced

methods of shear measurement, such as the *lens*fit algorithm (Miller et al., 2012), are needed to minimize the effects of systematic errors. This has allowed cosmic shear to recently provide tight constraints on various cosmological parameters in the CFHTLenS survey (Erben et al., 2013, Kilbinger et al., 2013, Heymans et al., 2013).

1.4 Photometric Redshifts

For distant galaxies, redshift measurements are the most accurate and practical method to estimate distance from us. Spectroscopic redshifts (spectro-zs) use detections of emission and absorption lines to measure redshifts. Spectro-zs are able to attain redshift errors limited only by the signal-to-noise and resolution of the detection, but the presence of peculiar velocities among galaxies limit how accurately redshifts can be interpreted as a distance measurement. Peculiar velocities of galaxies in groups and clusters are of the order $\sim 100 - 300\,\mathrm{km/s}$, equivalent to a blurring in redshift space of order ~ 0.0001. The effect of this on group-finding algorithms is discussed in Section 1.5 below.

However, while spectro-zs are very accurate and useful, they take a very large amount of telescope time to acquire, and their high degree of accuracy is not always necessary. Thus, the alternative method of photometric redshifts (photo-zs), which are orders of magnitude less precise than spectroscopic redshifts (spectro-zs), but take orders of magnitude less telescope time to obtain, can become useful.

Photo-zs require observations of a galaxy in a minimum of 3 filters, and more typically 4 or 5 (such as the *UVRI* or *ugriz* filter sets) are used. From these, a photo-z algorithm will attempt to map the galaxy's filter data to its redshift. Modern methods can achieve redshift errors as low as $\sigma_\mathrm{z} \sim 0.04$[4] with the *ugriz* filter set, for galaxies with $i < 22.5$ (Hildebrandt et al., 2012), and this has been improved to as low as $\sigma_\mathrm{z} \sim 0.01$ when using a set of 30 filters, as in the COSMOS-30 sample (Ilbert et al., 2009).

There are two classes of photo-z algorithms, which work in greatly different manners: artificial neural network (ANN) methods and template-based methods. ANN methods work by simulating the connections with a neural network, to map a galaxy's photometry to its redshift. These methods require no physical assumptions about the spectra of galaxies, or even calculations of the physics of redshifting, but they do require a sample of galaxies with both photometry and spectroscopic redshifts in order to "train" the method to estimate redshifts. These methods can be seen, in essence, as fitting a function of tens of parameters to sample data.

---

[4]Throughout this thesis we use the convention that σ_z refers to the root-mean-squared scatter of measured photo-zs relative to spectro-zs δz, as opposed to it referring to $\delta z/(1 + z)$.

In ideal conditions, when a training set of galaxies with spectro-zs is available that well approximates the set of galaxies whose redshifts are to be measured, ANN methods typically out-perform template-based methods, having lower bias and scatter in their redshift estimates. However, this ideal set of circumstances is rare in practice. Ideally, a training set would need to be randomly drawn from the galaxies in the photometric survey, but this typically is not practical. Photo-z surveys typically cover much wider regions of the sky than spectroscopic surveys, and a random sample of their galaxies would be too spread out to make gathering spectro-zs for them efficient; it would be more practical to simply gather spectro-zs for most galaxies in the survey. Rather, a more likely scenario would be gathering spectro-zs for a small patch of the wider survey. This can reasonably approximate the entire survey, although, depending on the size of the survey, galactic extinction may vary enough over its size to introduce errors into the photo-z estimation. But even a random sample of a patch of a wider field is not very likely to be useful; spectro-z surveys are typically limited to a brighter magnitude than the photo-z data, which introduces large biases into the training set. As such, in almost all practical circumstances, ANN methods will not perform as well as template-based methods (Collister and Lahav, 2004, Abdalla et al., 2011).

Template-based photo-z methods use assumptions about the spectral energy distributions (SEDs) of galaxies of various types to estimate their redshifts. Template methods use ~ 5 or more SED templates, which approximate the SEDs of various types of galaxies at redshift zero. These templates are then redshifted to various test redshifts, and expected photometry for each template at each test redshift are calculated, based on the filter's sensitivity and the redshifted SED. This expected photometry can then be used as a look-up table with which to compare the photometry for each galaxy. A χ^2 test or similar comparison can then be used to find the best-fit redshift and template for the galaxy, as well as a probability distribution function for each, which allows one to estimate the error in the redshift estimate.

One notable issue with photo-z estimation is the possibility of catastrophic errors, where a galaxy's estimated redshift differs from its actual redshift by a large amount (on the order of $\sigma_z \sim 0.2$ or more). To see why this is possible, consider the case of a red galaxy. The SED for a red galaxy shows two major "breaks," where there is a sharp jump in the SED, one at 912 Å and another at 4000 Å. This allows for possible degeneracy between a $z \sim 1$ red galaxy and a $z \sim 6$ red galaxy, as illustrated in Fig. 1.4. These cases are relatively, rare, however, and typically fewer than $\sim 5\%$ of galaxies at low redshift ($z \lesssim 1$) will have catastrophic errors in their photo-z estimates (Hildebrandt et al., 2012).
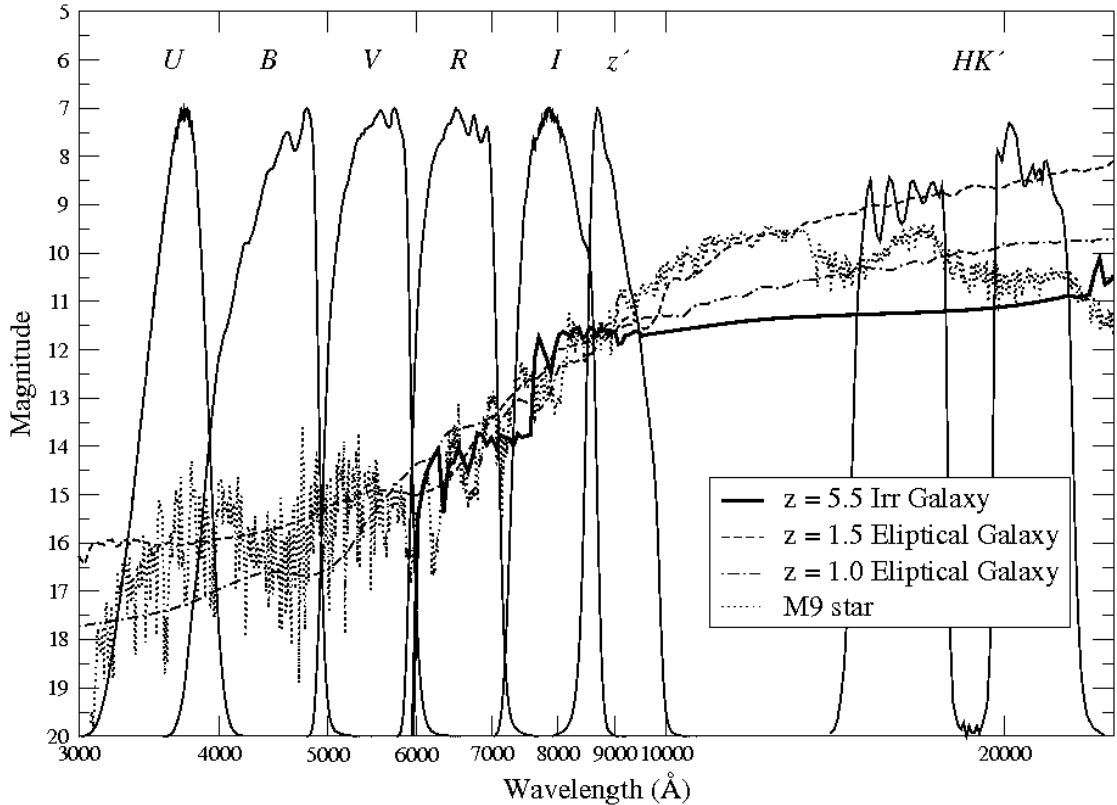
FIGURE 1.4: Figure 15 from Capak et al. (2004), illustrating three possible galaxy SEDs which are highly-degenerate. Without high-quality U data, it might be impossible to discriminate between the three possible redshifts for the galaxy.

1.5 Group-Finding Methods

While it is simple to provide a qualitative description of a galaxy group - a gravitationally bound structure of multiple galaxies - it is more difficult to identify such structures in the universe. We can start with the physics of structure formation. If we apply Equation (1.5) at $\eta = \frac{3}{2}\pi$, which is the time at which the collapsing structure will be supported by its virial energy, we find that structures will virialize when their density is $\sim 174\times$ the background density of the universe (Padmanabhan, 1993). We can thus define a group as a clustering of galaxies which has a galaxy number density $\sim 200\times$ the background density of the universe, and tune group-finding algorithms to search for galaxy overdensities which satisfy this criterion.

With this in mind, one of the most basic group-finding algorithms is the friends-of-friends (FoF) algorithm. This algorithm works by starting a seed from an individual galaxy, and then searching for all other galaxies that lie within a linking length r_l of it. These galaxies are then added to a group with the seed galaxy. The algorithm then iterates, adding all galaxies within distance r_l of any galaxy in the group until no more galaxies can be added. If the linking length is set to 1/5 the mean inter-galaxy separation, then this will

result in the algorithm detecting groups that have an overdensity of $\sim (1/5)^{-3} = 125$ at their edges.

FoF algorithms work well, but not perfectly, in simulations; they can overlink galaxies or dark matter particles and merge structures that should properly be considered as separate groups. In the real universe, errors in distance estimates to galaxies (due to peculiar velocities) introduce even more error into the groups detected by FoF algorithms, even with spectroscopic redshifts. Groups appear to be elongated along the line of sight, in what is known as the "fingers of God" effect. If FoF algorithms are run without correcting for this effect, they will greatly underestimate the population of groups. The standard method for correcting for this effect is to allow the linking length in the redshift direction to be much larger than in the other directions. If the linking length in z is increased by an amount equivalent to the velocity dispersion within a typical group, the algorithm will better identify group populations. This does lead to a risk of over-linking, however, and adding in "interlopers," field galaxies that are projected behind or in front of the group, but get mistakenly classified as being in the group, and so the linking length must be tuned to balance this effect against under-counting group galaxies. Typically, an FoF algorithm can simultaneously attain $\sim 80\%$ purity and completeness for its catalogue, though it can trade between purity and completeness if one is more desirable than the other for a given goal (Robotham et al., 2011).

In dark-matter simulations, FoF algorithms are typically run on the dark matter particles, instead of galaxies; if the simulation includes galaxies in a semi-analytic model, they will be added only after haloes have been identified. The algorithm then classifies the dark matter particles into haloes, which can be traced over the evolution of the simulation. This is not enough to fully populate a simulation with galaxies, however; in a group of galaxies, the FoF algorithm will only identify one shared halo for the group. A further refinement is needed to identify subhaloes within a larger halo. The most commonly-used method for this is the SUBFIND algorithm (Springel et al., 2001). This algorithm works by first creating a density estimate at the location of each dark matter particle, using the distance to the nth (tunable, typically a bit more than 10) nearest neighbour. These densities are then used to interpolate a density field, and substructure within the field will be defined by a self-bound region enclosed by an isodensity contour which traverses a saddle point in the density field. This is performed by starting with a high global density threshold and determining all contours at this density. This threshold is then lowered, and saddle points are identified when two contours merge to become a single contour. The algorithm then checks to ensure that the regions identified in this matter are self-bound. These regions, aside from the one identified with the primary halo, are then identified as subhaloes. They can then be populated with galaxies through

a semi-analytic model, generating a full galaxy catalogue and group assignments for all galaxies.

When spectroscopic redshifts are not available in galaxy surveys, FoF algorithms are not viable without extensive modifications. One possible modified FoF algorithm proposed by (Li and Yee, 2008) is the probability friends-of-friends algorithm (pFoF). As in a traditional FoF algorithm, this algorithm starts with a single galaxy as a seed group, using every galaxy in turn to start its own seed. The algorithm then progressively adds galaxies to the seed group using a probability comparison, based on the full probability distribution functions (PDFs) for the redshifts of the group and galaxy:

$$P_{ij} = \frac{\int_{z_{\min}}^{z_{\max}} P_i(z)P_j(z)dz}{P_{ij,\max}}, \tag{1.44}$$

where $P_i(z)$ is the PDF of the group, $P_j(z)$ is the PDF of the galaxy, and $P_{ij,\max}$ is a normalization factor, determined through the maximum value of $\int_{z_{\min}}^{z_{\max}} P_i(z-z_0)P_j(z)dz$ for $z_{\min} < z_0 < z_{\max}$. This can be envisioned as shifting one of the PDFs so they overlap as much as possible; the calculated P_{ij} is then the ratio of the actual integral to how large it could in principle be if the two PDFs were ideally aligned. If this galaxy passes a cut on transverse linking length and minimum P_{ij}, it is added to the group and the PDF of the group is updated to be:

$$P_i(z) = \frac{\Pi_k P_k(z)}{\int_{z_{\min}}^{z_{\max}} (\Pi_k P_k(z')) \, dz'}, \tag{1.45}$$

where $P_k(z)$ represents the PDF of each galaxy now within the group. This process is then iterated until no more galaxies can be added to the group and is then repeated for the next galaxy in the catalogue (even if it is already a member of a group). The algorithm thus creates a group for each galaxy, which it then checks for duplicates. Duplicate groups are merged with the most likely memberships, and groups of low overall significance are removed from the group catalogue.

As the pFoF algorithm works on a friends-of-groups basis, it is less likely to make spurious group detections than a standard FoF algorithm is, if redshift errors are significant. The overall PDFs of groups provide a ready method to determine how likely a detection is to be spurious, and groups with overly-broad PDFs are thus discarded. Li and Yee (2008) claim $\sim 90\%$ purity and $> 99\%$ completeness for groups of more than eight members.

An alternative method we proposed in Gillis and Hudson (2011) is the "Photo-z Probability Peaks" (P3) algorithm. This algorithm will be discussed in detail in Section 2.3.1, but it can be summarized as generating a 3D density distribution of galaxies and identifying peaks in this distribution as potential groups. The threshold signal-to-noise (S/N)

used to identify groups can be tuned for very high purity, but this comes at the expense of completeness.

Group identification can be improved if some assumptions are made about the physical properties of groups, although this risks biasing the sample toward certain classes of objects. For instance, clusters are known to typically emit strong X-ray radiation through the hot gas contained within their ICMs. If X-ray observations are available, detection of strong X-ray emissions can be used to generate a very pure and complete cluster catalogue (Mulchaey and Zabludoff, 1998). X-ray detections also allow ready detection of the centre of the cluster's dark matter halo, which can greatly aid in certain types of lensing analysis, such as the method we propose in Section 3.2. However, use of X-ray detections will limit the group sample to groups with significantly dense ICMs. It is likely that interesting physics happens in the transition between groups with and without a detectable ICM, but this cannot be investigated if the group sample is limited to only groups with detected ICMs.

Alternatively, groups can be detected using the presence of a bright cluster galaxy (BCG) (Koester et al., 2009) or a strong concentration of red galaxies (Gladders and Yee, 2000). As with X-ray detections, though, these methods will bias the resultant group catalogue to one which contains the features they search for. Groups which lack a BCG or a strong concentration of red galaxies will not appear in such catalogues, but it is necessary to include these groups in a sample if one wishes to analyse the physics which may cause the formation of a BCG or red galaxies.

One issue common to all methods that rely on photometric redshift estimates is that, while they can show high purity and/or completeness in their detections of groups, this does not extend to a pure and complete assignment of galaxies to groups. While with spectroscopic catalogues $\sim 80\%$ purity and completeness is typically possible, photo-z methods typically cannot surpass $\sim 50\%$ purity and completeness of their assignments of galaxies to groups without trading off either purity for completeness or completeness for purity. For our purposes, we value purity more than completeness and, in particular, the purity of the satellite selection. Using a modified version of our P3 algorithm, we are able to attain $\sim 60\%$ purity and $\sim 45\%$ completeness for identifying satellites in our simulated catalogue as such, as tested against the group catalogues from the simulations.

1.6 Thesis Summary

In Chapter 2 of this thesis, we present the details of the surveys and simulated catalogues used, we discuss the methodology we use to investigate tidal stripping when photometric

redshift data are available, and we present the results of our investigation of tidal stripping in the CFHTLenS catalogues. In Chapter 3, we discuss methods that can be used to investigate tidal stripping if spectroscopic redshift information and spectroscopically-derived group catalogues are available, and we present analysis of these methods. We conclude in Chapter 4, and details of some of the approximations used throughout this thesis are presented in Appendix A. In Appendix B, we present preliminary results from the application of our methodology to the Sloan Digital Sky Survey, Data Release 8 dataset.

This thesis is based primarily on work published in Gillis et al. (2013b) and Gillis et al. (2013a). Chapter 2 is composed primarily of material from Gillis et al. (2013a), and Chapter 3.2 is composed primarily of material from Gillis et al. (2013b). Certain paragraphs from these papers are also included in the introduction and conclusion to this thesis, and the data section from Gillis et al. (2013b) is mostly merged into Section 2.1 and Section 2.2. Appendix A is composed of the appendix to Gillis et al. (2013b). Appendix B is composed of unpublished work, which may be published at a later date. All material in this thesis was originally written by the author, with proofreading and recommendations from collaborators and members of the thesis committee.

For consistency with the Millenium Simulation, we use the following cosmological parameters: Hubble parameter at redshift zero $H_0 = 73\ \mathrm{km\,s^{-1}\,Mpc^{-1}}$, density parameters of matter, dark energy, and baryonic matter $\Omega_{\mathrm{m}} = 0.25$, $\Omega_{\Lambda} = 0.75$, and $\Omega_{\mathrm{b}} = 0.045$ respectively. All stated magnitudes are in the AB system. Since there is no clear division between galaxy groups and galaxy clusters, we use the terminology "galaxy groups" throughout this thesis, even though some of the structures we refer to as such would be more commonly deemed clusters. When masses are quoted in this thesis, M is used to refer to the total (halo + baryonic) mass of a galaxy or group, and m is used to refer to the stellar mass of a galaxy, unless otherwise specified. When radial measurements are used in this thesis, R refers to a projected, 2D proper distance, and r refers to a 3D distance, unless otherwise specified. All masses are in units of solar masses $M_{\odot}$ unless otherwise specified.

Chapter 2

Methods Using Photometric Redshifts

In this chapter we discuss methods to detect the presence or absence of tidal stripping, assuming only photometric redshift data are available, and we present an analysis of data from the CFHTLenS survey using these methods. In Section 2.1, we discuss the galaxy catalogue we use, drawn from the CHFTLenS, as well as how we process this catalogue and select subcatalogues of lens galaxies. In Section 2.2, we discuss the simulated galaxy catalogues we use for our analysis, including how the galaxy selections are prepared to match our observed data and how we simulate lensing signals for these simulated catalogues. In Section 2.3, we discuss methods we use to estimate the environments of galaxies, as well as describe how the sample is divided into matched high-density and low-density subsamples, and we also present the statistics of the galaxies in the HDE and LDE samples. In Section 2.4, we detail the model we use to fit the lensing signals measured in our analysis, and in Section 2.5, we discuss how we fit this model to the data. We present the results of our analysis in Section 2.6.

2.1   Observations

CFHTLenS is a 154 deg^2 survey (125 deg^2 after masking) (Erben et al., 2013), based on the Wide component of the Canada-France-Hawaii Telescope Legacy Survey (Heymans et al., 2012), which was observed in the period from March 22nd, 2003 to November 1st, 2008, using the MegaCam instrument (Boulade et al., 2003). It consists of deep, sub-arcsecond, optical data in the $u^*g'r'i'z'$ filters. CFHTLS-Wide observations were carried out in four high-galactic-latitude patches:

- W1: 72 pointings; RA=$02^h18^m00^s$, Dec=$-07^d00^m00^s$

- W2: 25 pointings; RA=$08^h54^m00^s$, Dec=$-04^d15^m00^s$

- W3: 49 pointings; RA=$14^h17^m54^s$, Dec=$+54^d30^m31^s$

- W4: 25 pointings; RA=$22^h13^m18^s$, Dec=$+01^d19^m00^s$.

As contamination from foreground stars and galaxies, cosmic rays, and other observational limitations can contribute to inaccuracy in weak lensing measurements, it was necessary to mask out unusable regions of the observed fields. The `automask` tool (Dietrich et al., 2007, Erben et al., 2009) was used to automatically generate masks for the fields, and this was compared with human-corrected masks. These latter masks were developed by a team including the author, who expanded the `automask` masks to cover all suspicious regions near contaminating objects. A lensing catalogue quality assessment was performed, which found that the `automask` masks were sufficient for science purposes and manual correction is not necessary (Heymans et al., 2012, Erben et al., 2013).

Shapes of background galaxies in the unmasked regions were measured with the *lens*fit shape measurement algorithm for galaxies with $i' < 24.7$ (Miller et al., 2012), giving an effective galaxy density of 11 sources/arcmin^2 in the redshift range $0.2 < z_{\mathrm{phot}} < 1.3$ (Heymans et al., 2012). For the analysis in this thesis, we use all fields in the survey, not simply those that passed the systematics tests for cosmic shear measurements (Heymans et al., 2012). It has been demonstrated that fields with systematics that may affect cosmic shear have no effect on galaxy-galaxy lensing measurements (Velander et al., 2013), and the analysis in this thesis requires as many lens-source pairs as possible.

Photometric redshifts for the survey were estimated with the *BPZ* code (Benítez, 2000). *BPZ*, when used alongside accurate galaxy SEDS, was one of the redshift codes found to perform best by the PHoto-z Accuracy Testing (PHAT) collaboration (Hildebrandt et al., 2010). The PHAT team tested and compared various template- and neural-network-based photo-z codes for precision and accuracy, including contributions from the author in testing the `ZEBRA` code (Feldmann et al., 2006). The accuracy of photo-z measurements for the CFHTLS-Wide survey was improved through homogenizing the PSF through different bands in the CFHTLenS survey. Photo-zs were made available for the entire survey, with a typical redshift uncertainty of $\sim 0.04(1 + z)$ in the redshift range $0.2 < z_{\mathrm{phot}} < 1.3$ (Hildebrandt et al., 2012).

We use the stellar mass estimates described by Velander et al. (2013), obtained by fitting spectral energy distribution (SED) templates, following the method of Ilbert

et al. (2010). These stellar masses were found to be in rough agreement with deeper data such as WIRDS, which includes NIR filters (Bielby et al., 2012), up to $z = 0.8$.

Since we perform a differential measurement between samples, an overall bias in the stellar masses would not affect our results. It is possible, however, for a relative bias in the stellar mass estimates of red and blue galaxies to impact our results. This possibility is investigated further in Section 2.6.4.1.

For this thesis, we use all unmasked galaxies with photometric redshifts in the range $0.2 < z_{\mathrm{phot}} < 0.8$ as lens candidates. We divide these into HDE and LDE samples as described in Section 2.3.1.

2.2 Simulations and Models

In this section we discuss the simulations used to generate our galaxy catalogues and our models for the mass distributions of galaxies within these catalogues. In Section 2.2.1, we discuss how we extracted our galaxy catalogues from the Millennium Simulation and the properties of these catalogues. In Section 2.2.2 we discuss the mass distributions we assume for dark matter haloes surrounding the galaxies in our catalogues; in Section 2.2.2.1, we discuss the mathematical form of the model we use, and in Section 2.2.2.2, we discuss the different models we use for the presence or absence of tidal stripping, along with other datasets we use for comparison purposes. In Section 2.2.3, we discuss how we simulate shears and ellipticities for our source catalogues.

2.2.1 Simulated Catalogues

In order to assess the differences varying stripping models have between their lensing signals, it is easiest to work with a simulated galaxy catalogue, where exact redshifts, masses, mass distributions, and group assignments can be known. In this thesis, we used a semi-analytic galaxy catalogue based on the Millennium Simulation (Springel et al., 2005b) by De Lucia and Blaizot (2007). The Millennium Simulation is a collisionless simulation of $N = 2160^3$ dark matter particles, each with a mass of $8.6 \times 10^8 \ h^{-1}\mathrm{M}_\odot$, in a box with 500 $h^{-1}\mathrm{Mpc}$ sides and periodic boundary conditions. The simulation used the following cosmological parameters: $h = 0.73$, $\Omega_{\mathrm{m}} = 0.25$, $\Omega_{\mathrm{v}} = 0.75$, $\Omega_{\mathrm{b}} = 0.045$, $\sigma_8 = 0.9$, $n = 1$. The simulation used force softening on a scale of 5 h^{-1} comoving kpc. This causes an artificial smoothing of the cores of dark matter haloes, and as a result, density measurements within ~ 50 kpc of a halo's core are unreliable.

	h	Ω_{m}	Ω_{b}	σ_8	n
Millennium	0.73	0.25	0.045	0.9	1
Planck	$0.670^{+.015}_{-.009}$	$0.318^{+.013}_{-.021}$	$0.049^{+.003}_{-.004}$	$0.835^{+.006}_{-.018}$	$0.9619^{+.0057}_{-.0089}$
WMAP*	$0.6933 \pm .0088$	$0.288 \pm .010$	$0.0472 \pm .0010$	$0.830 \pm .018$	$0.971 \pm .010$

TABLE 2.1: A comparison of the cosmological parameters used for the Millennium Simulation with the constraints of Planck (Planck Collaboration et al., 2013) and WMAP (Hinshaw et al., 2012). *For WMAP, we use the constraints including the BAO and H_0 priors, as discussed in (Hinshaw et al., 2012).

The galaxy catalogues used in this thesis consist of lightcones within De Lucia and Blaizot (2007)'s catalogue prepared by Hilbert et al. (2009). These catalogues are complete for $M_{\mathrm{stellar}} > 10^9$ M$_\odot$ and consist of thirty-two 16 deg.^{2} fields. We split these catalogues into sub-catalogues of "lens" and "source" galaxies. The lens catalogues consist of all galaxies in the parent catalogue with $0.05 < z < 0.8$, and the source catalogues consist of all galaxies in the parent catalogue with $r < 24.5$, approximately the limit for shape data in the CFHTLenS (Heymans et al., 2012). We use all galaxies in the lens catalogue for our ray-tracing simulations, The source galaxies have shears calculated from a ray-tracing simulation performed by Hilbert et al., which differs from ours in that it uses the positions of dark matter particles within the Millennium Simulation rather than our halo models (described in Section 2.2.2). As such, it provides a useful comparison to check that our models generate reasonable results.

The resolution of redshift and mass within these catalogues was limited by the number of snapshots of the original simulation which were saved. Sixty-four snapshots were saved in total, of which 23 are below redshift 1.

In order to properly compare results from the Millennium Simulation to observed results, we must first consider how well the Millennium Simulation approximates reality. First, let us consider whether the Millennium Simulation might have difficulty identifying haloes and subhaloes. If it were to exhibit any problems in doing this, it would likely be at the low-mass end, nearest the resolution limit. This can be investigated through a comparison with the similar Millennium-II Simulation, which is identical to the Millennium Simulation in cosmological parameters assumed, but has a volume and particle mass a factor of 125 smaller (the box has 100 h^{-1}Mpc sides and dark matter particles each have a mass of 6.9×10^6 h^{-1}M$_\odot$). For this test, we look to the work of Fakhouri et al. (2010), who tested halo merger rates of haloes and subhaloes in both the Millennium and Millennium-II simulations. The authors found that in the small mass range in which the two simulations overlapped, the agreement between them in all measurements of merger rates tested was excellent. This implies that the number counts of subhaloes in the Millennium Simulation are unlikely to be affected by resolution limits at the low-mass end.

Secondly, let us consider the cosmological parameters assumed for the Millennium Simulation. The most recent constraints on these parameters from the *Planck* (Planck Collaboration et al., 2013) and WMAP (Hinshaw et al., 2012) observations are compared with the parameters used for the Millennium Simulation in Table 2.1. With the exception of Ω_b, all of the listed parameters now differ from observational constraints at at least 2σ significance. As such, we do not expect the measurements from the Millennium Simulation to perfectly match observations. It nevertheless provides a strong qualitative test of the performances of our algorithms.

The dark matter haloes of the Millennium Simulation were populated with galaxies through a semi-analytic model developed by De Lucia and Blaizot (2007). Dark matter haloes are identified through a friends-of-friends algorithm with linking length of $0.2\times$ the mean interparticle separation, and haloes with at least 20 dark matter particles ($M \sim 2 \times 10^{10} M_\odot$) are populated with galaxies. Haloes are also analysed with the SUBFIND algorithm (Springel et al., 2001) to identify subhaloes, and self-bound subhaloes of at least 20 dark matter particles are similarly identified and populated with galaxies. All of these galaxies are labeled with the ID of the dark matter halo or subhalo that contains them. Haloes in adjacent snapshots are identified as descendants or progenitors if they share at least 50% of their dark matter particles, and the galaxies they contain are similarly linked.

In Fig. 2.1 we show a comparison of the stellar mass distributions of galaxies in our simulated catalogues to the CFHTLenS catalogues, assuming the same observational constraints. While the stellar mass distribution is similar, the simulated catalogue shows a peak in the histogram at a higher stellar mass than the CFHTLenS, and then cuts off much more sharply. We discuss the implications of this in Section 2.2.2.1.

We identified galaxies in these catalogues as either "central," "satellite," or "field" galaxies. Central galaxies are galaxies which share a host halo with at least one other galaxy and are labeled by De Lucia and Blaizot (2007) as being at the centre of the group's dark matter halo. Satellite galaxies are galaxies which share a host halo with at least one other galaxy and are not labeled as central galaxies. Field galaxies are galaxies which do not share a host halo with any other galaxy: they are centrals in a halo with no satellites.

We cut our source and lens catalogues to match observations as well as possible. We assign and apply photo-z errors consistent with those in the CFHTLenS and apply the P3 algorithm to the simulated data, and apply magnitude cuts of $i < 24.7$ (simulating the CFHTLenS) to both the lens and source catalogues.
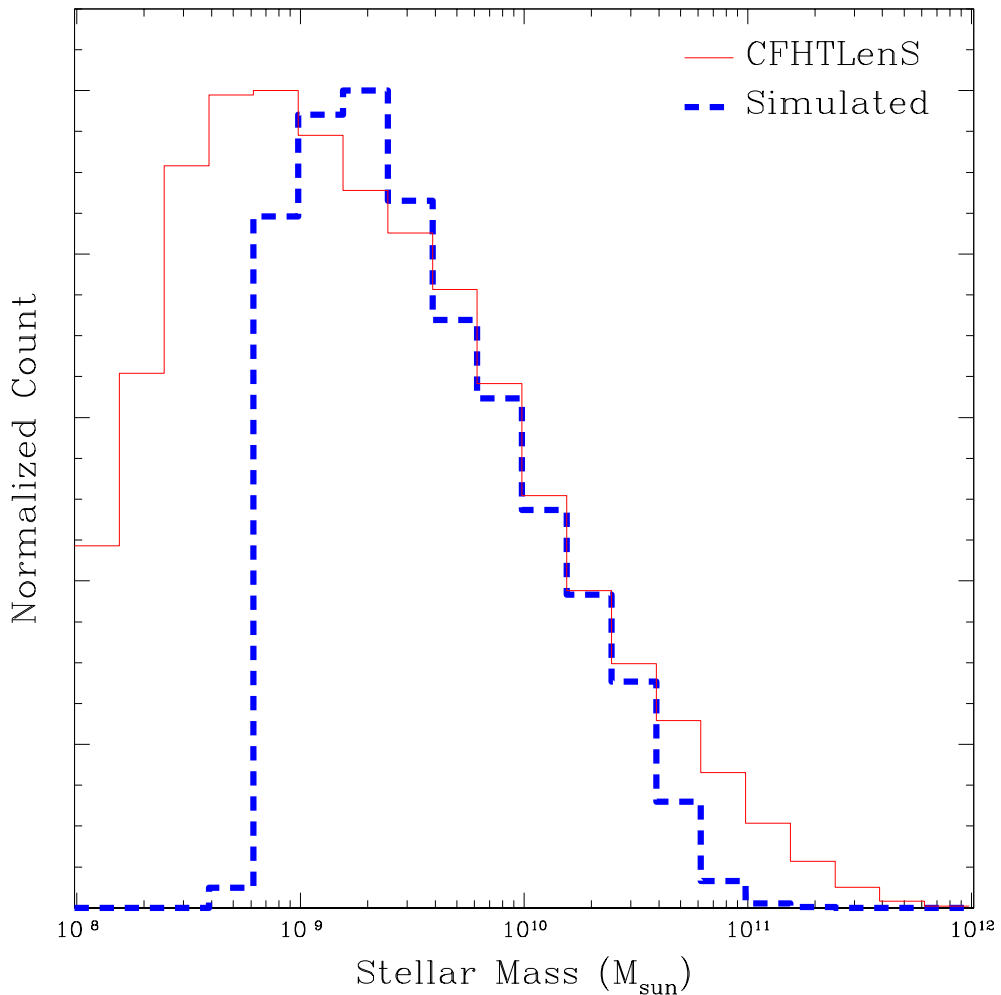
FIGURE 2.1: A comparison of the stellar mass distributions of all galaxies in the simulated catalogues, drawn from the semi-analytic model of De Lucia and Blaizot (2007), and the CFHTLenS catalogues. The simulated catalogue was cut to match the observational limits of the CFHTLenS. Counts are normalized to share a maximum.

For the simulated photometric redshift measurements for these catalogues, we do not directly calculate photo-zs from the simulated galaxy colours in the Millennium simulation. We tested this method using the publicly-available ZEBRA (Feldmann et al., 2006) and *BPZ* (Benítez, 2000) codes for estimating photo-zs, but the resultant redshifts showed extremely large scatter compared to the actual redshifts of the galaxies ($\sigma_z \gtrsim 0.2$), even without simulating any errors in the measured filter magnitudes. This implies that the colours in the Millennium Simulation are not a sufficiently good match for reality to allow use of photo-z codes with them. We thus decided to instead simulate photo-z errors by scattering the simulated redshifts by a Gaussian error, whose size matches the errors in our datasets. This method has the advantage that it is easy to simulate different qualities of photo-z data, although it does have the disadvantage that

it doesn't simulate effects such as catastrophic errors that are present in photometric redshift measurements. However, the high quality of photo-zs in the CFHTLenS sample results in less that 5% of galaxies likely having catastrophic errors. We further minimize the potential contamination from this effect by weighting lens galaxies by their "ODDS" parameter in our analysis. This parameter represents the probability that a galaxy does not have a catastrophic error in its redshift estimate. As such, galaxies with low ODDS are given low weight in our sample to minimize the contribution of catastrophic errors.

2.2.2 Models

2.2.2.1 Halo Models

For ease of calculations, we assume that all dark matter lies within spherically-symmetric haloes[1]. We modeled the mass distributions of all lens haloes as truncated NFW profiles, as defined by Baltz et al. (2009), with a density profile:

$$\rho(x) = \frac{M_0}{4\pi r_{\mathrm{s}}^3} \frac{1}{x(1+x)^2} \frac{\tau^2}{\tau^2 + x^2}, \tag{2.1}$$

where $M_0 = M_{200}(\ln(1+c) - c/(1+c))^{-1}$, $r_{\mathrm{s}} = r_{200}/c$, and $x = r/r_{\mathrm{s}}$. c is the concentration parameter, in principle unique to each halo, and $\tau = r_{\mathrm{tidal}}/r_{\mathrm{s}}$ determines the truncation radius. This model provides an analytic form for the weak lensing signal, as outlined in Baltz et al. (2009). In this thesis, we assume that for haloes that haven't been tidally disrupted, $\tau = 2c$, which implies $r_{\mathrm{tidal}} = 2r_{200}$. This assumption is consistent with results from Hilbert and White (2010) and Oguri and Hamana (2011), the latter of which supports a value of τ between $2c$ and $3c$. We determine c using the mass-concentration relation determined by Neto et al. (2007) for haloes in the Millennium Simulation:

$$c = 4.67 \times \left(\frac{M_{200}}{10^{14} h^{-1} \mathrm{M}_\odot} \right)^{-0.11}. \tag{2.2}$$

To see how weak lensing signals depend on the mass distribution within groups, we experimented with different methods of apportioning a group's mass to its constituent galaxies. The catalogue from De Lucia and Blaizot (2007) provides the total mass of a group's halo (which includes the mass of all subhaloes) at any snapshot and the stellar masses of all galaxies. Note that the stellar mass is not expected to evolve significantly

---

[1]Triaxial models (Jing and Suto, 2002) provide a more accurate representation of real dark matter haloes, but this is not necessary for our purposes. Per Equation (1.43), with a sufficient number of lenses and sources stacked together, the lensing signal of a triaxial halo (which appears elliptical in projection) will be indistinguishable from the lensing signal of a spherically-symmetric halo. This is due to the fact that the noise due to neglecting triaxiality is of order $\sim 20\%$ per pair, while shape noise is 1–2 orders of magnitude larger.

after a galaxy joins a group (Padilla et al., 2009), so if there is a monotonic relation between infalling halo mass and stellar mass, the latter can be used to estimate the mass of the galaxy's dark matter halo prior to joining the group. Here we make this identification using the method of "abundance matching", originally applied to entire haloes (Marinoni and Hudson, 2002, Yang et al., 2003) and later subhaloes (Vale and Ostriker, 2004, Conroy et al., 2006). We use the following formula from Guo et al. (2010) to relate the stellar and halo masses:

$$0.129 \times \frac{m_{\text{halo}}}{m_{\text{stellar}}} = \left(\left(\frac{m_{\text{halo}}}{10^{11.4} \text{M}_\odot} \right)^{-0.926} \right.$$
$$\left. + \left(\frac{m_{\text{halo}}}{10^{11.4} \text{M}_\odot} \right)^{0.261} \right)^{2.44}. \tag{2.3}$$

See Appendix A.1 for details on how we used this formula to calculate m_{halo} given m_{stellar}.[2] From here on, we will refer to the halo mass calculated in this manner as the "infall mass." The mass of any given group is then the total mass of all of its constituent galaxies' haloes:

$$M_{\text{tot}} = \Sigma m_{\text{halo}}. \tag{2.4}$$

Note that the formula from Guo et al. (2010) was determined based on observational data rather than data from the Millennium Simulation. As can be seen in Fig. 2.1, the stellar mass distribution in the simulated catalogues used here is cut off more sharply at high stellar mass than the data from the CFHTLenS. Since high stellar mass galaxies are typically at the centres of groups, the result is that the group-central galaxies in the simulated catalogues have less stellar mass than galaxies in similar-mass groups in the CFHTLenS. As such, when we estimate halo mass from stellar mass in this method, we typically underestimate group mass.

2.2.2.2 Stripping Models

Using the data for total group mass and satellite infall mass, we constructed the following two models for the mass distributions of satellite and group haloes:

- No Stripping: A model expected to correspond to unrelaxed groups. Satellites retain their infall masses. The mass of the central halo is then set equal to M_{tot} minus the mass in satellite haloes.

---

[2]There is a log-normal scatter in this relation of ~ 0.17 dex (Yang et al., 2012), which we do not simulate. Testing showed that the effect of this scatter on our results was negligible.
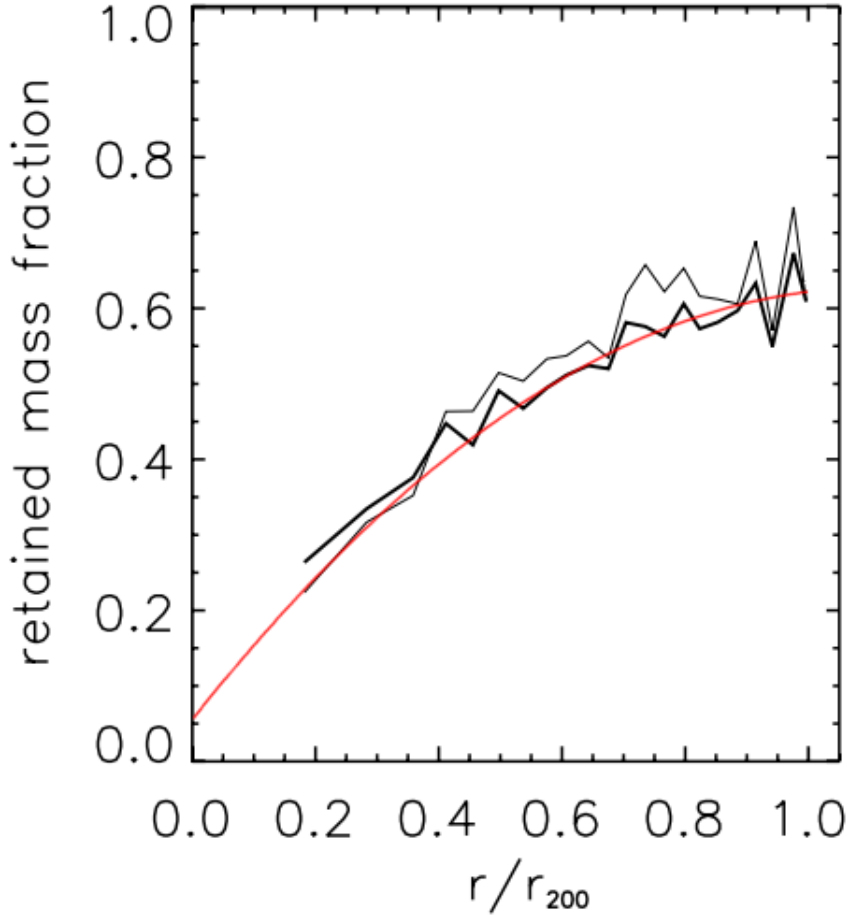
FIGURE 2.2: Fig. 15, upper-right panel of Gao et al. (2004), showing the mean (thick black) and median (thin black) retained mass fractions for subhaloes within cluster haloes. Our fit to it, Equation (2.5), is overlaid (red curve). The fit has mean residual 2.5×10^{-4} and root-mean-square residual 1.8×10^{-2}.

- Stripping: A model expected to correspond to relaxed groups, on average. Masses of satellite haloes are decreased relative to their infall mass by an amount dependent on their projected distance from the group centre. The central halo's mass is then set equal to M_{tot} minus the mass that remains in satellite haloes.

We also compare with a "Matched Field" dataset, which is matched in redshift and stellar mass to the satellite galaxies used in the above two models. This dataset allows us to measure what the lensing signal around the galaxies in the No Stripping model would look like if the contribution from being in a group environment were removed.

In order to model stripping within groups, we applied results from Fig. 15 of Gao et al. (2004) to estimate a satellite's retained mass fraction from the projected distance

between it and its group's centre, using the following function, fit by hand to the figure:

$$\frac{M_{\text{ret}}}{M_{\text{init}}} \approx -0.464 \left(\frac{r}{r_{200}}\right)^2 + 1.03 \left(\frac{r}{r_{200}}\right) + 0.058. \tag{2.5}$$

A comparison of this fit to the plot by Gao et al. (2004) can be seen in Fig. 2.2. With this prescription, we find that the mean retained mass after stripping is approximately 40% of the initial mass.

We modeled the reduction of satellite mass due to stripping by decreasing their tidal radii. The relationship between mass within the virial radius and tidal radius is given by:

$$M_{\text{halo}} = M_0 \frac{\tau^2}{(\tau^2 + 1)^2} \left[(\tau^2 - 1) \ln(\tau) + \tau\pi - (\tau^2 + 1) \right] \tag{2.6}$$

(Baltz et al., 2009). As this equation is not analytically invertible, we use a solution-space search to find the value of τ which gives the proper value for $\frac{M_{\text{ret}}}{M_{\text{init}}}$.

As has been shown by Gao et al. (2004), the fraction of group mass contained within satellites at a given radius increases with distance from the group centre. This implies that in the Stripping and No Stripping models, we should use a halo density profile for the central halo which converges to the original profile near the core, but is progressively lower than the original profile as the radius increases. We accomplish this with the following, modified version of the truncated NFW profile, which we call the "contracted" NFW profile:

$$\rho(x) = \frac{M_0' f_r}{4\pi r_s'^3} \frac{1}{x'(1 + x')^2} \frac{\tau'^2}{\tau'^2 + x'^2}, \tag{2.7}$$

where f_r is the fraction of mass retained by the group halo, and M_0', r_s', x', and τ' are calculated with new concentration $c' > c$, which satisfies the equation:

$$\frac{c^2}{\ln(1 + c) - c/(1 + c)} = \frac{f_r c'^2}{\ln(1 + c') - c'/(1 + c')}. \tag{2.8}$$

This ensures that in the region near the core, where $x \ll 1$, this profile will converge with the profile given by Equation (2.1). Since this profile has a higher concentration than the original profile, the density will decrease faster with radius than in the original profile. There is no strong physical evidence for this specific model; it is used simply because it meets the basic requirements of converging to the initial NFW profile near the core while having a greater fraction of mass in satellites far from the core, and because its lensing signal can be calculated analytically in the same manner as the lensing signal of an NFW profile.
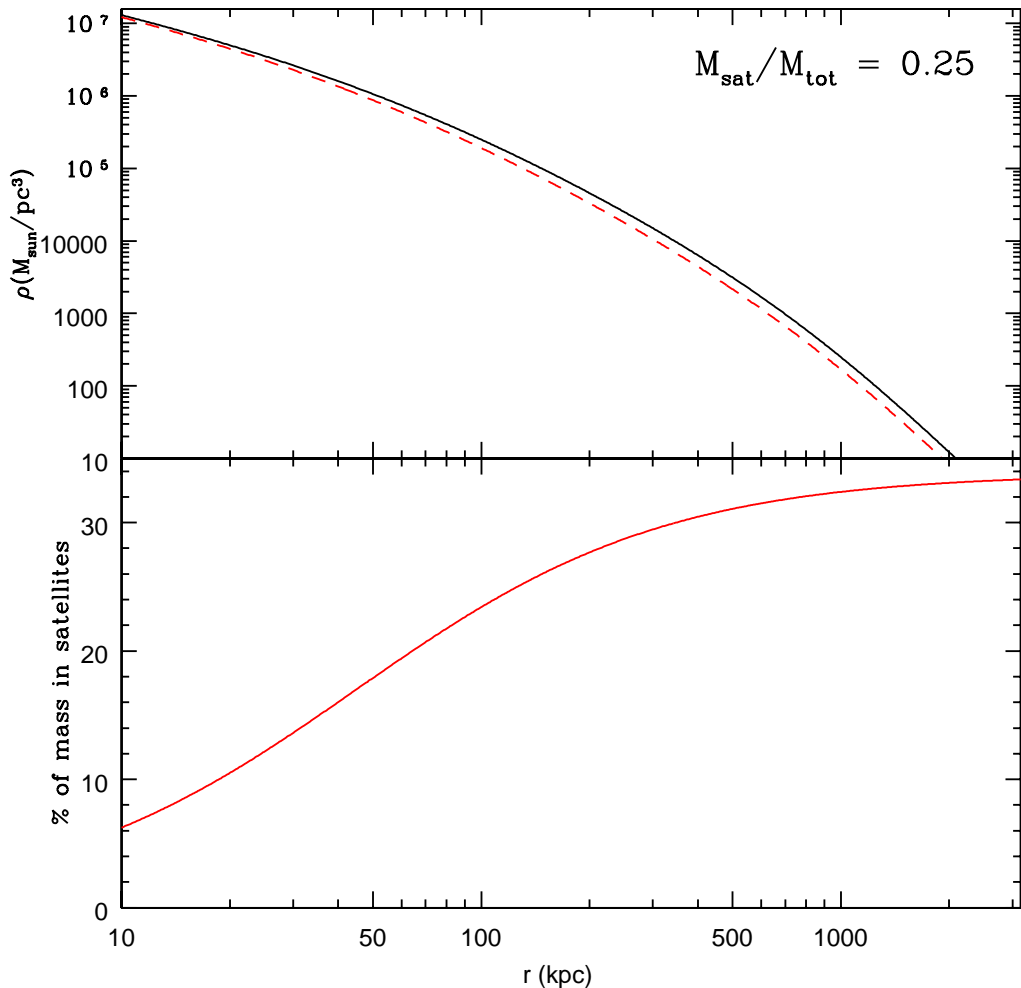
FIGURE 2.3: Top panel: An illustration of our "contracted NFW" profile (red dashed) compared to the initial profile (black solid), with a group of $M_{\text{tot}} = 10^{13}$ $M_\odot$ and $M_{\text{sat}}/M_{\text{tot}} = 0.25$. The profile converges with the initial NFW profile near the core, but falls below it away from the core. Bottom panel: The resultant fraction of mass assumed to be in satellites at a distance r from the center of this profile. This curve meets our requirements of decreasing to zero at the core and rising with radius.

An illustration of this transformation, along with a plot of the mass fraction assumed to be contained within satellites under this model, can be seen in Fig. 2.3. The weak lensing signal for this model can be calculated similarly to the original model, simply by using a different concentration and applying f_r as a scaling factor. For consistency, we use this profile for all haloes, with $f_r = 1$ for all satellite and field haloes.

2.2.3 Determining Ellipticity

While full ray-tracing, such as that performed by Hilbert et al. (2009), is a powerful tool for estimating weak lensing signals caused by an arbitrary mass distribution, it has

a few limitations. The accuracy of the ray-tracing is limited by the resolution of the simulations used to generate the lens mass distribution, which causes the algorithm to noticeably underestimate the lensing signal within 50 kpc of halo cores (this effect can be seen in Fig. 3.3 below). Additionally, the algorithm has no method to easily model different hypothetical mass distributions, as we wish to test here. Because of this, we have developed a modified ray-tracing algorithm in which we assume that all dark matter lies in spherical haloes in amounts and distributions dependent on the models described in Section 2.2.2.2. The algorithm is as follows:

1. Lens galaxies are assigned mass, concentration, tidal radius, and scaling factor under one of the models described in Section 2.2.2.2.

2. In order to eliminate edge effects, the catalogue of lens galaxies used for this algorithm includes galaxies within a wider field of view than the catalogue of source galaxies. Since the fields are 4×4 degrees, we accomplish this by only using source galaxies within a central 1.4 x 1.4 degree square field, which also significantly reduces the amount of computational time needed for later analysis. For the rest of our analysis, we also only use lens galaxies that lie within this central field.

3. Each source galaxy is initialized with zero ellipticity in both components (shape noise is simulated at a later stage of analysis).

4. For each source galaxy, tangential shear is applied to it for every lens galaxy where $([\mathrm{RA_{lens}} - \mathrm{RA_{source}}] \times \cos(\mathrm{Dec_{lens}}))^2 + (\mathrm{Dec_{lens}} - \mathrm{Dec_{source}})^2 < (\Delta_{\max})^2$ and $z_{\mathrm{lens}} < z_{\mathrm{source}}$. Here $\Delta_{\max}$ is an upper limit to conserve computational time and ensure that the rectangular boundaries of the field will not cause artefacts in the lensing signal. The strength of the shear applied is determined using the equations of Baltz et al. (2009) for a truncated NFW halo and our modifications for a contracted NFW profile (see Section 2.2.2.2).[3]

5. Shear is added linearly to the ellipticity of the source galaxy for all lens galaxies within this lightcone.

This process in principle accounts for the two-halo term seen in the lensing signal around groups, which is caused by other nearby groups. However, our application of a cut-off angle $\Delta_{\max}$ suppresses lensing signals at large radii, meaning the two-halo term is not observable in our simulated lensing signals. This method does not account for dark matter that is correlated with the positions of galaxies and groups but not considered

---

[3]We use an approximation for angular separation here to conserve computational time. With the small separations involved ($\ll 1\,\mathrm{deg}$), this approximation is nearly exact.

part of their haloes, which also results in a slight suppression of the lensing signal at large ($R \gtrsim 1000$ kpc) scales. Since we are interested in the stripping of subhaloes, for which the relative signal is strongest at intermediate (50 kpc $\lesssim R \lesssim 400$ kpc) scales, this suppression at large scales will have no effect on our analysis.

2.3 Catalogue Analysis

In Section 2.3.1, we discuss the method we use to estimate the environments of galaxies. In Section 2.3.2, we describe how the galaxy sample is divided into matched high-density and low-density subsamples, and we present the statistics of the galaxies in the HDE and LDE samples.

2.3.1 Determining Environment: The P3 Algorithm

It is not a trivial matter to determine which galaxies are members of groups. Even when spectroscopic redshifts are available, the peculiar velocities of galaxies make it impossible to determine the memberships of groups with absolute certainty (Robotham et al., 2011). When only photometric redshifts are available, the best we can do is to select galaxies that are likely to be members of groups. To do so, we use a modified version of the Photo-z Probability Peaks (P3) algorithm (Gillis and Hudson, 2011). The P3 algorithm generates a 3-D density field by smoothing the distribution of galaxies in the redshift direction according to the probability distribution function of their photometric redshifts. The algorithm identifies peaks in the pseudo-three-dimensional field with group centres. Here we do not use the group centres, but rather use the entire P3 density field to identify overdense regions. Rather than use the local P3 overdensity itself, we restrict ourselves to regions in which we have high confidence in the overdensity, and instead use the signal-to-noise (S/N) of the local overdensity, under the assumption that galaxies in overdense regions of space are more likely to be in groups than galaxies in underdense regions.

We now briefly review the technical details of the P3 algorithm. To determine the S/N of a given test galaxy, the P3 algorithm compares the density of galaxies within a circular aperture ($R = 0.5$ Mpc) surrounding each test galaxy to the density of galaxies within a larger annulus ($R_{\text{inner}} = 1$ Mpc, $R_{\text{outer}} = 3$ Mpc) surrounding each test galaxy (to approximate the background density). The contribution of each galaxy to this measurement is weighted by the probability that this galaxy lies at the same redshift as the test galaxy (by taking the integral of the photo-z probability distribution function over

a thin redshift slice). This gives the overdensity:

$$\delta = \frac{\rho_{\mathrm{ap}} - \rho_{\mathrm{annu}}}{\rho_{\mathrm{annu}}}, \tag{2.9}$$

where ρ_{ap} and ρ_{annu} are the weighted densities of galaxies within the aperture and annulus surrounding the test galaxy, respectively. This value can take the range $-1 < \delta < \infty$, where negative values correspond to regions less dense than the background density, and positive values correspond to overdense regions. We then estimate the noise in this value by assuming a Poisson distribution for galaxies:

$$\sigma_{\mathrm{Poisson}} = \sqrt{\left(\frac{\rho_{\mathrm{ap}}}{n_{\mathrm{ap}}}\right)^2 + \left(\frac{\rho_{\mathrm{annu}}}{n_{\mathrm{annu}}}\right)^2}, \tag{2.10}$$

where n_{ap} and n_{annu} are the numbers of galaxies in the aperture and annulus respectively with more than a threshold weight.[4] From this, we calculate the S/N $\equiv \delta/\sigma_{\mathrm{Poisson}}$ for each test galaxy. Note that this S/N can take negative values when δ is negative. The distribution of the S/N values that results from this calculation depends on the choice of threshold weight used, so our choices of S/N limits are not universally applicable. We picked limits of S/N > 2 for the high-density sample and S/N < 0 for the low-density sample based on an analysis of the simulated galaxy catalogues to maximize the expected signal for tidal stripping.[5]

Since this environment estimator provides us with galaxy samples biased to lie in high- and low-density environments, we cannot use the standard halo model (eg. Mandelbaum et al., 2006b, Velander et al., 2013) for fitting our lensing signals. Instead, the models we use are calibrated from simulations and are detailed in Section 2.2.2.

2.3.2 Galaxy Matching

2.3.2.1 Matching Algorithm

We use the S/N values obtained for each of the galaxies in Section 2.3.1 to form two samples of galaxies from the catalogues. As we cannot ensure that a pair of random samples of galaxies in high- and low-density environments will have the same distribution

---

[4]We use a threshold weight here of a $> 0.001\%$ chance of lying within a redshift of 0.01 of the test galaxy.

[5]In a rough approximation, the expected signal-to-noise of a stripping measurement is proportional to $(f_{\mathrm{sat,HDE}} - f_{\mathrm{sat,LDE}})\sqrt{N_{\mathrm{HDE}}^{-1} + N_{\mathrm{LDE}}^{-1}}$, where $f_{\mathrm{sat,HDE}}$ and $f_{\mathrm{sat,LDE}}$ are the fractions of satellites in the HDE and LDE samples respectively, and N_{HDE} and N_{LDE} are the number counts of galaxies in the HDE and LDE samples respectively. We calculated this value for various S/N cuts, and the combination of S/N > 2 for the HDE sample and S/N < 0 for the LDE sample provided the best expected signal-to-noise for a stripping measurement.

of stellar mass and redshift as each other, and both of these will affect the measured lensing signal, we perform a matching between galaxies with S/N > 2 and galaxies with S/N < 0 as follows:

1. For each galaxy with S/N > 2, we search through all galaxies with S/N < 0 within the same pointing.[6]

2. For each S/N < 0 galaxy, if its stellar mass differs from the stellar mass of the S/N > 0 galaxy by more than 20%, we exclude it as a possible match.

3. For each remaining S/N < 0 galaxy, we calculate a quality-of-match value:

$$d = \sqrt{\left(\frac{z_{\mathrm{H}} - z_{\mathrm{L}}}{z_{\mathrm{H}}}\right)^2 + (10(\log m_{\mathrm{H}} - \log m_{\mathrm{L}}))^2} \tag{2.11}$$

where z_{H} and z_{L} are the redshifts of the S/N > 2 and S/N < 0 galaxies, respectively, and m_{H} and m_{L} are their stellar masses. This form significantly prioritizes a match in mass over redshift, as the lensing signal depends much more strongly on mass than redshift.

4. We select the four S/N < 0 galaxies with the lowest d values as matches for this S/N > 2 galaxy. If there are fewer than four match candidates, we assign them all as matches.

5. Assuming at least one match was found for it, we add this S/N > 2 galaxy to the HDE sample, and we set its weight equal the number of matches we found. (This weight is later applied when we stack lensing signals together, and this modification is necessary to ensure the mass distributions of the HDE and LDE samples are comparable.)

6. We assign all match galaxies to the LDE sample. If they were not already in the LDE sample, we set each of their weights to 1. Otherwise, we increase their weights by 1.

The resultant mass and redshift distributions of this scheme are assessed in Section 2.3.2.2.

2.3.2.2 Statistics of Galaxy Selection

Fig. 2.4 shows the distributions of stellar mass and redshift for the HDE and LDE samples of lens galaxies in the CFHTLenS. The matching scheme results in a nearly identical distribution of stellar masses for HDE and LDE galaxies, and a very similar distribution of redshifts.
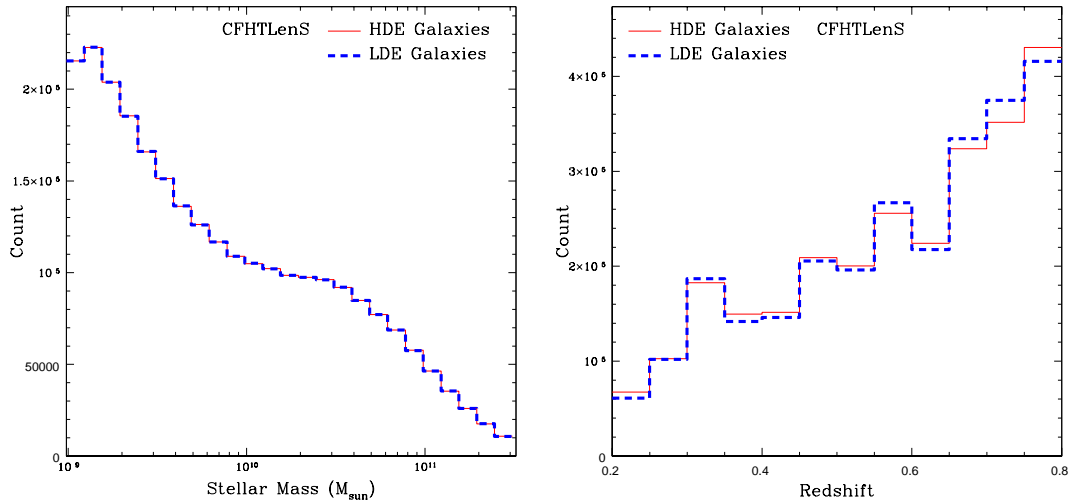
FIGURE 2.4: The distributions of stellar mass (left) and redshift (right) for the samples of HDE (solid line) and LDE (dashed line) galaxies in the CFHTLenS catalogues, which, because of our matching algorithm, are virtually identical. The redshift distributions differ slightly between HDE and LDE galaxies, but there is no apparent trend to the deviation.

CFHTLenS					
		HDE		LDE	
$\log m$	$\overline{z}$	f_{red}	f_{blue}	f_{red}	f_{blue}
9–9.5	0.57	0.13	0.73	0.08	0.80
9.5–10	0.56	0.28	0.60	0.18	0.70
10–10.5	0.56	0.54	0.30	0.44	0.38
10.5–11	0.57	0.78	0.10	0.72	0.13
11–11.5	0.57	0.95	0.02	0.90	0.03
9–10.5	0.56	0.43	0.43	0.33	0.51

TABLE 2.2: Statistics of galaxies in various stellar mass bins in the CFHTLenS, as a function of environment. $\overline{z}$ is the mean redshift of the bin. f_{red} is the fraction of galaxies that are red, and f_{blue} is the fraction that are blue, determined by the best-fit photometric templates and defined in the same manner as by Velander et al. (2013). Fractions do not add to unity as not all galaxies are classified as "red" or "blue." See Velander et al. (2013) for further explanation. All average values and fractions assume galaxies are weighted by their stellar masses.

Table 2.2 shows statistics for lens galaxies in the HDE and LDE samples in the CFHTLenS, for various stellar mass bins. The HDE sample contains a higher fraction of red galaxies than the LDE sample, as expected, but the difference is at most 10% for a given stellar mass bin. This difference in the fractions of red and blue galaxies could in principle lead to a spurious detection of stripping if there is a relative bias in the stellar mass estimates between red and blue galaxies. This issue is discussed further in Section 2.6.4.1, where we conclude that this is unlikely to pose a problem for our analysis.

---

[6]Matching only within the same pointing is done to conserve computational time.
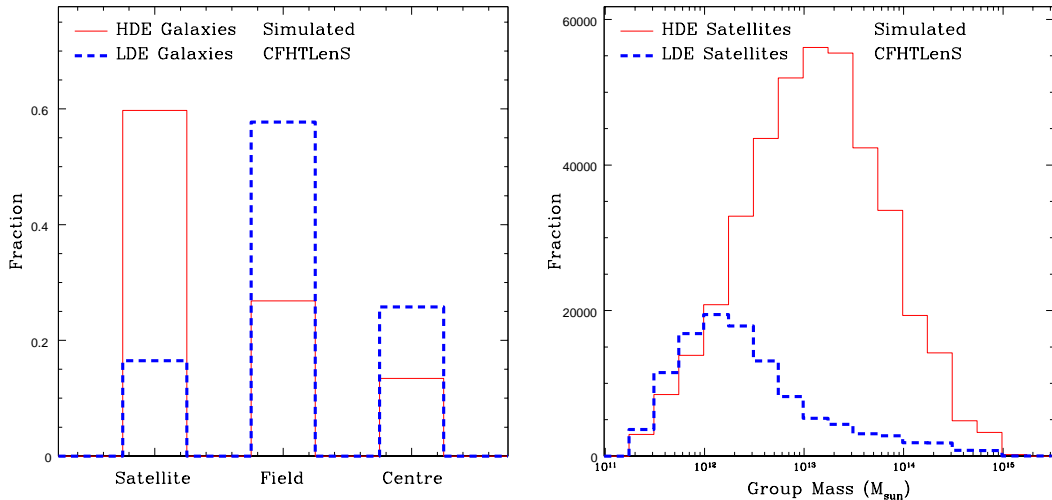
FIGURE 2.5: The distributions of the types of galaxies classified as HDE and LDE in the simulations (left), and, of those classified as satellites, the distributions of the masses of the groups in which they reside (right). Plots assume detection limits and photo-z quality similar to the CFHTLenS.

Simulated CFHTLenS										
			HDE				LDE			
$\log m$	$\overline{M}$	$\overline{z}$	f_{sat}	f_{field}	f_{cen}	$\overline{M}_{\text{host}}$	f_{sat}	f_{field}	f_{cen}	$\overline{M}_{\text{host}}$
9–9.5	17	0.37	0.54	0.42	0.05	4700	0.14	0.79	0.07	1600
9.5–10	32	0.45	0.62	0.25	0.13	4000	0.15	0.61	0.24	1500
10–10.5	80	0.51	0.64	0.10	0.26	4300	0.13	0.32	0.54	1900
10.5–11	390	0.50	0.45	0.02	0.53	5600	0.09	0.12	0.79	3400
9–10.5	63	0.48	0.63	0.16	0.21	4300	0.14	0.43	0.43	1800

TABLE 2.3: Statistics of galaxies in the Millennium simulation for various stellar mass bins, using our models for estimating halo mass and environment, and assuming similar detection limits and photo-z quality to the CFHTLenS. $\log m$ is the stellar mass bin. $\overline{M}$ is the mean halo mass of the galaxies in this bin in units of $10^{10} M_{\odot}$, and $\overline{z}$ is their mean redshift. f_{sat}, f_{field}, and f_{cen} are the fractions of galaxies that are satellites, field galaxies, and group centrals, respectively. $\overline{M}_{\text{host}}$ is the mean mass of the host group for satellite galaxies in units of $10^{10} M_{\odot}$. All values assume galaxies are weighted by their stellar masses.

Fig. 2.5 shows the distributions of galaxy types for the mock HDE and LDE samples drawn from the Millennium Simulation, and, for the satellite galaxies within each sample, the distribution of the masses of the groups in which they reside. We classify galaxies as "central" (the most massive galaxy in a group), "satellite" (in a group but not the most massive galaxy) or "field" galaxy (not in a group). Table 2.3 shows the distributions of galaxy types for the HDE and LDE samples for various stellar mass bins. This shows that the fraction of satellites in the HDE sample remains roughly constant with stellar mass and decreases slightly with stellar mass in the LDE sample. For all samples, the fraction of centrals rises with stellar mass, while the fraction of field galaxies falls. No sample

shows any significant change with stellar mass in the mean mass of the host groups for satellites, except for a rise in the most massive stellar mass bin tested. HDE satellites are observed to reside in groups of $\sim 4 \times 10^{13}$ $M_\odot$. In contrast, for the small fraction of LDE galaxies that are satellites, the characteristic host halo mass is $\sim 1.8 \times 10^{13}$ $M_\odot$.

We note that the redshift distributions of galaxies in our simulated catalogues does not well-match the redshift distributions of galaxies in our CFHTLenS catalogues. Galaxies in the simulated catalogues typically reside at lower redshift ($\overline{z} \sim 0.45$) compared to the galaxies in the CFHTLenS catalogues ($\overline{z} \sim 0.55$). However, as we match our HDE and LDE samples on redshift in addition to stellar mass, and our results rely on a differential comparison, this difference from simulations should have negligible effects on our results. At most, this might affect the fraction of galaxies within our HDE sample which are satellites; we investigate the effects that a different value of this parameter might have on our results in Section 2.6.4.2.

2.3.2.3 Measuring the Lensing Signal

To calculate the lensing signal around the HDE and LDE lens galaxies, we stack together all galaxies in a particular sample and stellar mass bin[7]. We then bin all lens-source pairs (only using pairs where $z_{\mathrm{phot,source}} > z_{\mathrm{phot,lens}}+0.1$) based on the projected distance between the lens and source, calculated at the redshift of the lens. For each pair, we calculate the tangential ellipticity of the source relative to the lens, g_t, and convert this into units of surface mass density gradient $\Delta\Sigma$ using the equations in Section 1.3.1. We compute the error in this value empirically from the root-mean-squared scatter in calculated $\Delta\Sigma$ values for all lens-source pairs in each annular bin.

For the error calculations in our model fits, we assume the noise in all radial annuli is independent. Strictly speaking, this is not true, as there is a small correlation between the ellipticities of nearby sources due to the effects of cosmic shear, but this effect is negligible except at extremely large radial annuli. For computational simplicity, we do not apply the $c2$ correction to our CFHTLenS samples[8] to source ellipticities in our analysis. Because galaxy-galaxy measurements stack lens-source pairs over all position angles, they are insensitive to this correction(see Velander et al., 2013, for further explanation and justification of this). Moreover, here we are interested in a differential measurement between galaxy-galaxy lensing samples, and so we expect our results to be highly robust to this effect.

---

[7]This process is performed one pointing at a time due to computational limitations, and all pointings are stacked together in the end.

[8]The $c2$ correction is an empirical correction to the $e2$ component of source ellipticity, based on the assumption that the mean $e2$ across a given field should be close to zero.

2.4 Halo Model

We expect the lensing signal around galaxies in the HDE sample to be reasonably well-described by the following halo model (see, e.g., Velander et al., 2013):

$$\Delta\Sigma = \Delta\Sigma_{1h} + f_{sat}\Delta\Sigma_{OG} + \Delta\Sigma_{2h} \tag{2.12}$$

where $\Delta\Sigma_{1h}$ is the "one-halo" term, f_{sat} is the fraction of galaxies in the sample that are satellites $\Delta\Sigma_{OG}$ is the "offset group halo" term, and $\Delta\Sigma_{2h}$ is the "two-halo" term, as described below:

- One-halo term: The lensing signal that results from the galaxy's own dark matter halo.

- Offset group halo term: This is the contribution to the lensing signal around a satellite caused by the presence of its group's halo.

- Two-halo term: Galaxies will typically reside near other massive structures, which results in a contribution to the lensing signal at large radii.

Since galaxies in the HDE sample are more likely lie to in overdense regions, we cannot apply exactly the same halo model as, e.g., Velander et al. (2013), who use all galaxies independent of environment. This primarily affects the offset group halo term. See Section 2.4.2 below for an explanation of how we modify our halo model to account for this.

For LDE galaxies, we expect the signal to be described by the form:

$$\Delta\Sigma = \Delta\Sigma_{1h} + \Delta\Sigma_{UD} \tag{2.13}$$

where $\Delta\Sigma_{UD}$ is the "underdensity" term, which is the effective contribution from the fact that galaxies in an underdense environment will see a negative contribution to their lensing signal at large radii. This effect is analogous to the offset group halo term, except arising from an underdensity instead of an overdensity, and is explained in more detail in Section 2.4.3.

We can best compare the lensing signals that result from stacks of HDE and LDE galaxies by fitting the signals with a model profile, and comparing these fits. The model profile for the HDE sample includes just the "one-halo" and "offset group halo" terms. Since the "underdensity" and "two-halo" terms are only significant at relatively large

radii, we can safely ignore them if we do not fit the profiles out to large radii. We discuss this further in Section 2.6.4.2.

These components are discussed in the sections below, and we discuss the procedure we use to fit a model to the data in Section 2.5.

2.4.1 One-halo term

For the one-halo term, we assume that all galaxies reside in a dark matter halo that can be approximated by a truncated NFW density profile, as formulated by Baltz et al. (2009). This model has three free parameters: the halo mass M_{200}, concentration c, and the truncation parameter $\tau \equiv r_{\mathrm{trunc}}/r_{\mathrm{s}}$. In practice, we have found that the signal is not strong enough to simultaneously constrain all three parameters. Therefore, for simplicity, in our default fits discussed below, we fit only M_{200}, with c fixed by Equation (2.2), taken from Neto et al. (2007), and we also fix $\tau = 2c$, which is a reasonable value for unstripped haloes (Hilbert and White, 2010, Oguri and Hamana, 2011).

In Section 2.6.3.2, we investigate alternative fits in which c or τ are left free and fitted to the data.

2.4.2 Offset group halo term

Since the P3 algorithm biases our galaxy selection such that the HDE sample predominantly consists of galaxies within groups, we cannot use the standard halo model (e.g., Velander et al., 2013) to calculate the contributions of nearby groups. Instead, we make the assumption that the sample consists of a fraction f_{sat} satellites, and the rest are either central or field galaxies. The central and field galaxies will only have a one-halo component in their lensing signals, while satellites will have both the one-halo component and a contribution from their host groups. In order to model the average contribution of group haloes to the lensing signal around galaxies in the HDE sample, we assume that it takes the following form:

$$\Delta\Sigma_{\mathrm{OG}}(R) = \int_0^\infty \Delta\Sigma_{\mathrm{host}}(R, R_s) \mathrm{P}(R_s) dR_s, \tag{2.14}$$

where R_S is the projected separation between a satellite and the group centre, $\Delta\Sigma_{\mathrm{host}}(R, R_s)$ is the contribution of the group halo to the lensing signal around a point at projected distance R from the group centre:

$$\Delta\Sigma_{\text{host}}(R, R_s) = \overline{\Sigma_{\text{host}}(< R, R_s)} - \overline{\Sigma_{\text{host}}(R, R_s)}$$
$$= \frac{1}{\pi R^2} \int_0^R 2\pi R' \int_0^{2\pi} \Sigma_{\text{host}}(R_g) d\theta dR'$$
$$- \frac{1}{2\pi} \int_0^{2\pi} \Sigma_{\text{host}}(R_g) d\theta, \qquad (2.15)$$

where $\Sigma_{\text{host}}(R_g)$ is the projected surface density of the host group's halo at projected radius $R_g = \sqrt{R'^2 + R_s^2 - R'R_s\cos\theta}$ and $P(R_s)$ is the probability that a satellite in the sample will reside a distance R_s from the centre of its host group. We assume $P(R_s)$ takes the form:

$$P(R_s) = \frac{1}{M_N} 2\pi R_s \Sigma(R_s, M_{\text{gr}}, c_{\text{sat}}) P_{\text{HDE}}(R_s), \qquad (2.16)$$

where M_N is a normalization factor, $\Sigma(R_s, M_{\text{gr}}, c_{\text{sat}})$ is the projected surface density of an NFW halo with mass equal to the mass of the host group, M_{gr}, but a concentration c_{sat}, different from the dark matter concentration c. Analyses of the satellite density in groups and clusters (Lin et al., 2004, Budzynski et al., 2012) have indicated that the spatial distribution of satellites can be well-modelled in this way, assuming an NFW density profile with concentration ~ 2.5, which is lower than the typical concentration of the dark matter halo by a factor of ~ 2.

The term $P_{\text{HDE}}(R_s)$ is the probability that a satellite at a distance R_s from the centre of the host group will be included in the HDE sample. The form of $P_{\text{HDE}}(R_s)$ is determined by the selection effects inherent in the P3 algorithm. To first order, P3 selects galaxies in regions of high projected surface density for the HDE sample. We thus model $P_{\text{HDE}}(R_s)$ as a smooth cut-off based on the projected surface density of the group. We wish for it to converge to $P_{\text{HDE}}(R_s) = 1$ for $\Sigma(R_s) \gg \Sigma_t$, and converge to $P_{\text{HDE}}(R_s) = 0$ for $\Sigma(R_s) \ll \Sigma_t$. We therefore choose the following functional form, which has these properties:

$$P_{\text{HDE}}(R_s) = \frac{\Sigma(R_s)^2}{\Sigma(R_s)^2 + \Sigma_t^2}, \qquad (2.17)$$

where $\Sigma(R_s)$ is the projected surface density for a satellite at distance R_s from a group centre and Σ_t is the threshold density. As we have no prior justification for any specific density threshold to use, we leave this parameter free, to be fit by our algorithm.

For the HDE sample, we fix f_{sat} to the value found in the mock HDE sample from the Millennium Simulation. We do not expect this simulated result to perfectly match the fraction of satellites we might find in the CFHTLenS dataset, and we investigate

the impact that a different value of f_{sat} might have in Section 2.6.4.2. For the LDE sample, we do not include this term, since the form of the measured lensing signal in both simulated and CFHTLenS data shows that the underdensity signal dominates at large radii (see the simulated LDE signal in Fig. 2.7 and the measured LDE signal in Fig. 2.8).

We choose to model the offset group halo term as if all groups are of the same mass. We tested this assumption using a distribution of group masses, and the resulting signal was not appreciably different from the single-mass signal. The use of a distribution of group masses did tend to increase the resultant signal (the difference scaling with the spread of the mass distribution), even when the mean mass is fixed, and so the single-mass model will likely underestimate the mean host halo mass.

Fig. 2.6 illustrates how the modeled one-halo term varies with satellite halo mass, as well as how the fitted offset group halo terms varies with the group halo mass M_{group}, satellite concentration c_{sat} and threshold surface density Σ_{t}.

2.4.3   Underdensity signal

Galaxies in the LDE sample are selected to lie in S/N < 0 regions, which are underdense ($\delta < 0$) compared to a surrounding annulus with inner radius 1 Mpc and outer radius 3 Mpc. Similar to the way in which galaxies in groups have a positive contribution to their lensing signal from the offset overdensity in which they reside, galaxies in underdense regions will have a negative contribution to their lensing signal on larger scales due to the fact that their local environment is less dense than the surrounding environment. This effect has been observed in both the CFHTLenS dataset, as well as in the simulations.

The expected form of this negative lensing signal has not been well-studied, so there is no functional form which we expect it to take. We have attempted to fit this signal with the same functional form as the group halo term, multiplied by a negative free term, but this failed to provide a suitable fit to either the simulated or to the CFHTLenS data. Note in the right panel of Fig. 2.8 below that the minimum value for the LDE signal is at a higher projected radius than the peak of the offset group halo term.

To handle this effect for the LDE sample, we only fit the lensing signal for $R < 400$ kpc, where the one-halo term dominates the signal.
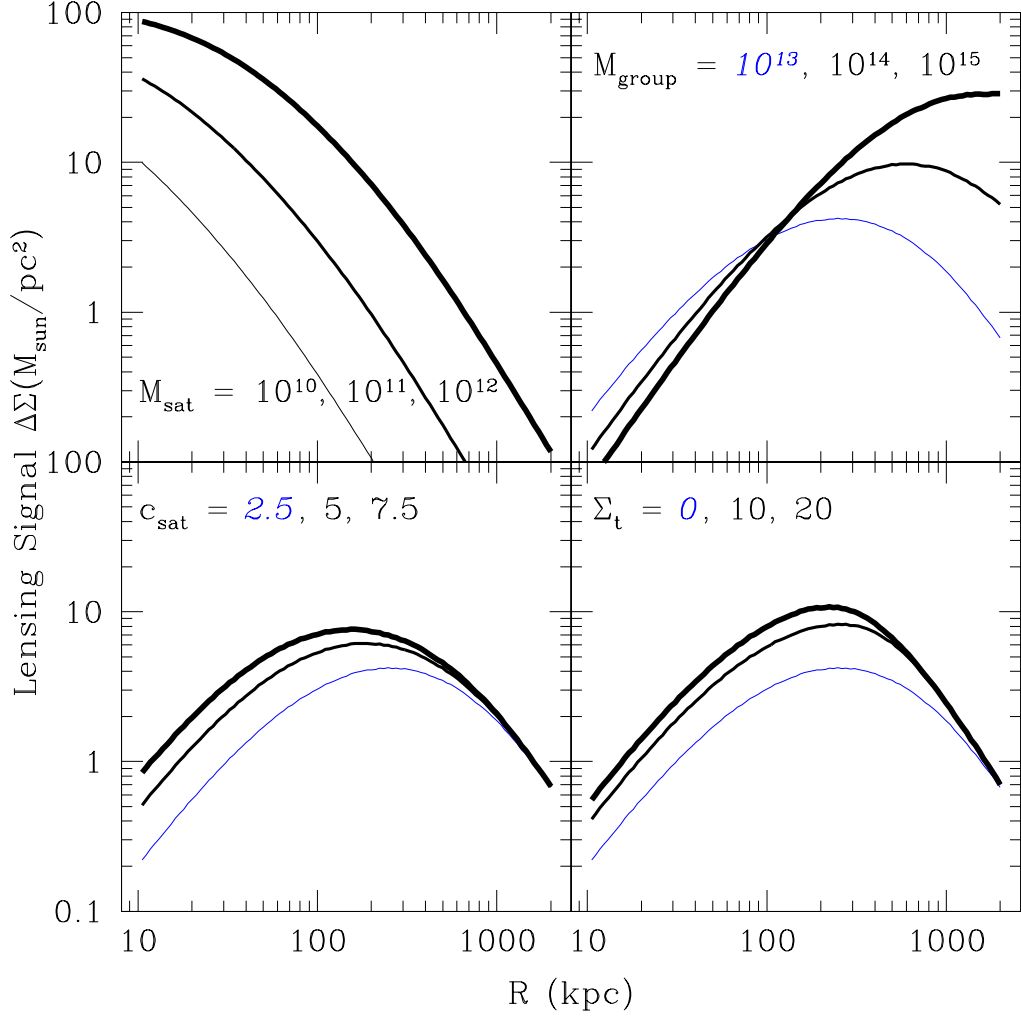
FIGURE 2.6: An illustration of how the one-halo term varies with satellite mass (top left); and how the offset group halo term (Equation (2.15)) varies with group mass (top right), satellite concentration (bottom left), and density threshold (bottom right). Plotted values of the parameters, with italicized parameter corresponding to the value used for other plots: $M_{\rm sat} = 10^{10}$, 10^{11}, 10^{12} $M_\odot$; $M_{\rm group} = 10^{13}$, 10^{14}, 10^{15} $M_\odot$; $c_{\rm sat} = 2.5$, 5, 7.5, $\Sigma_t = 0$, 10, 20 $M_\odot/\,{\rm pc}^2$. Increasing line weight corresponds to increasing the varying parameter. The fraction of satellites which reside in groups is not illustrated, as it is a simple scaling of the group halo term; it is fixed to 0.6 for these plots.

2.5 Fitting Procedure

For all fits, we use radial bins of 25 kpc$< R < 2000$ kpc. We tested constraining the fits to a lower maximum radius, and this had no noticeable effect on the fitted satellite halo masses. Fitting to a lower maximum radius only altered the fitted group mass, making it less well-constrained.

We use a two-step procedure to fit the models to the lensing signals. Because our models are relatively simple, they are not perfect fits to the data. So, we first attempt to determine the amount of error inherent in our modelling in order to assign more conservative uncertainties to the fitted parameters. To do this, we first perform a steepest-descent χ^2 minimization to obtain best-fitting parameters for the model. At this point, if the χ^2_{red} value for the fit is greater than 1, we assume that this is due to some error in the modeling, which we parametrize as σ_{m}. We uniformly add this value in quadrature to the measured uncertainties in all radial bins, such that the adjusted $\chi^2_{\mathrm{red}} = 1$ for the best fit. We then repeat this process, finding new best-fit values and recalculating σ_{m} until convergence is reached.

Since this procedure effectively increases the error in all radial bins, this process has the result of increasing the measured errors on all fitted parameters. If the model is initially a good fit ($\chi^2_{\mathrm{red}} \approx 1$) to the data, the increase is negligible, but if the model is a poor fit to the data, the estimated errors for the fitted parameters will be significantly increased. As such, this process allows us to place more conservative limits on our results, based on the quality of the fit of the model to the data.

Additionally, since the model error is uniformly added to the errors in all radial bins, it prevents the fitting algorithm from over-weighting the fit to the high-radius bins, which otherwise have significantly lower errors, and thus typically contribute more to the χ^2 value of the fit if the model is not a perfect fit to the data.

For the models we tested, we typically found for the HDE samples that $\sigma_{\mathrm{m}} \lesssim 0.5 M_\odot/\mathrm{pc}^2$, which is $\lesssim 5\%$ of the measured lensing signal, $\Delta\Sigma$. For the LDE samples, most fits were initially of $\chi^2_{\mathrm{red}} \approx 1$, and so no model error term was necessary.

Once the model error is determined, we run an MCMC algorithm to help determine the errors of the fitted parameters. Since only the mass of satellite haloes is relevant to us, we marginalize over all other parameters to obtain the mean value and errors for the satellite mass.

TABLE 2.4: Results of the fitting procedure when applied to simulated (top) and the CFHTLenS (bottom) lensing data in various stellar mass bins. All masses are in units of 10^{10} $M_\odot$. $\log m$ is the stellar mass bin. f_{sat} is the fraction of satellites we use for the fitting, based on data from the Millennium Simulation. M_{HDE} and M_{LDE} are the fitted one-halo masses for the HDE and LDE samples. M_{gr} is the fitted mass of the offset group halo term. R_M is the ratio of M_{HDE} to M_{LDE}. χ^2_{red} is the reduced χ^2 parameter without the model error term (see Section 2.5) included (for 36 degrees of freedom; a value close to 1 is ideal).

		"No Stripping" Model				"Stripping" Model			
$\log m$	f_{sat}	M_{HDE}	M_{gr}	M_{LDE}	R_M	M_{HDE}	M_{gr}	M_{LDE}	R_M
9–9.5	0.53	20	12000	21	0.95	14	9800	19	0.74
9.5–10	0.60	46	11000	41	1.12	32	9700	39	0.83
10–10.5	0.63	140	7300	110	1.27	110	7200	120	0.94
10.5–11	0.48	930	9600	650	1.43	950	5900	660	1.44

		CFHTLenS Data						
$\log m$	f_{sat}	M_{HDE}	$\chi^2_{\mathrm{red,HDE}}$	M_{gr}	M_{LDE}	$\chi^2_{\mathrm{red,LDE}}$	R_M
9–9.5	0.53	17.6 ± 4.8	2.31	20500 ± 2300	24.9 ± 4.0	0.83	$0.71^{+0.25}_{-0.18}$
9.5–10	0.60	16.5 ± 6.5	1.05	15060 ± 900	35.6 ± 6.2	0.80	$0.46^{+0.25}_{-0.15}$
10–10.5	0.63	67 ± 12	0.65	14550 ± 550	95 ± 11	0.90	$0.70^{+0.17}_{-0.12}$
10.5–11	0.48	287 ± 34	1.45	23100 ± 4000	239 ± 38	1.41	$1.20^{+0.30}_{-0.21}$
11–11.5	0.48	1090 ± 120	0.81	20300 ± 2000	530 ± 110	1.29	$2.05^{+0.65}_{-0.31}$

2.6 Results of Photometric Redshift Investigation

In this section, we present the results of the fits and discuss their implications. In Section 2.6.1, we discuss the predicted results from the simulations for both the "No Stripping" and "Stripping" models. In Section 2.6.2, we present the main results of our analysis of the CFHTLenS dataset and discuss their implications. In Section 2.6.3, we discuss alternative interpretations of the data, and which of the one-halo mass, concentration, and truncation radius might plausibly contribute to the observed differences between the HDE and LDE samples. In Section 2.6.4, we discuss potential systematic effects, and in Section B.2 we present preliminary results from the SDSS DR8 data.

2.6.1 Predictions from Simulations

Fig. 2.7 shows plots of the best-fit models for the simulated catalogues from the Millennium Simulation, for both the "Stripping" and "No Stripping models" (described in Section 2.2), for galaxies with $10^9 M_\odot < m < 10^{10.5} M_\odot$. The plot illustrates that in the "No Stripping" scenario, the measured lensing signals for the HDE and LDE samples are nearly identical at very small radii. Our algorithm does not work perfectly for this mass bin, and in the "No Stripping" scenario, it fits a one-halo mass to the HDE sample that is somewhat larger than the one-halo mass fitted to the LDE sample, while for the
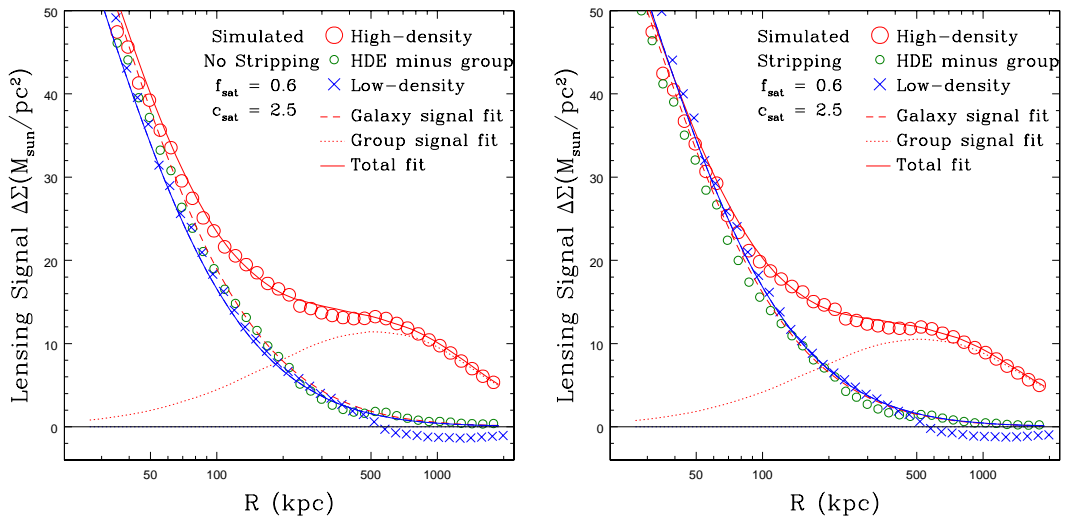
FIGURE 2.7: Lensing signals and fits for simulated lensing data for the "No Stripping" (left) and "Stripping" (right) scenarios (see Section 2.2). The "No Stripping" scenario shows similar one-halo fits for the HDE and LDE samples, while the "Stripping" scenario shows a lower one-halo mass fit for the HDE sample than for the LDE sample. Error bars are not shown, as shape noise is not simulated for these datasets, and so the scatter is extremely small.

"Stripping" scenario, the fitted HDE one-halo mass is slightly lower than the fitted LDE one-halo mass.

Further comparisons of fitted one-halo masses for different mass bins can be seen in Table 2.4 and Fig. 2.10. As can be seen there, for all mass bins $m < 10^{10.5}M_\odot$ with the "Stripping" model, the fit (as expected) yields a relatively lower one-halo mass for the HDE sample compared to the LDE sample than it does for the "No Stripping" model. Above $m = 10^{10.5}M_\odot$, however, the fitted masses in the "Stripping" and "No Stripping" scenarios are comparable. This is due to the fact that at high stellar masses, the fraction of galaxies in the HDE sample that are centrals increases rapidly (see Table 2.3). Since mass stripped from satellites is added to the masses of central galaxies, then if too many central galaxies are included in the sample, stripping will have little or no net effect on the lensing signal.

The fitted group masses for the simulated data in Table 2.4 are larger than the actual group masses by a factor of $\sim$ 1.5–2. Our tests have shown that this can occur when haloes from a very broad range of masses are averaged together, as is the case here. The lensing signal of an average of haloes of varying mass is similar to the lensing signal of a single halo with a mass somewhat greater than the average of the sample.

The fitted group masses for the CFHTLenS data are observed to be a factor of $\sim$ 2 larger than the group masses for simulated data. This is not surprising, as the halo masses in the simulated data are extrapolated from the stellar masses of their constituent

64

galaxies, and the distribution of stellar masses in the simulated data does not match the distribution in the CFHTLenS dataset. As discussed in Section 2.2.2.1 and illustrated in Fig. 2.1, the central galaxies of groups in the simulated data have significantly lower stellar masses than are observed in the CFHTLenS, which results in our estimated halo masses for groups being lower for the simulated data than the actual halo masses in the CFHTLenS.

The results from the simulations imply that with the CFHTLenS data, a comparison of the HDE and LDE fitted one-halo masses can be used as an indication of whether or not tidal stripping is occurring, but we must use a stellar mass upper limit of $\sim 10^{10.5} M_{\odot}$.

2.6.2   Results from CFHTLenS

Fig. 2.8 shows the lensing signals for the HDE and LDE samples taken from the CFHTLenS, including all galaxies with $10^9 M_{\odot} < m < 10^{10.5}\ M_{\odot}$, with the best-fit models plotted on top. For this broad mass bin, the fits show that the HDE one-halo term is lower than the LDE term, at 2.5σ significance ($p = 0.0113$). However, this simple fit is not optimal. In part, this is because we are combining galaxies with greatly varying masses. The resultant lensing signal of this combination does not perfectly resemble the lensing signal of a single halo possessing the average mass of the sample, and the code compensates for this by fitting a higher σ_{m}, which results in larger errors for the best fit.

Fig. 2.9 shows the likelihood distributions for the fitted satellite masses, host group mass, and surface density threshold for the HDE sample of galaxies with $10^9 M_{\odot} < m < 10^{10.5} M_{\odot}$. The plot shows that there is only a weak degeneracy of M_{sat} with the other two parameters, but there is a stronger degeneracy between M_{host} and Σ_{t}. Nevertheless, when marginalized over the other parameters, M_{host} is very tightly constrained, and M_{sat} is reasonably constrained.

We can more carefully analyse the data by splitting the galaxy sample into smaller stellar mass bins. Fig. 2.10 shows the results of this analysis for both simulated and the CFHTLenS data, with the ratio of the fitted one-halo mass for the HDE sample to that of the LDE sample plotted against the galaxies' stellar masses. Simulated data are not available for all of the mass bins due to limitations of the Millenium catalogue.

Details of the fits to CFHTLenS data for different stellar mass bins are shown in Table 2.4. The goodness-of-fit is comparable to previous galaxy-galaxy lensing studies. Specifically, the χ^2_{red} values for our fits (which are calculated before the inclusion of the model error term, see Section 2.5) are similar to the full halo model fits of Velander et al.
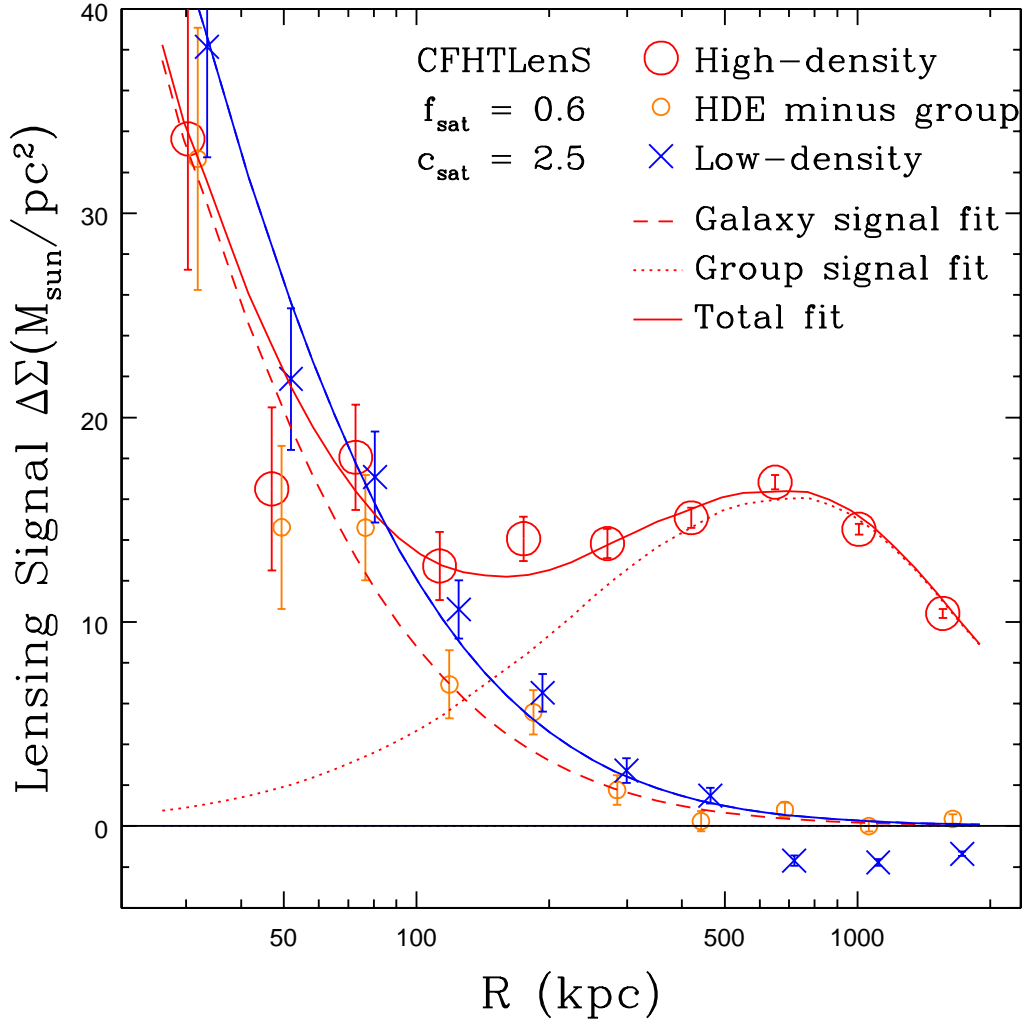
FIGURE 2.8: Measured lensing signal and model fits for data from the CHFTLenS, including all galaxies with $10^9 < m < 10^{10.5} M_\odot$. HDE (red) and LDE (blue) lensing signals and fits are illustrated. The dashed line shows the one-halo model fit to the HDE sample, and the dotted line shows the HDE offset-group-halo term. The one-halo mass fit for the HDE sample is found to be significantly lower than for the LDE sample.

(2013): their $\chi^2_{\rm red}$ values varied from 0.5–2 for different stellar mass bins, whereas ours vary from 0.6–2.3.

If only the three stellar mass bins with $10^9 < m < 10^{10.5} M_\odot$ are used, we obtain a weighted mean ratio of HDE one-halo mass to LDE one-halo mass of 0.65 ± 0.12. If we assume that this ratio is indicative of the retained mass after stripping, and assume the sample contains $\sim 60\%$ satellites, then we can extrapolate that for a sample of 100% satellites, the mean retained mass fraction will be $\sim 0.41 \pm 0.19$, which is consistent with the mean retained mass fraction of 0.40 we measured from the simulated data.

Note that at face value, our result suggests less mass reduction in HDE environments
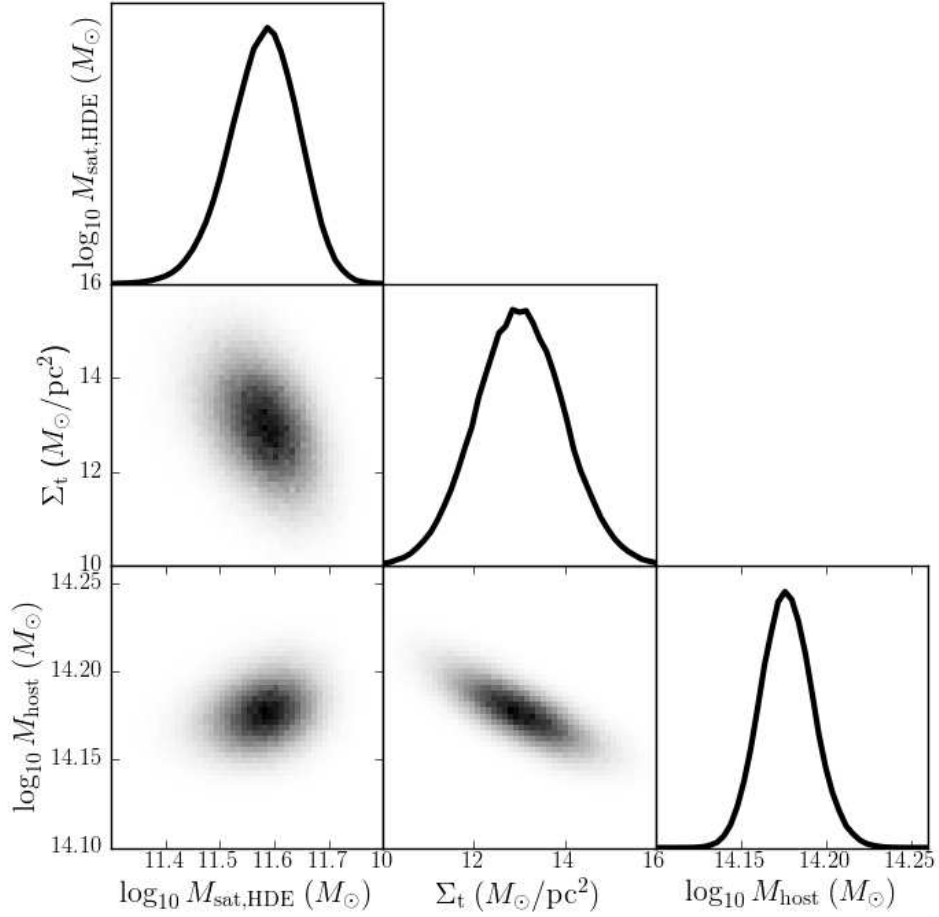
FIGURE 2.9: Probability distribution functions and joint probability distribution functions for satellite mass M_{sat} (left column), host group mass M_{host} (bottom row), and surface density threshold Σ_t (middle row and middle column) for the fit of the lensing signal of all HDE galaxies with $10^9 M_\odot < m < 10^{10.5} M_\odot$.

than the factors of 2–5 found for the $\sim L_*$ satellites of the rich cluster Cl 0024+16 found by Natarajan et al. (2009). There are several key differences between these samples, however; in particular, our satellites have lower stellar mass and our satellites inhabit lower mass host haloes than the rich cluster studied by Natarajan et al. (2009).

These combined results reject the results of the simulated "No Stripping" model at 4.1σ ($p < 0.0001$), reject $M_{HDE} = M_{LDE}$ at 2.9σ ($p = 0.0039$), and are consistent with the simulated "Stripping" model at 1.8σ ($p = 0.0651$). This near-rejection of the "Stripping" model may indicate that this model underestimates the amount of tidal stripping which occurs in reality, or it might indicate that some effect other than tidal stripping (such as a difference in star formation histories dependent on environment) is contributing to the observed signal. Additionally, while our results have high statistical significance, they do not rule out the possibility of systematic errors resulting in a spurious detection. We investigate the possibility of such a spurious detection in Section 2.6.4.
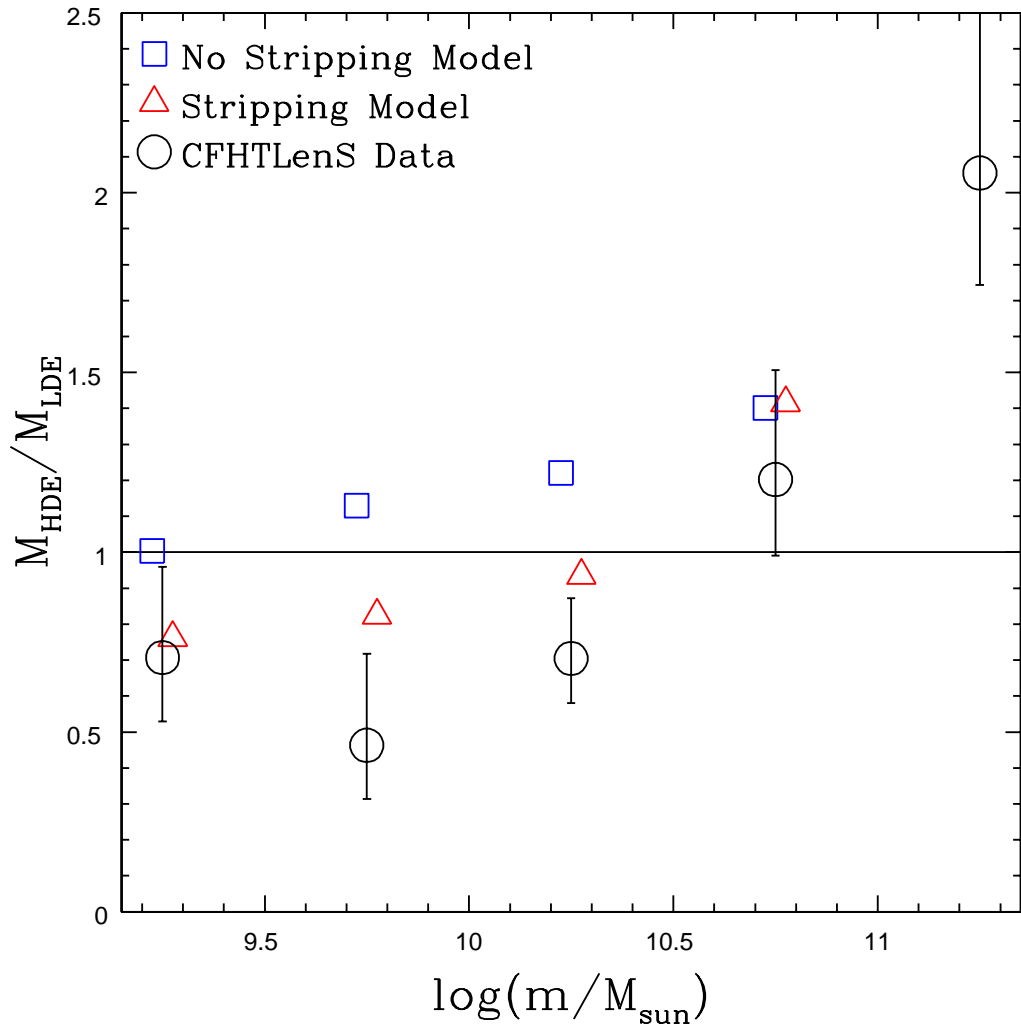
FIGURE 2.10: A summary plot of the fitting results for various stellar mass bins. Shown are the ratios of the best-fit one-halo mass for the HDE and LDE samples, for both the Stripping and No Stripping simulations, and for the CFHTLenS data.

2.6.3 Alternative Fits

In the previous section, we made a number of assumptions relating one-halo mass, concentration, and tidal radius (see Equation (2.2)). This allowed us to compare only the one-halo mass between the HDE and LDE samples, in order to determine if there was a difference in their lensing signals. However, this does not tell us what variations in mass, concentration, and tidal radius might be causing this difference. In this section we investigate alternate means of fitting the lensing signals to determine which of these parameters might differ between the HDE and LDE samples.

2.6.3.1 Truncation Radius

An alternative fit with one free one-halo parameter is to fit the HDE model with the same one-halo mass as the LDE sample, but with a lower tidal (truncation) radius for its halo, as is predicted by typical models of tidal stripping (see Equation (2.1)). For the single broad stellar mass bin $10^9 < m < 10^{10.5} M_\odot$, and fixing the one-halo mass to match that fitted to the LDE sample, we fit a tidal radius of $r_{\text{tidal}}/r_{200} = 0.26 \pm 0.14$ for the HDE galaxies. This corresponds to a typical tidal radius of 40 ± 21 kpc and a retained mass fraction of 0.43 ± 0.18 for a satellite galaxy with $M = 5.9 \times 10^{11} M_\odot$ and $c = 8.5$. This model is only a marginally poorer fit compared to the default method of fitting one-halo mass: $\chi^2_{\text{red}} = 1.08$ for fitting tidal radius, compared to $\chi^2_{\text{red}} = 0.99$ for fitting mass. Our data are thus consistent with both interpretations, and we are unable to discern between them.

2.6.3.2 One-halo Mass and Concentration

It is also possible that the observed difference in lensing signals between HDE and LDE galaxies could be due to a difference in concentration, rather than a difference in mass. Haloes with lower concentrations will have lower lensing signals at small radii, and somewhat higher lensing signals at large radii. To test whether the observed results could be due to a change in concentration, we reran the analysis, leaving concentration as a free parameter. The resultant joint probability distribution function for this analysis is shown in Fig. 2.11. As this plot shows, while there is a difference in the mass PDFs for the HDE and LDE samples, there is no evidence for a difference in concentration between the two samples. We therefore favour the interpretation that the measured difference in lensing signals between the HDE and LDE samples is due to the HDE haloes being less massive than LDE haloes, but we are unable to rule out the possibility that the two samples have the same mass, but the HDE sample is less concentrated.

2.6.4 Analysis

Although the results are statistically significant, it is nevertheless possible that systematic errors have entered our analysis. In this section we discuss various possible systematic errors that may affect the results.
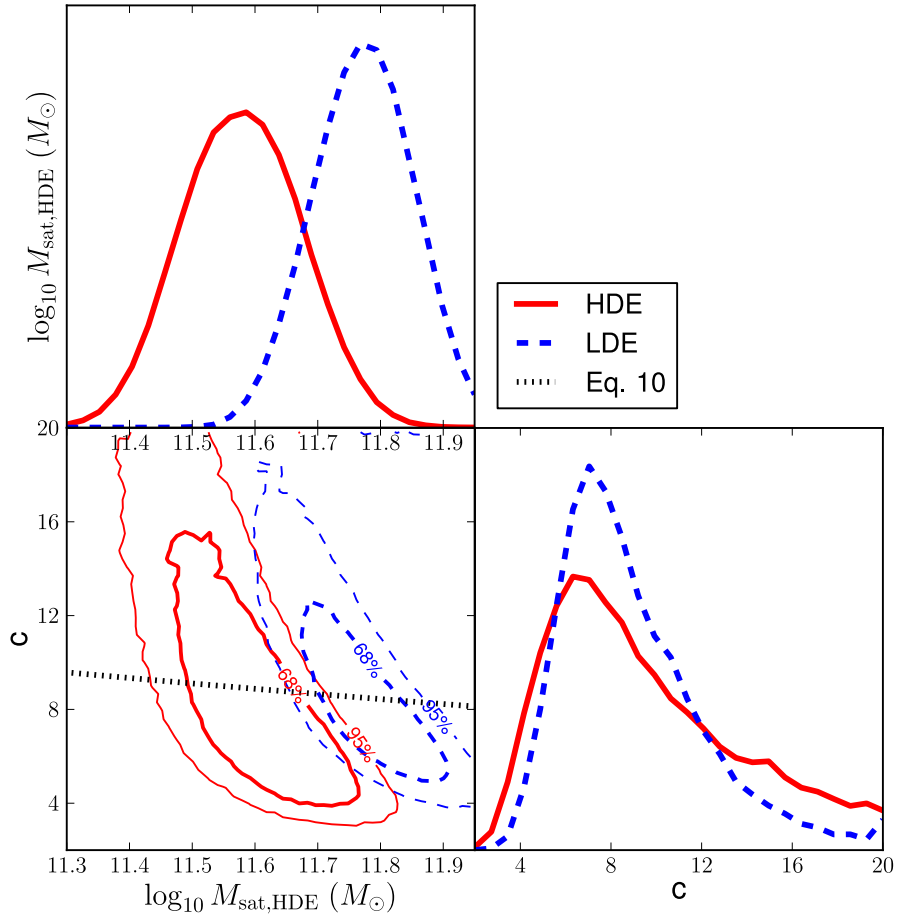
FIGURE 2.11: Lower left: Joint probability distribution function for one-halo mass and concentration for the HDE (red solid lines) and LDE (blue dashed lines) galaxy samples. The dotted line shows the relation between mass and concentration given by Equation (2.2), which was used for previous analysis. Upper left: Probability distribution function for one-halo mass, marginalized over concentration. Lower right: Probability distribution function for concentration, marginalized over one-halo mass.

2.6.4.1 Stellar Mass Biases

In principle, if there is a relative bias in the estimates of stellar mass between red and blue galaxies, and if the HDE and LDE samples contain different fractions of red and blue galaxies, we could obtain a spuriously positive detection of tidal stripping with our method. It is difficult to completely rule out the possibility of a relative bias in stellar mass, but it can be investigated by comparing the distributions of stellar mass to other published distributions. Unlike the CFHTLenS data, the WIRDS (Bielby et al., 2012) data are based on optical photometry supplemented by deep infrared images. We would therefore expect the stellar masses in WIRDS to be more accurate. A comparison of stellar mass estimates between CFHTLenS and WIRDS (Velander et al., 2013) shows that, if we assume WIRDS stellar masses to be more accurate, then CFHTLenS stellar

TABLE 2.5: Results of varying the fixed parameters (f_{sat} and c_{sat}) in the fitting proce-
dure, using a sample of galaxies with $10^9\ M_\odot < m < 10^{10.5}\ M_\odot$ from the CFHTLenS.
All masses are in units of $10^{10}\ M_\odot$.

f_{sat}	c_{sat}	M_{HDE}	R_M	M_{group}	χ^2_{red}
0.4	2.5	44 ± 6	0.76	23000	1.17
0.6	**2.5**	$\mathbf{38 \pm 5}$	**0.65**	**15000**	**0.99**
0.8	2.5	33 ± 5	0.56	12000	1.22
0.4	5.0	35 ± 4	0.59	25000	1.08
0.6	5.0	25 ± 4	0.43	17000	1.93
0.8	5.0	20 ± 4	0.33	9100	12.09

masses may indeed be slightly biased, with CFHTLenS red galaxy stellar masses ~ 0.05–
0.1 dex too low and the opposite for CFHTLenS blue galaxies. Since we are selecting
by CFHTLenS stellar mass, and because red galaxies are more common in high-density
environments, this implies that the true mean stellar mass in HDE regions is actually
slightly larger than that in the "matched" LDE regions. Correspondingly, in the absence
of stripping, we would expect the recovered subhalo masses to be larger. Since we find
them to be smaller, this effect is in the wrong sense to explain our stripping detection.

In any case, the effect is small. As can be seen in Table 2.2, the maximum difference
in the fraction of red galaxies between the HDE and LDE samples is in fact only 10%,
in the $10^{9.5}\ M_\odot < m < 10^{10}\ M_\odot$ and $10^{10}\ M_\odot < m < 10^{10.5}\ M_\odot$ bins. This, combined
with the above estimates of the relative bias, allows us to put an upper limit on this
effect of $\sim 5\%$.

2.6.4.2 Modeling Inaccuracies

We have attempted to account for inaccuracies in the models through the inclusion of a
"model error" term, but this does not account for all possible errors in modelling that
might arise. Notably, for the HDE sample, there is a weak degeneracy between the fitted
one-halo term and the other fitted parameters, as well as with the fixed parameters: the
fraction of galaxies which are satellites (f_{sat}) and the concentration of satellites (c_{sat}).
We marginalize over the other fitted parameters to estimate the mean one-halo mass
and its error, but errors in f_{sat} and c_{sat} would persist through the analysis as systematic
errors.

To assess the potential impact of errors in the fraction of satellites and satellite concen-
tration, we reran the analysis and allowed these parameters to vary. The results plotted
here use a sample of all galaxies with $m < 10^{10.5}M_\odot$, weighted by estimated halo mass.
The results of this analysis are presented in Table 2.5, and sample plots of the fits can
be observed in Fig. 2.12. We allow the fraction of satellites to vary from 0.4 to 0.8,
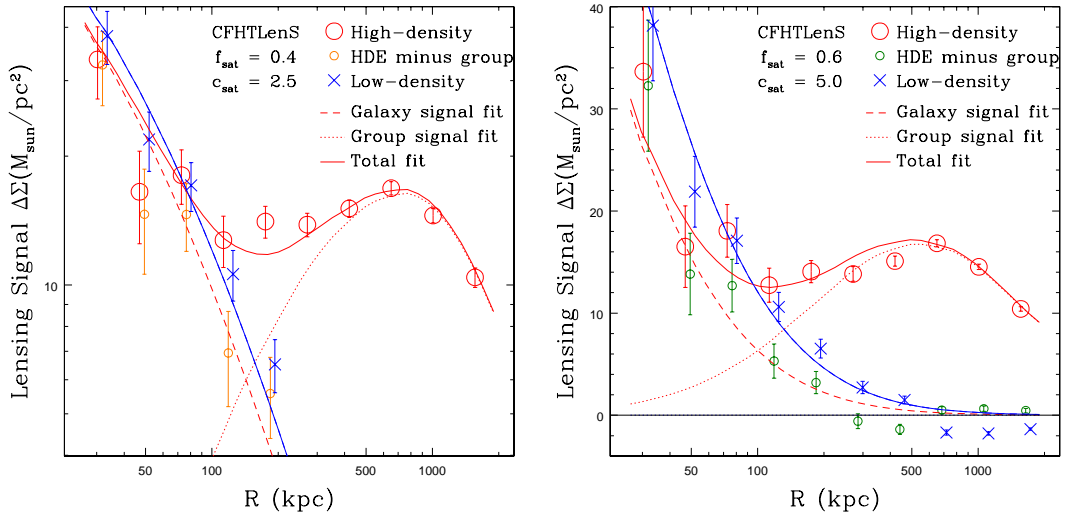
FIGURE 2.12: As Fig. 2.8, except with the fraction of satellites fixed to 0.4 (left), and the concentration of satellites fixed to 5.0 (right) for the fitting of the HDE signal.

TABLE 2.6: Fitted values of Σ_t for various stellar mass bins, in units of $M_\odot/\mathrm{pc}^2$.

$\log m$	Σ_t
9–9.5	42 ± 2
9.5–10	34 ± 3
10–10.5	44 ± 3
10.5–11	39 ± 6
11–11.5	36 ± 7

and we test increasing the concentration of satellites to 5.0, which is comparable to the concentration of the dark matter haloes of galaxy groups.

As compared with the default case ($f_{\mathrm{sat}} = 0.6$ and $c_{\mathrm{sat}} = 2.5$), the only variation of parameters that results in increasing the fitted HDE mass is when the fraction of satellites is decreased. If the tested fraction of 0.4 were the case in reality, the significance of the detection would decrease to $\sim 2.1\sigma$. However, this particular satellite fraction results in a marginally poorer fit, as evidenced by the increased χ^2_{red} value.

Alternatively, if the actual concentration of satellites within groups is higher, the fitted satellite mass will be lower. A fit with $c_{\mathrm{sat}} = 5.0$ yields a marginally poorer χ^2_{red} value, but we cannot rule out this scenario. If this is the case in reality, it would strengthen the significance of the detection to $\sim 4.4\sigma$.

It is also important to look at the impact of the density threshold term, Σ_t. Although this term was found to be necessary in the simulated data to provide a reasonable fit when the fraction of satellites is known exactly, it is not certain that this is an accurate description. We can investigate this matter by looking at how the fitted value of Σ_t varies in the fits, as can be seen in Table 2.6. If we were modeling everything perfectly,

we would expect to see Σ_t being roughly constant for all stellar mass bins, as the P3 algorithm is blind to galaxy mass, and so there is no reason the threshold Σ_t for S/N > 2 regions should vary with the mass of satellites. In fact, we observe Σ_t to remain roughly constant at $\sim 40 M_\odot/\text{pc}^2$, which is consistent with the hypothesis that we are modeling it reasonably.

Other modeling inaccuracies may also affect the results. The model for the HDE sample neglects the contribution of the two-halo term (the contribution of nearby groups and field galaxies) to the lensing signal around satellites. We tested the implications of this with a rough model of the two-halo term, and it resulted in decreasing the fitted HDE satellite mass. Therefore, any possible systematic error in our results from this effect would be in the wrong sense to contribute to a spurious detection.

Additionally, the model for the LDE sample neglects the contribution of the local under-density (see Section 2.4.3) to the lensing signal. Proper handling of this term would likely result in a slight increase in the fitted LDE mass, which would increase the significance of the detection.

Chapter 3

Methods Using Spectroscopic Redshifts

If spectroscopic redshift data for a large sample of lens galaxies is available, as is the case with the GAMA survey (Driver et al., 2011), we can determine to high accuracy– $\sim 80\%$ purity and completeness (Robotham et al., 2011)–which galaxies are in fact satellites. We can then use information on satellites' placement within groups to better estimate the contributions of their host groups to the observed lensing signals. We can also use group assignment information to bin our lens samples by the masses of their host groups, which will potentially allow us to detect whether there is a change in the extent of tidal stripping with host group mass.

In Section 3.1, we discuss the simulated catalogues we use for our analysis. In Section 3.2, we present the methods we use for isolating the lensing signals of the dark matter haloes of satellites. In Section 3.3, we analyse the performance of the methods tested, and we discuss these results in Section 3.4. In Section 3.5, we discuss which method performs best, and in Section 3.6, we discuss the projected S/N of tidal stripping detections for various planned and proposed surveys.

In this chapter, we use m_{min} and m_{max} to define the lower and upper limits, respectively, for total (dark + stellar) satellite mass in our samples, and M_{min} and M_{max} to define the lower and upper limits, respectively, for the total masses of the groups in which they reside.

3.1 Simulations

We use the same simulated catalogues and halo models as discussed in Section 2.1 and Section 2.2, with modifications to the lens catalogues to approximate the originally-planned completeness limit of the GAMA-II survey (Driver et al., 2011), applying a magnitude cut of $r < 19.8$ to this catalogue. For our estimates of statistical errors in this chapter, we assume that the survey will cover 50 deg^2 of sky after masking, with the same source density (effective 11 sources/arcmin^2) and depth as the CFHTLenS.

For this analysis, we use an additional two datasets for comparisons and tests, compared to our work with photometry alone:

- Pure Group: A test case in which all group mass is assigned to the central halo, and the masses of all satellite haloes are set to zero.

- Particle Ray-Tracing (PRT): This dataset uses the ray-tracing simulation performed by Hilbert et al. (2009), which uses the positions of dark matter particles rather than our halo models. Groups are selected using the group masses in the catalogue from De Lucia and Blaizot (2007), rather than our calculated M_{tot}.

3.2 Methodology

With each subset of lens galaxies, we calculate the average tangential shear within radial bins. The subsets of satellites will typically show some contribution from their groups' haloes to the lensing signals around them. Since the observed lensing signal around satellites is the combination of the contributions from the satellites' haloes and their groups' haloes,

$$\Delta\Sigma_{\text{obs}} = \Delta\Sigma_{\text{group}} + \Delta\Sigma_{\text{sat}}, \tag{3.1}$$

we can isolate the portion of the signal contributed by the satellites' haloes ($\Delta\Sigma_{\text{sat}}$) by estimating the groups' contribution to the lensing signal ($\Delta\Sigma_{\text{group}}$) and subtracting it from the observed lensing signal ($\Delta\Sigma_{\text{obs}}$). We have applied the two methods detailed below to do this, and we compare their results in Section 3.3.3.1 and Section 3.3.4.

3.2.1 Mirror Method

The first method for isolating the satellite's contribution to the lensing signal involves using a "mirror" point in the group to measure the group's contribution to the satellite's lensing signal. This sample point is placed opposite the group centre from the satellite,
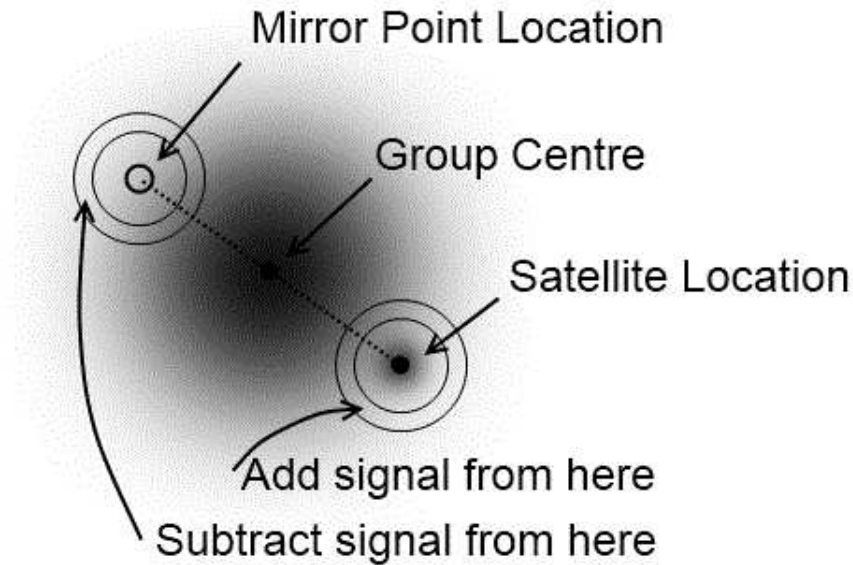
Figure 3.1: An illustration of the Mirror Method. For each satellite used as a lens, we also calculate the lensing signal around a point opposite the group centre from this satellite. We subtract this signal from the signal around the satellite to correct for the contribution of the group's halo to the lensing signal. See also Figure 1 of Pastor Mira et al. (2011) and related discussion.

at the same distance from it, as illustrated in Fig. 3.1. In an ideal scenario, the lensing signal around this sample point will include exactly the same contribution from the group's halo as at the satellite's location, while including little contribution from the satellite itself.

One might consider alternative methods to sample the lensing signal of a galaxy groups, such as using an annulus of sample points rather than a single sample point opposite the group centre. However, the use of only a single sample point has two important advantages:

1. This method assumes that some form of symmetry must be present within the group in order for the lensing signal around the sample point to approximate that around the satellite. Use of an annuli of points requires axial symmetry, but use of a single sample point requires only mirror symmetry, which is satisfied in the case of triaxial group haloes.

2. The lensing signal around any sample point will see some contribution from the satellite's halo, in addition to the group's (see Equation (1.43)). The closer the sample point is to the satellite, the greater this contribution will be, and thus the

76

more lensing signal will be lost from the satellite. This effect is minimized by the use of only a single sample point opposite the group centre from the satellite.

This method is in practice identical to the "Galaxy-Galaxy Lensing with Calibration" method used by Pastor Mira et al. (2011). Figures 1 and 2 in that paper provide a useful illustration of how this method functions, and discussion of it is found in Section 3.

3.2.2 Ensemble Method

The second method involves estimating the masses of groups and their contributions to the lensing signals around their satellites. First, we create a sample of groups with $M_{\min} < M < M_{\max}$ and each with at least one satellite with $m_{\min} < m < m_{\max}$. We use a weighted average of the groups' masses to generate an "ensemble" halo, representative of the sample. We then assign this ensemble halo a concentration based on Equation (2.2). For each source in the sample, we then use our ensemble haloes and the positions of group centres to calculate the group's expected contribution to the source's ellipticity and subtract off this amount.

3.3 Analysis of Spectroscopic Redshift Methods

In this chapter we present the lensing signals that result from our simulations and discuss the effects of various sources of error on these signals. In Section 3.3.1, we discuss the dominant sources of error in this type of analysis. In Section 3.3.2, we present the lensing signals that result when group centres are stacked together. In Section 3.3.3, we present the lensing signals that result when satellite galaxies are stacked together, we show the effects of our methods to reduce the contributions of group centres to these signals, and we investigate the effects of centring and group mass errors on these signals.

3.3.1 Dominant Sources of Error

In order to properly assess whether our methods for measuring satellites' lensing signals are viable with observational data, it is necessary to account for the sources of error present in such datasets. In this section, we explain the major sources of error we expect in datasets and how we replicate them in our simulations.

3.3.1.1 Shape Noise

There is significant variation in the orientation of galaxies in the sky, independent of the effects of gravitational lensing. The distribution of the unlensed shapes of background galaxies can be approximately modeled by a Gaussian distribution for both components of ellipticity, with a mean of zero and a standard deviation of 0.28. This value was calculated from the distribution of ellipticities measured in background galaxies in the CFHTLenS, estimated with the lensfit method (Miller et al., 2007, Kitching et al., 2008, Heymans et al., 2012).

We account for the impact of shape noise on our measurements by setting the size of the error bars in our plots to account for its expected impact. This allows us to precisely predict the mean expected measurements, unaffected by shape noise, and to estimate the scatter that will be seen in observational data. Our error estimates assume data from a survey similar to the overlap of the CFHTLenS survey and the GAMA-II survey. This hypothetical survey covers 50 deg.^{2} of the sky, with an effective 15 sources per arcmin.^{2} and galaxy spectra complete to $r < 19.8$.

3.3.1.2 Group Mass and Group Assignment Errors

With observational data, group masses must be estimated through one of various methods, such as using the velocity dispersion of constituent galaxies, the luminosity of the group, X-ray emissions, or lensing signals. In the GAMA surveys, group masses are estimated primarily through velocity dispersions, so this is the method that we simulate here. To do this, we first determine which of the galaxies in a group are within the detection limits of the survey. For each of these galaxies, we generate a random line-of-sight velocity from a Gaussian distribution, where the dispersion is determined by the total mass of the group, as given in the catalogue from De Lucia and Blaizot (2007). For all calculations relating σ_1 and M_{200}, we assume a Singular Isothermal Sphere (SIS) profile, which gives us the relation:

$$\sigma_1 = (10 G h M_{200})^{1/3} / \sqrt{3}. \tag{3.2}$$

When groups are detected through a friends-of-friends algorithm, it is expected that some portion of the galaxies believed to be within a group will in fact be "interlopers." This happens when field galaxies lie at a similar position in the sky as a group at a different cosmological redshift, but with a peculiar velocity that makes their apparent redshift lie within the redshift distribution of galaxies within the group. For a given

FoF-detected group, typically 20% of the galaxies identified as belonging to it are in fact interlopers (Robotham et al., 2011).

To simulate the effects of interlopers on group mass estimates, we first determine the number of interlopers that a given group contains. Since the number of interlopers should be proportional to the projected area of the group, we set the mean number of interlopers in a given group proportional to $N_{\mathrm{gal}}^{2/3}$. We then use a Poisson distribution to generate the number of interlopers for each group, normalized so that a group with 10 members will have an expected 2.5 interlopers (resulting in a 20% interloper fraction). For each of these interlopers, we then generate a velocity, drawn from a uniform distribution, $v_{\min} - v_{\mathrm{tol}} < v_{\mathrm{rand}} < v_{\max} + v_{\mathrm{tol}}$, where $v_{\min}$ and $v_{\max}$ are the minimum and maximum velocities of real members of this group, and v_{tol} is the velocity tolerance used by the FoF algorithm. In the algorithm used for the GAMA surveys, v_{tol} is not fixed, and in fact depends on the luminosities of the galaxies being linked, but for simplicity's sake, we use a constant value of 150 km/s here.

Once velocities for real members and interlopers are generated, we then calculate the predicted group mass using these velocities. When this mass is used in our analysis, we use the subscript "dyn."

The presence of interlopers will also affect the lensing signal for the "Stripping" model, as interlopers would typically be field galaxies, which will exhibit an unstripped mass distribution. To simulate this effect, we recalculate the signal in the "Stripping" model as:

$$\Delta\Sigma_{\mathrm{S,new}} = 0.8 \times \Delta\Sigma_{\mathrm{S,old}} + 0.2 \times \Delta\Sigma_{\mathrm{NS}}, \tag{3.3}$$

where $\Delta\Sigma_{\mathrm{S}}$ is the lensing signal found with the "Stripping" model, and $\Delta\Sigma_{\mathrm{NS}}$ is the lensing signal found with the "No Stripping" model.

We use both the modifications to group mass, which affects the binning by group mass, and the simulation of the contamination caused by interlopers only for the plots shown in Section 3.3.4, which attempt to predict the strength of the signal with a CFHTLenS + GAMA-II-like survey (see Section 3.3.1.1).

3.3.1.3 Centring Errors

It is not trivial to determine the location of a group's centre. Since the majority of the mass in a group is dark matter, and galaxies are an imperfect tracer of the dark matter distribution, any method which uses galaxies' positions to estimate the centre of a group's dark matter halo will have some degree of error. The amount of error can be roughly estimated by analysis of the velocity dispersion about suspected centres, as done
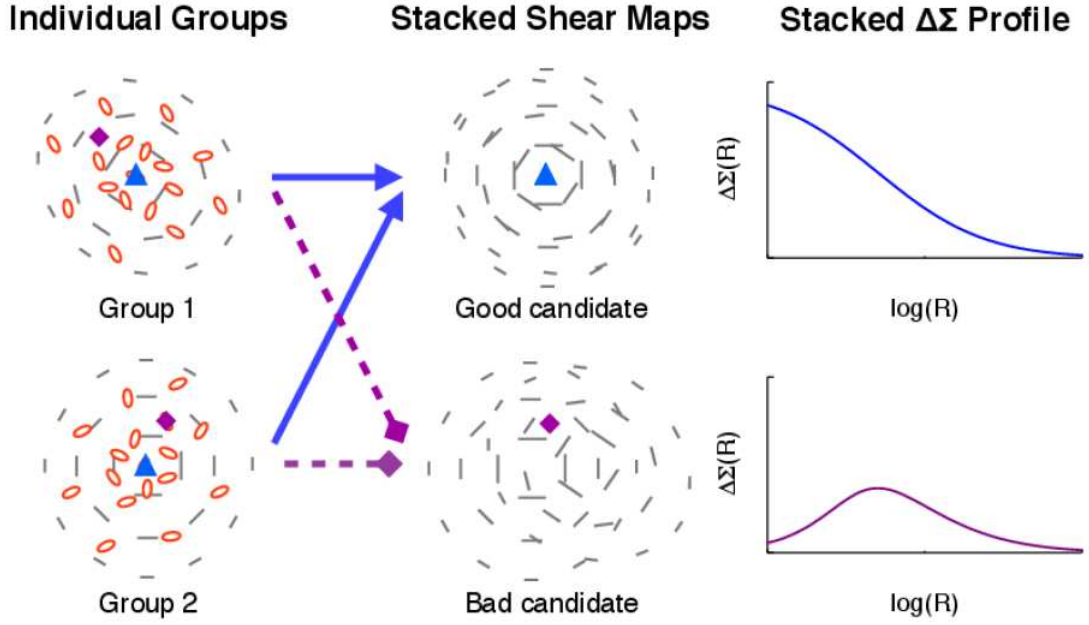
FIGURE 3.2: Figure 2 from George et al. (2012), showing a schematic illustration of the result of centring errors on the lensing signals around group centres. The blue squares represent the actual centres of the groups, and the magenta triangles represent false centres. The top row shows the resultant stacked lensing signal when groups are stacked on their actual centres, and the bottom row shows the result when groups are stacked on false centres.

by Skibba et al. (2011); by comparing the results of multiple independent methods for identifying the group's centre, or by fitting the lensing signal around a stack of groups with a profile convolved with error, as done by George et al. (2012); or through direct analysis of N-body simulations, as done by Johnston et al. (2007). While Johnston et al. (2007)'s analysis of simulations implies that rich groups are less likely to be miscentered than poor groups, this does not seem to be the case with real groups. Recent work by Skibba et al. (2011) and George et al. (2012) all show that this trend is in fact reversed in real groups.

In Fig. 3.2 we show an illustration from George et al. (2012) on how centring errors affect the lensing signals around group centres. When the lensing signals around group centres are measured, the models presented in that paper can be used to fit proper amount of centring error from the lensing signal around a sample of group centres. In testing this on groups identified through X-ray detections, the authors found that for the most massive groups, the centre is misidentified roughly 40% of the time, implying that misidentifying the BCG is a significant problem. The typical magnitude of the error when the group is mis-centred is found to be $\sim 0.7 r_\mathrm{s}$. The authors also demonstrated that using either the most massive or brightest galaxy in a group as the centre is the optimal method when X-ray observations are not available.

80

To simulate the effects of centring errors, we assume that all groups are miscentered according to a 2D Gaussian with σ proportional to their scale radii r_s. When groups are stacked together, this leads to roughly the same net effect as observed previously, but it allows us to adjust the magnitude of the effect by altering only the constant of proportionality (rather than both the fraction of groups in which the centre is misidentified and the dispersion of the false centres relative to the real centres), to easily compare different amounts of error. This does not, however, perfectly match the best fit models of George et al. (2012), so only qualitative conclusions should be made from our simulations involving centring error. We compare models with centring errors $\sigma = 0$, r_s, and $2r_\mathrm{s}$, which covers the expected range of error. When real data are available, it will be necessary to determine the proper amount of error through an analysis of the lensing signals around suspected group centres, and then recalibrate our predictions for it, using a method similar to the George et al. (2012) method of fitting the lensing signals with an NFW profile convolved with centring error.

For the Mirror Method, centring errors will have an impact because if there is error in the location of the group's centre, there will also be error in the location of the mirror point. On average, this error will cause the mirror point to lie farther away from the group centre than it actually should, and so it underestimates the group's contribution to the lensing signal around its satellite.

For the Ensemble Method, centring errors will affect the calculated signal from the ensemble halo. The reason for this is that errors in the positions of group centres will suppress the group signal at low radii ($R \lesssim \sigma_\mathrm{cen}$), thus causing a lower mass to be fit. They will also change the calculated satellite distances from group centres, increasing them more often than decreasing them, and thus decreasing the ensemble halo's typical impact on source ellipticity. In practice, this effect is somewhat smaller than the effect of centring errors on the Mirror Method (see Section 3.3.4 for details).

3.3.2 Lensing Signal around Group Centres

Since the expected form of the lensing signal around group centres is well-understood, measuring this signal in our simulations provides a useful test to confirm that our models behave as expected. Fig. 3.3 shows the average lensing signals around a sample of group centres with $10^{13} \ \mathrm{M_\odot} < M_\mathrm{tot} < 10^{14} \ \mathrm{M_\odot}$, where M_tot is the total mass of the group, for all of our mass models and the particle ray-tracing data (PRT), with no centring or group mass errors applied. Our models show rough agreement with the PRT lensing signal at large radii, although the PRT signal drops significantly below the models' signals for sources within ≈ 50 kpc. This effect was noticed by Hilbert et al. (2009), and is due
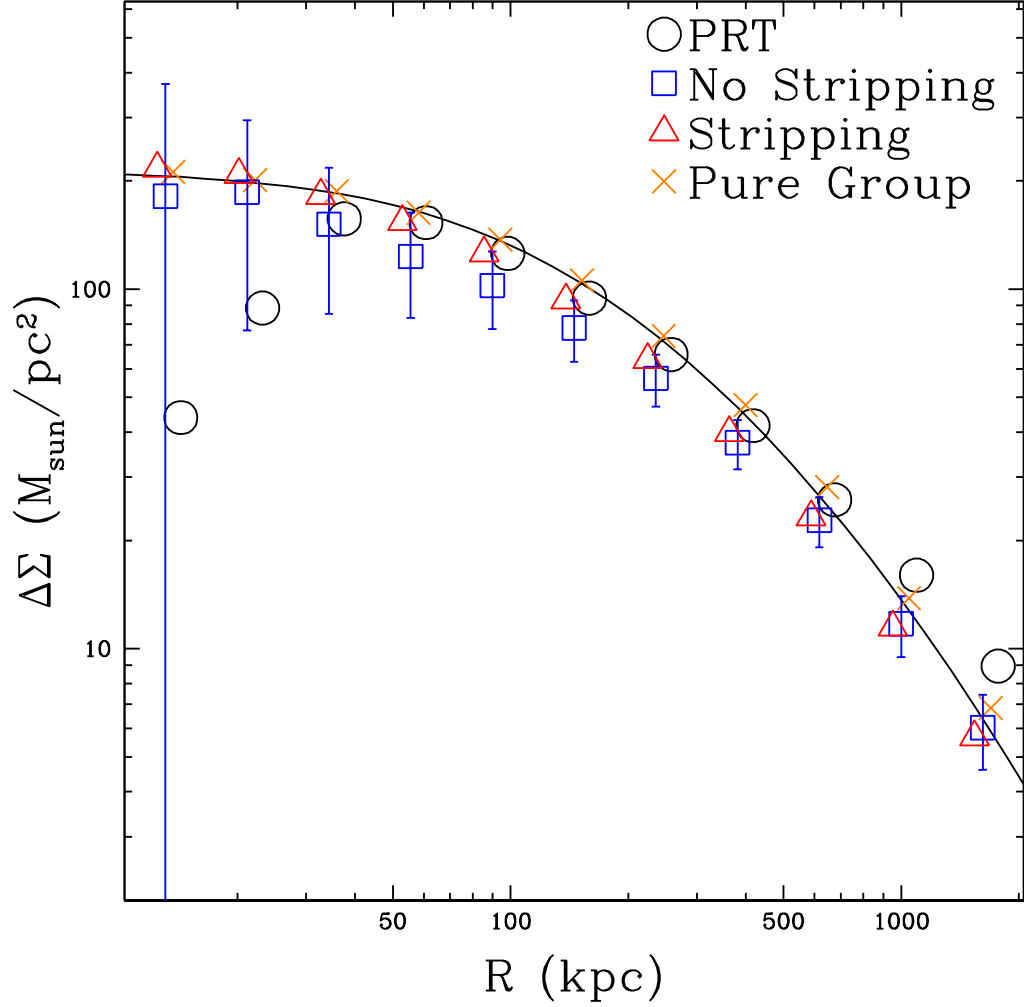
FIGURE 3.3: Lensing signal, measured with $\Delta\Sigma$, around a sample of galaxy groups with 10^{13} $M_\odot$ < M_{tot} < 10^{14} $M_\odot$ drawn from the Millennium Simulation, with no centring or group mass errors applied. All four mass models detailed in Section 2.2.2 are shown here, along with the lensing signal that results from using the particle ray-tracing (PRT) shear data. The solid line shows the predicted shear for a group which has the weighted average mass of the sample ($\overline{M_{tot}} = 4.00 \times 10^{13}$ $M_\odot$) at the weighted average redshift of the sample ($\bar{z}_{gr} = 0.18$). Error bars are shown for the No-Stripping model which represent the projected errors for data from a hypothetical CFHTLenS + GAMA-II-like survey (see Section 3.3.1.1).

to force softening used within the Millennium Simulation, which flattens the cusps of haloes, as well as the smoothing applied during the ray-tracing to suppress particle shot noise.

All of our models appear similar in this regime, with a slight tendency for the "No Stripping" and "Stripping" models to fall below the "Pure Group" model. This implies that our contracted NFW profile is not a perfect model for the background halo of a group with significant substructure in it. More work will be required to determine a better model for this. This effect is minor, however, and all lensing signals are consistent with an NFW profile. If centring errors (see Section 3.3.1.3) are present in observational data, the lensing signal around group centres should be suppressed at low radii.

3.3.3 Lensing Signal around Satellites

Fig. 3.4 shows the average lensing signals around a sample of satellite galaxies with 10^{10} M$_\odot$ < m_{halo}, where m_{halo} is as used in Equation (2.3), and 10^{13} M$_\odot$ < M_{tot} < 10^{14} M$_\odot$, for all of our mass models and the particle ray-tracing data. The differences between our models are in principle detectable with the amount of data available in our hypothetical CFHTLenS + GAMA-II-like survey (see Section 3.3.1.1). At radii larger than ~ 50 kpc, the PRT signal lies close to our No Stripping model, which is an encouraging sign that our models are giving reasonable results. However, our "No Stripping" model is noticeably different from the "Matched Field" dataset, due to the contributions of the satellites' host groups to the lensing signal, and this difference is greater than the difference between it and the "Stripping" model. The "Pure Group" model, as shown here, shows only the lensing signal that results from setting the satellite masses to zero in our simulations, and so it can be used as an approximation of the group haloes' contribution to the lensing signal around satellites. In order to use the "Matched Field" dataset as a standard for comparison, it will be necessary to eliminate the groups' contributions to the lensing signals measured here. This may be possible through one of the methods outlined in Section 3.2. Below we have presented the results of our tests of these methods.

3.3.3.1 Idealized Group Signal Subtraction

As detailed in Section 3.2.1, the Mirror Method uses a sample "mirror" point opposite the group centre from a satellite to estimate the contribution of the group to the lensing signal around the satellite. Fig. 3.5 shows the result of applying this to a sample of satellite galaxies with 10^{10} M$_\odot$ < m_{halo} and 10^{13} M$_\odot$ < M_{tot} < 10^{14} M$_\odot$, in the idealized scenario in which there are no errors in the positions of group centres or the estimated
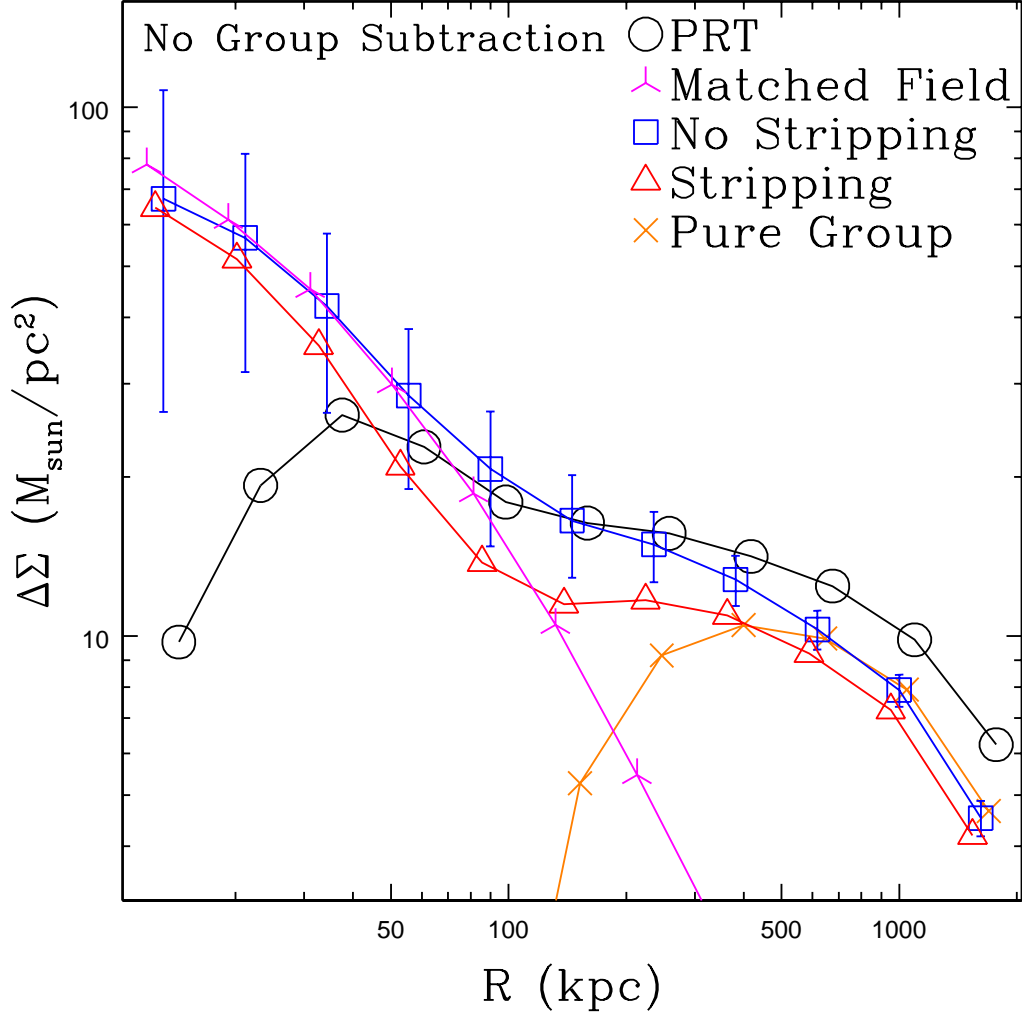
FIGURE 3.4: Lensing signal, measured with $\Delta\Sigma$, around a sample of satellite galaxies with 10^{10} $M_\odot < m_{halo}$ (as determined with the "No Stripping" mass model), and 10^{13} $M_\odot < M_{tot} < 10^{14}$ $M_\odot$, drawn from the Millennium Simulation. All three mass models detailed in Section 2.2.2 are shown here, along with the "Matched Field" dataset and the lensing signal that results from using the particle ray-tracing shear data with a similarly-cut sample of lenses. Error bars are shown for the No-Stripping model which represent the projected errors for data from a hypothetical CFHTLenS + GAMA-II-like survey (see Section 3.3.1.1).
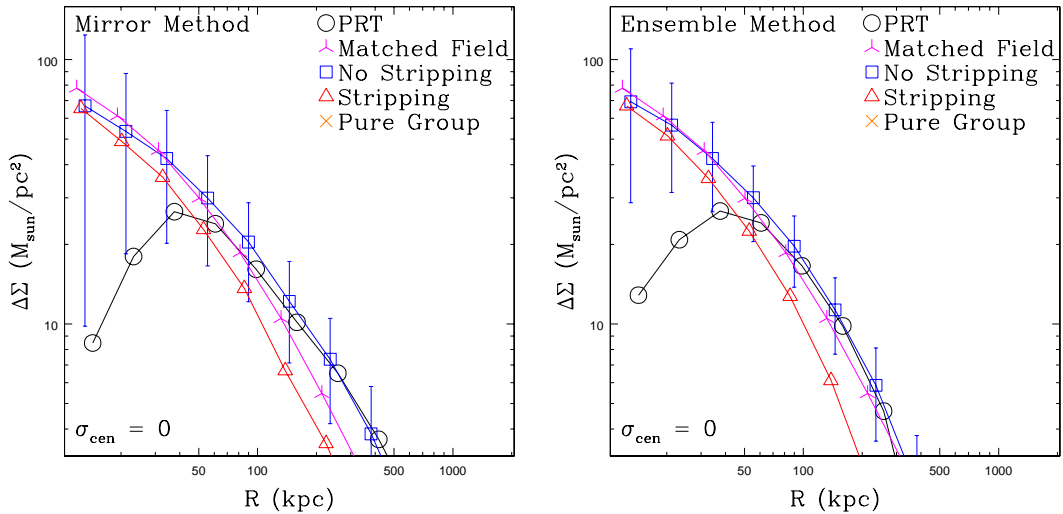
FIGURE 3.5: Same as Fig. 3.4, except with the Mirror Method (left panel) and Ensemble Method (right panel) applied to reduce contribution to the lensing signal from groups' haloes (except with the "Matched Field" dataset).

masses of groups. As can be seen in the figure, the curve for the "No Stripping" model is very similar to that of the "Matched Field" dataset, and the "Pure Group" model has disappeared off the bottom of the plot (it is consistent with zero). This implies that the method does a satisfactory job of eliminating the contribution of the groups to the lensing signal around their satellites. The signal-to-noise in the difference between the "No Stripping" and "Stripping" models is quite strong.

The Ensemble method, explained more thoroughly in Section 3.2.2, uses the average mass of the groups in the sample as an average "Ensemble" halo. For each group centre, its predicted shear is then subtracted from the ellipticities of all nearby source galaxies. After this, satellites are stacked together, and the lensing signal around them, using the altered ellipticities, is measured. Fig. 3.5 shows the result of applying this method to a sample of satellite galaxies with 10^{10} $M_{\odot} < m_{halo}$ and 10^{13} $M_{\odot} < M_{tot} < 10^{14}$ $M_{\odot}$, also in the idealized scenario of no centring or group mass errors. The signals from the "No Stripping" model show good agreement with the "Matched Field" model. Notably, the difference between the "Stripping" and "No Stripping" models here is greater than when the Mirror Method is used. This is because the Mirror Method results in some of the lensing signal around satellites being lost, particularly for satellites near the centres of groups. Although the Ensemble Method requires more assumptions about the physical properties of the groups, it does not face this problem, and so the resultant signal-to-noise in the difference between the two models is larger.
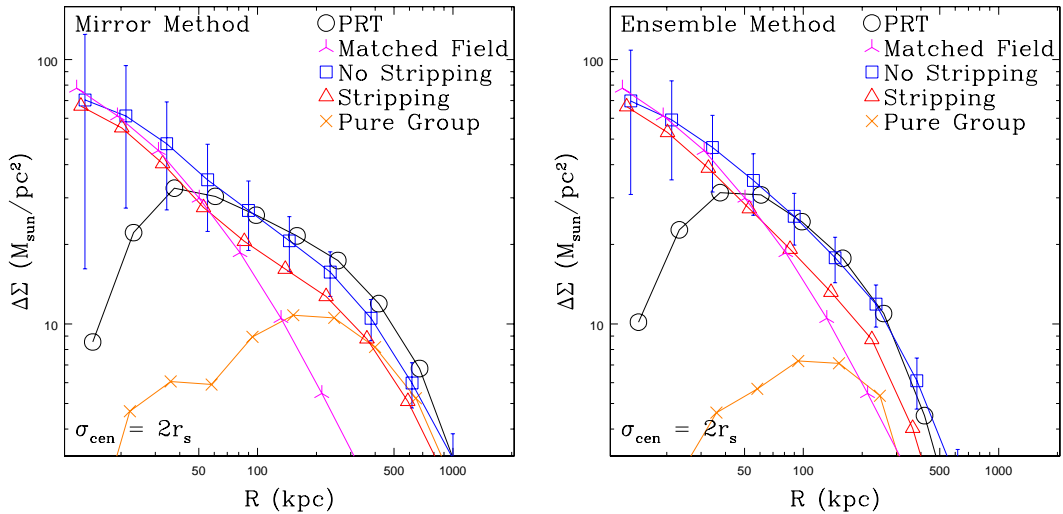
FIGURE 3.6: Same as Fig. 3.4, except with the Mirror Method (left panel) and Ensemble Method (right panel) applied to reduce contribution to the lensing signal from groups' haloes (except with the "Matched Field" dataset), assuming centring errors of $\sigma = 2r_s$.

TABLE 3.1: Statistics for our galaxy samples and NFW profile fits, using the Ensemble Method and assuming $\sigma_{cen} = 0$. All masses are in units of 10^{10} M$_\odot$. S/N$_{F-S}$ is the signal-to-noise ratio in the difference between the fitted masses for the "Field" and "Stripping" models, and S/N$_{NS-S}$ is the same for the difference between the "No Stripping" and "Stripping" models.

	Matched Field				No Stripping				Stripping			
$\log M$	$\overline{z}$	$\overline{m}_{halo}$	m_{fit}	$m_{fit,err}$	$\overline{z}$	$\overline{m}_{halo}$	m_{fit}	$m_{fit,err}$	m_{fit}	$m_{fit,err}$	S/N$_{F-S}$	S/N$_{NS-S}$
12–13	.15	42	45	9.4	.14	47	34	13	18	11	1.43	2.11
13–14	.18	93	97	18	.16	93	77	19	43	15	1.88	2.33
14–15	.14	64	82	25	.12	70	90	27	47	21	1.61	1.38

3.3.4 Realistic Group Signal Subtraction

With observational data, the positions of group centres will not be precisely defined, so it is necessary to assess the impact of centring errors on the utility of this method. Fig. 3.6 shows how the lensing signal appears if centring errors of $\sigma_{cen} = 2r_s$ are assumed. We choose this form for centring errors as it has the general behaviour of increasing error with increasing group mass. We simulated this by applying a 2-dimensional Gaussian deviate to the positions of groups centres. This amount of centring error is significantly higher than the errors found by George et al. (2012) in fitting lensing signals (with a model for centring error) around groups, which were typically of order $\sigma_{cen} \approx 0.5r_s - 1r_s$, and so this provides an upper bound to the amount of centring error that might be seen in observational data. As can be seen through comparison with Fig. 3.5, centring errors have a significant impact on the resultant lensing signal.

To determine whether or not we will be able to detect a difference between the "Stripping" and "No Stripping" models when centring errors are present, we have plotted the
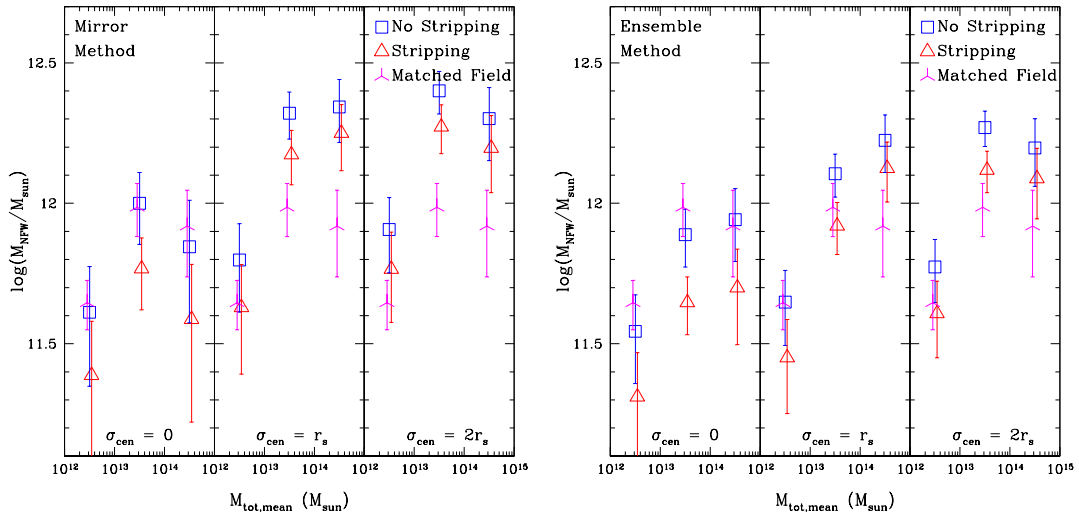
FIGURE 3.7: Best-fit NFW masses for a sample of satellite galaxies with 10^{10} $M_\odot <$ m_{halo} (as determined with the "No Stripping" mass model) drawn from the Millennium Simulation, using only source galaxies within 10 to 400 kpc of the lens galaxies. Satellites from three ranges of group mass are included, shown at the average mass for the range, and the Mirror Method (left panel) and Ensemble Method (right panel) have been applied with three different levels of centring error assumed. Centring errors used were $\sigma_{\text{cen}} = 0$ (left), $\sigma_{\text{cen}} = r_{\text{s}}$ (centre), and $\sigma_{\text{cen}} = 2r_{\text{s}}$ (right). Error bars shown are the projected errors for data from a hypothetical CFHTLenS + GAMA-II-like survey (see Section 3.3.1.1). The "Matched Field" mass is observed to increase with group mass as more massive groups typically contain more massive satellites, and these more massive satellites are then matched to more massive field galaxies.

best-fit NFW mass (determined by minimizing the χ^2 statistic for the group-subtracted lensing signal around satellites in radial bins between 10 and 400 kpc) for our "Stripping" and "No Stripping" models in both group mass bins in Fig. 3.7, for varying amounts of centring error. As this figure shows, centring errors increase the best-fit masses in all mass bins, but it is only a significant problem for the more massive groups. If we have no knowledge of how large centring errors in observational data will be, the uncertainty they cause will be too large for us to distinguish between stripped and unstripped models. This is unlikely to be the case, however, as we will be able to measure the lensing signals around group centres to estimate the magnitude of centring errors through a fit such as that performed by George et al. (2012) (see the discussion in Section 3.3.1.3), and significant amounts of error will manifest as a much-poorer χ^2 fit. Details for all models, assuming no centring error, can be seen in Table 3.1.

Fig. 3.8 shows the projected best-fit NFW masses for different group mass bins if there is significant error in our estimates of group masses. This causes bleeding between bins, increasing the expected mass in all group mass bins. We have illustrated this effect by using the dynamical mass for binning. Note that estimates of halo mass from stellar
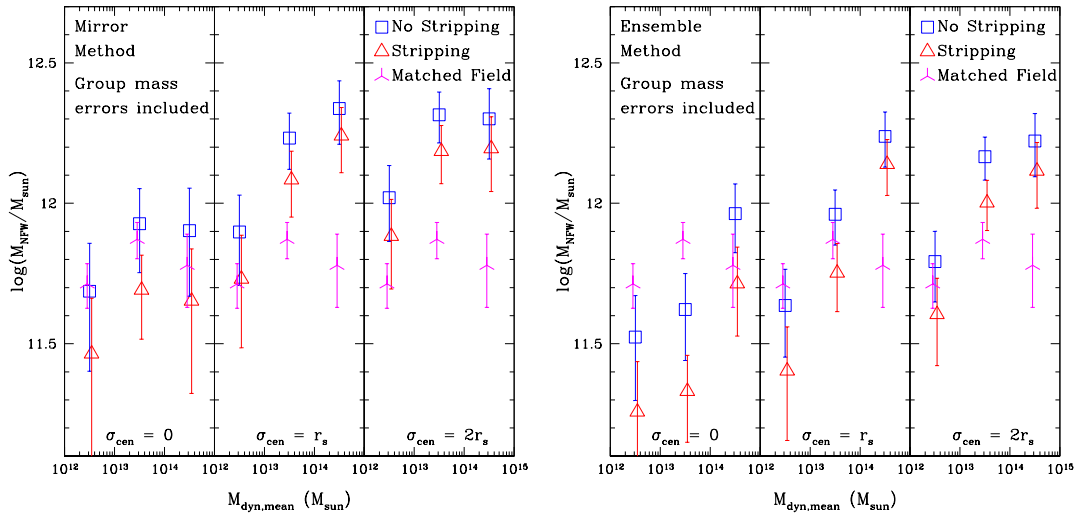
FIGURE 3.8: Same as Fig. 3.7, except satellites have been binned by their groups' estimated dynamical masses instead of the actual masses.

mass will likely have much lower scatter, so this should be seen as an upper bound for the effect of binning error.

3.4 Discussion

As our tests have shown, tidal stripping will have a significant effect on the lensing signals of satellites within groups. However, various sources of error make the detection of this effect more difficult in practice. As is the case with any weak lensing measurements using shear, shape noise is the largest source of error and the most difficult to overcome – it can only be reduced by gathering more data. By determining the expected signals for stripped and unstripped satellites, we can estimate the amount of data that will be necessary to discriminate between stripping models.

To measure tidal stripping, it is necessary to eliminate the contribution of the shared group halo to the lensing signal around satellites. Any method to do this will introduce its own sources of error, which can be comparable in magnitude to shape noise. In the cluster regime, it is possible to obtain very accurate mass estimates for individual clusters, and so these errors can be minimized even for individual clusters. In the group regime, it is only possible to estimate group mass sufficiently well when multiple groups are stacked together, but the far greater numbers of groups make this feasible.

3.5 Optimal Methodology

Our tests of both the Mirror Method and Ensemble Method show that in ideal circumstances, they both successfully eliminate the groups' contribution to the lensing signals around satellites. In this scenario, the Mirror Method is less biased, but suffers from a greater error due to shape noise - a result of the fact that it relies in the difference in signal between two points, causing the error to be increased by a factor of $\sqrt{2}$. The Ensemble Method causes errors to be contributed from the estimate of the average group mass, but the total errors still tend to be less than the errors from the Mirror Method.

When comparing the "No Stripping" and "Stripping" models, we see that the difference between the two models is larger when the Ensemble Method is used. This is due to the fact that the Mirror Method, by subtracting out the signal from around sample points, also subtracts out a portion of the lensing signal around satellites. In particular, for a point-mass satellite a distance R from the centre of its group, the Mirror Method will detect zero signal for it on average for sources at annuli of radius greater than $2R$ (the distance from the satellite to the sample point). The satellites which are found closest to group centres tend to be the ones which have undergone the most stripping, but these are also the satellites which lose the largest amount of their own lensing signals when the Mirror Method is used. This suppresses the difference between the "No Stripping" and "Stripping" models.

Although neither method works perfectly when centring errors are present, the Ensemble Method shows somewhat less sensitivity to centring errors than does the Mirror Method. This difference is most significant for centring errors of $\sigma = r_\mathrm{s}$. Note that we expect to be able to quantify centring errors through the George et al. (2012) method of fitting the lensing signal around group centres with an NFW profile convolved with centring error (see the discussion in Section 3.3.1.3), but it is still useful to minimize the expected offset due to centring errors.

Overall, the Ensemble Method is preferable to the Mirror Method. It presents a better signal-to-noise in the difference between the expected signals for stripped and unstripped satellites, and it is less vulnerable to centring errors than the Mirror Method.

Other methods, such as a maximum-likelihood analysis, which work similarly to the Ensemble Method, will likely have a similar signal-to-noise to what we have calculated here.

3.6 Prospects for Stripping Detections

A detection of tidal stripping with either of the methods we have proposed will first require the issue of centring errors to be addressed. If they can be addressed and corrected for (e.g., by using the method of George et al. (2012), discussed in Section 3.3.1.3), the Ensemble Method then provides the better S/N. By using the Ensemble Method and comparing the S/N in the difference between the Stripping and No Stripping models, we can estimate how much data will be needed in different group mass regimes in order to differentiate between the models. Table 3.1 lists our predicted S/N values for a measurement using the overlapping region of the CFHTLenS and GAMA-II surveys, as well as for other future surveys. We list S/N values for both the difference between the "No Stripping" and "Stripping" models, and the difference between the "Matched Field" dataset and the "Stripping" model. Of these two, the latter comparison is what we will measure in observational data, but it may be influenced by systematic errors in the application of the Ensemble Method. The former comparison is less likely to be influenced by systematic errors, as we used the same fields and realization of noise for both the "No Stripping" and "Stripping" models. As such, it provides a more realistic prediction for what we might see with observational data.

Of the three mass regimes tested, we see the highest S/N, 1.88, in the group mass bin of 10^{13} $M_\odot < M_{tot} < 10^{14}$ $M_\odot$. Although this does not quite reach the 2σ threshold for a detection, it is still worth making this measurement for various reasons:

- We do not apply any weighting scheme to our lenses or sources. An optimal weighting scheme could serve to boost the S/N.

- When all three mass bins are combined together, the predicted S/N rises to 2.86. This will allow us to detect the presence or absence of stripping, but not the group mass regimes in which it is taking place.

- If stripping does occur and is stronger than predicted by our models (see Equation (2.5)), a detection will be more likely.

- Even if no 2σ detection can be made from the CFHTLens+GAMA-II dataset, the results of this measurement can be combined with future measurements to potentially add significance to those results.

Our predicted significance can be improved upon if data from other surveys is combined with the CFHTLenS+GAMA-II dataset. Of note, KiDS (Verdoes Kleijn et al., 2011) will overlap the GAMA-I survey in 150 deg.[2] when it is complete, and we estimate that

TABLE 3.2: Predicted detection S/N for measurements in various surveys, assuming the Ensemble Method is used, and using the comparison of our "No Stripping" and "Stripping" models. "C+G" is the combination of the CFHTLenS and GAMA-II surveys; "K+G" is KiDS and GAMA-I; "C+K+G" is CFHTLenS; KiDS, GAMA-I, and GAMA-II; "H+L*" is HSC and LOWZ; and "E+L*" is Euclid and LOWZ. *These columns give estimates for proposed surveys, and may not represent the surveys in their final forms.

	Predicted S/N$_{NS-S}$				
$\log M$	C+G	K+G	C+K+G	H+L*	E+L*
12–13	1.43	1.63	2.17	~ 8	~ 13
13–14	1.88	2.14	2.85	~ 11	~ 16
14–15	1.61	1.84	2.44	~ 9	~ 14

it will contain an effective 8 sources per arcmin.^{2}. Assuming that the overlap between KiDS and GAMA-I will be 80% unmasked, this results in a dataset that is $\sim 1.3\times$ larger than CFHTLenS+GAMA-II. Table 3.2 shows the predicted significances for the three mass regimes we have tested, assuming the KiDS+GAMA-I dataset is used alone, and also combining it with the CFHTLenS+GAMA-II dataset. KiDS+GAMA-I alone is somewhat better than CFHTLenS+GAMA-II, and the combination of the two datasets has a $> 50\%$ chance of a 2σ detection in each mass bin, if stripping is occurring at the strength we have modelled.

We also show in Table 3.2 the estimated S/N for these mass bins for potential future large-scale surveys. To estimate this, we use the GAMA-II S/N estimates and a calculated scaling factor which depends on the survey size, source density, and the redshift distributions of lenses and sources. We first consider a combined dataset of the anticipated Hyper-Suprime Cam (Takada, 2010, hereafter HSC) survey and the Next Generation Canada-France-Hawaii Telescope (Cote et al., 2012, hereafter ngCFHT) proposed LOWZ survey. HSC is planned to cover $\sim 1,400$ deg^2 ($\sim 1,000$ deg^2 after masking), with $20\,\mathrm{min}$ exposures in the i-band for shape data, which we project will result in ~ 29 shapes per arcmin^2, or an effective ~ 13 after weighting. The LOWZ survey is projected to gather spectra for all galaxies in a $1,000$ deg^2 field, whose location is yet to be determined, but may overlap HSC. This survey will aim for near-100% completeness to a redshift of $z < 0.15$ and a depth of $i' < 22$, resulting in a conservative project surface density of ~ 700 galaxies per deg^2. This would allow us a much higher significance $(8-11\sigma)$ detection of tidal stripping.

We next consider a projected dataset for the Euclid (Laureijs et al., 2011) survey. Euclid is planned to cover $\sim 15,000$ deg^2 ($\sim 11,000$ deg^2 after masking), with a projected effective ~ 30 shapes per arcmin^2. Euclid also plans to gather spectroscopic redshifts for ~ 3000 galaxies per deg^2 in the redshift range $0.7 < z < 2.1$. However, given the high redshift of this sample and the fact that the source sample for Euclid is expected

to peak at $z \sim 0.9$, the combined dataset will present us with relatively few lens-source pairs to work with. This is made worse by the fact that the survey is aimed at gathering spectra for luminous red galaxies (LRGs), which are mostly central galaxies, and by the fact that the low completeness of this survey will make identifying groups difficult. As such, Euclid alone will not provide a good dataset for the type of analysis presented in this chapter. However, if it ends up overlapping the LOWZ survey, the spectra from that survey can be used for such an analysis, which would give even higher significance results than if LOWZ were combined with HSC ($\sim 13 - 16\sigma$).

In conclusion, we will soon be able to use weak gravitational lensing to measure tidal stripping even within low-mass galaxy groups. Planned surveys over the next two decades will provide us with a wealth of data to investigate even more subtle factors involved in tidal stripping, but we will need to get a better handle on systematic errors in order to take full advantage of these surveys. We will hopefully soon be able to gain a better understanding of tidal stripping, which will allow us insight into its role in the evolution of galaxies within group environments.

Chapter 4

Conclusion

In this chapter we conclude. In Section 4.1, we discuss the results of our analysis, and we further explore the possible implications of these results in Section 4.2. In Section 4.3, we discuss prospects for future surveys and analysis, and we present concluding remarks in Section 4.4.

4.1 Summary of Results

Previous lensing analyses of the environmental dependence of satellite halo masses (Mandelbaum et al., 2006b, van Uitert et al., 2011) have revealed the difficulty of detecting such an effect in samples where the satellites are predominantly expected to lie in groups. The analysis here improves on previous work by using the much deeper data provided by the CFHTLenS sample to better constrain the lensing signal around low-mass satellite galaxies in high-density environments.

Using photometric redshifts we divide galaxies in high-density and low-density environment subsamples that are matched in stellar mass. We have found a significant difference in their halo masses. Our analysis shows a highly significant (4.1σ) rejection of the simulated "No Stripping" model, and a significant (2.9σ) rejection of the simple "null hypothesis" that there is no difference in the halo properties of HDE and LDE galaxies, for galaxies in a broad range of group masses. This difference is most likely due to tidal stripping of dark matter, and if so, this analysis represents the first detection of tidal stripping in a selection of galaxies that do not all reside within galaxy clusters.

The mean ratio of fitted mass for the high-density environment sample to that of the low-density environment sample is $\sim 0.65 \pm 0.12$. Since the HDE galaxy sample consists of only $\sim 60\%$ satellites, the retained mass fraction for a pure satellite sample would

be considerably lower: $\sim 0.41 \pm 0.19$. This compares favorably with the retained mass fractions of $\sim 20 - 40\%$ found by Natarajan et al. (2009) in the cluster regime. We can alternatively model this as the HDE satellites being tidally stripped at a typical radius of $r_{\mathrm{tidal}}/r_{200} = 0.26 \pm 0.14$. This corresponds to a typical tidal radius of 40 ± 21 kpc and a retained mass fraction of 0.43 ± 0.18 for a satellite galaxy with $M = 5.9 \times 10^{11} M_{\odot}$ and $c = 8.5$.

We argue that these results are unlikely to be due to systematic errors in our methodology; there are various possible systematics which we analyse, but only one possibility would bias us in the direction of a false positive detection. In principle a relative bias in the stellar mass estimates between red and blue galaxies could result in a measure such as what we observe, but this would require that the stellar masses of red galaxies are overestimated relative to blue galaxies and that the relative fractions of red and blue galaxies differ greatly between our HDE and LDE samples. As we show, neither of these is the case - the stellar masses of blue galaxies are in fact more likely to be overestimated relative to red galaxies, while the relative red and blue fractions differ by no more than 10% in our HDE and LDE samples. As such, this effect would be expected to only cause a slight bias away from a false positive detection.

Additionally, it is possible that some of our assumptions regarding the fraction and distribution of satellites within groups could bias us toward or away from a false detection. As we show though, most possible variations in these parameters would in fact increase the significance of our detection, as would properly including the two-halo term in our analysis. The only variation in parameters that would decrease the significance of our detection is if the actual fraction of galaxies in the HDE sample which are satellites were significantly lower than we predicted from simulations. While this is possible, we have no evidence to indicate it might be the case. Even if this is the case, for a satellite fraction of 0.4, the significance of our detection would only fall to $\sim 2.1\sigma$. A lower satellite fraction could further decrease the significance of our result, below the threshold of 2σ, but this is unlikely, particularly when one factors in that a proper treatment of the two-halo term would likely raise the significance of our detection. As such, this detection appears to be very robust.

Further work will be necessary to confirm these results, and to analyse the dependence of stripping on both group mass and on the locations of satellites within groups. We have begun preliminary analysis of the SDSS DR8 dataset, which we expect to have similar statistical power to the CFHTLenS, to determine whether or not it supports our conclusions, but more works needs to be done before firm conclusions can be made.

In our analyses of methods that will be usable if spectroscopic redshift data becomes available, we have shown that for analysis of the lensing signals of satellite galaxies,

the Ensemble Method (see Section 3.2.2) successfully subtracts out the contributions of these satellites' host groups to their lensing signal. This method performs better overall than the Mirror Method (see Section 3.2.1).

We have shown here that errors in identifying the centres of group haloes have a significant impact on the analysis of the lensing signals around satellites with these methods. The contribution of these centring errors to the lensing signals around satellites is typically larger than the effect of tidal stripping on these signals. It is thus necessary to properly estimate the amount of centring error present in a sample before an assessment can be made of the presence or absence of tidal stripping.

If centring errors in the dataset can be measured, upcoming data from the GAMA-II survey, when combined with the CFHTLenS dataset, may be able to detect tidal stripping within groups of mass 10^{13} $M_\odot < M_{\rm tot} < 10^{14}$ $M_\odot$ to 2σ significance, depending on the strength of stripping in reality, as well as the scatter of the observational data. Data from KiDS and GAMA-I can be used to improve the significance of this measurement, and to also potentially detect stripping in lower-mass groups.

4.2 Implications of Results

While previous analyses of tidal stripping in galaxy groups failed to detect the presence of tidal stripping (Mandelbaum et al., 2006b, van Uitert et al., 2011), they did not rule it out either, and so this result is not, in fact, surprising. N-body simulations have predicted that tidal stripping should occur in groups and clusters of all masses (Hayashi et al., 2004, Kazantzidis et al., 2004, Springel et al., 2008), and the difficulty prior to this has simply been in finding evidence for this effect on group scales. There are, however, two surprising aspects to our results: First, the observed stripping is even stronger (at the 1.8σ significance level) than the simulated "Stripping" model; and second, our HDE and LDE samples contain very similar fractions of red and blue galaxies, and yet this difference in their one-halo masses is nevertheless quite significant. We discuss these implications in Section 4.2.1 and Section 4.2.2 respectively, and in Section 4.2.3 we discuss the implications of our results on modified gravity theories.

4.2.1 Strength of Tidal Interactions

The fact that our detection is stronger than that predicted by the "Stripping" model, which was based on N-body simulations performed by Gao et al. (2004), may indicate that this model underestimates the amount of stripping that occurs in reality, particularly on group scales. The evidence that this may be the case is not strong (1.8σ), and

95

so it merits further investigation before any firm conclusions may be drawn, but the possible explanations for this are intriguing. Notably, if dark matter haloes are more easily disrupted in galaxy groups than is currently predicted in N-body simulations, this could have bearing on the "missing substructure" problem, previously referred to in Section 1.1.4.2.

Consider how structure formation might occur if dark matter more readily experienced tidal stripping, whatever the physical reason for this. As a group-scale halo collapses, and smaller dark matter haloes join to form a group, tidal stripping could disrupt or destroy some fraction of the haloes. This effect would not be limited to the least-massive haloes; as long as there are more massive haloes which could strip away dark matter, a halo could be disrupted and prevented from forming a galaxy. Unlike considerations of warm dark matter, tidal interactions readily explain why there might be missing substructure at a large range of mass scales; some structures by chance would avoid close interactions with more massive haloes (including the haloes at the centres of groups) and survive to produce galaxies. In addition to the effects on dark matter haloes, tidal interactions would also have the effect of stripping away gas from less-massive proto-galaxies, which would also aid in preventing star formation. However, more massive haloes would still be expected to be more tightly-bound than less-massive structure, and so one would expect the reduction in substructure to be most extreme among the least massive structures, which does not easily fit with comparisons of the Local Group to dark matter simulations.

This possibility also raises the question of what physical process might cause haloes to be more readily stripped. Warm dark matter provides one possible answer, as supported by the simulations of Colín et al. (2000), who found that in a warm dark matter model, roughly twice as many satellites were destroyed by tidal interactions as in a cold dark matter model, which they hypothesize is due to the lower concentrations of satellite haloes in the warm dark matter model. This lower concentration would also result in a shallower potential well for the subhaloes, making the particles more susceptible to escape after tidal shocks. However, N-body simulations of warm dark matter are not always better than cold-dark-matter simulations at predicting the abundance of substructure in the Local Group. Mixed state dark matter, which contains multiple species of particles, some of which are warm and some of which are cold (Davis et al., 1992, Borgani et al., 1996, Boyarsky et al., 2009b,a), may provide a better solution, but further analysis will be necessary to determine the full implications of this scenario, and if it would better explain the amount of tidal stripping observed in our analysis here.

4.2.2 Colour-Dependence of Stripping

One interesting aspect of our results here is the fact that, while the red and blue fractions differ by no more than 10% between our HDE and LDE samples, we nevertheless show a very strong difference in the one-halo mass between the two samples. Consider what we would expect to observe if all red galaxies had experienced tidal stripping, and no blue galaxies had. We would expect to see a difference between our HDE and LDE samples roughly of magnitude $f_{\mathrm{massstripped}}\,(f_{\mathrm{red,HDE}} - f_{\mathrm{red,LDE}})$, where $f_{\mathrm{massstripped}}$ is the fraction of mass typically lost in tidal stripping, and $f_{\mathrm{red,HDE}}$ and $f_{\mathrm{red,LDE}}$ are the fractions of red galaxies in the HDE and LDE samples respectively. If we assume that $f_{\mathrm{red,HDE}} - f_{\mathrm{red,LDE}} \approx 0.1$ and $f_{\mathrm{massstripped}} \approx 0.6$, then we would expect the difference between one-halo masses measured in the HDE and LDE samples to be only $\sim 6\%$, a possibility which we rule out at 2.4σ significance.

If we rule out the possibility that all red galaxies are stripped, but no blue galaxies are, at least one of the following possibilities must be true:

1. Red galaxies in high-density environments are more likely to be stripped than red galaxies in low-density environments

2. Blue galaxies in high-density environments are more likely to be stripped than blue galaxies in low-density environments

3. Some factor other than tidal stripping, such as a difference in formation history, causes an environment-dependent difference in stellar mass for galaxies in haloes of similar total mass.

If possibility (1) is true, this would imply that some factor other than tidal stripping causes galaxies to become red, such as mergers, ram pressure stripping, supernova feedback, or AGN feedback. Ram pressure stripping is strongest in clusters, but it may still play a role in group scales. A history of mergers may be more likely, as the lower relative velocities in low-density regions will allow mergers. However, any region that experiences a significant frequency of galaxy mergers would also be expected to experience frequent close interactions between galaxies, and thus tidal stripping. Supernova and AGN feedback are not likely to have more of an effect in a group environment, and we observe very few red galaxies in the field, where these effects would dominate, so this would imply that only a small fraction of red galaxies in groups and clusters are red due to feedback.

If possibility (2) is true, then this would imply that tidal stripping does not immediately or always lead to a transformation from blue galaxies into red. As dark matter haloes

have a significantly larger spatial extent than hot gas, it is possible that some fraction of stripping events affect dark matter haloes but not gas. This would result in a number of blue galaxies in high-density environments which have stripped dark matter haloes, which could explain our results. Additionally, it is possible that, even when gas is stripped from blue galaxies, it takes a significant amount of time before they transform into red galaxies. There is independent evidence, for instance from Taranu et al. (2012) and Wetzel et al. (2013), that the transformation of blue galaxies into red galaxies does not occur until $\sim$ 2–3 Gyr after a galaxy's orbit passes pericentre. Our results thus present indirect evidence that this may in fact be the case, but further analysis of the environmental dependence of the dark masses of blue galaxies will be necessary before a firm conclusion might be drawn.

Possibility (3) above implies that the difference we observe in one-halo masses is primarily due to a difference in formation history. Structures within denser large-scale environments would have an initially higher δ, and thus would collapse earlier. This would not directly impact the fraction of baryons within a halo, but if galaxies form earlier, they will have had more time to form stars, increasing their stellar masses while their dark matter haloes slowly accrete mass. If the rate of dark matter accretion is sufficiently slow, this could be seen to manifest as an apparent effect where galaxies of similar stellar mass will have less-massive dark matter haloes if they reside within a high-density large-scale region. The earlier collapse time, along with the increased background density, will also result in the galaxies that have higher mean densities at a fixed halo mass compared to galaxies which form in lower-density regions. Since the star-formation rate does not scale linearly with density, the resultant stellar masses of these galaxies could end up higher than galaxies which formed in less-dense regions.

Our data cannot rule this possibility out at present, but this explanation is currently disfavoured by the data we do have. As can be seen in Fig. 2.10 and Table 2.4, the halo masses are actually higher in the HDE sample than in the LDE sample for the two most massive stellar mass bins. While this does not rise to the 2σ threshold for significance, it is inconsistent with what would be expected if a difference in formation history were the primary factor behind our results. If this were the only effect in play, it would decrease mass-to-light ratios for galaxies of all stellar masses in high-density regions. However, tidal stripping would be expected to decrease mass-to-light ratios for less-massive galaxies in these regions, while increasing it for the most massive galaxies, as the dark mass gets stripped away from less massive galaxies and transferred to more massive galaxies. As such, tidal stripping better fits our results than does a difference in formation history.

Possibilities (1) and (2), that red and blue galaxies, respectively, are preferentially stripped in high-density environments, remain possible. These possibilities can be readily investigated once further data becomes available, through comparing samples of HDE and LDE red and blue galaxies. This will allow us to conclude how much of a role tidal stripping plays in the transformation of blue galaxies into red galaxies.

4.2.3 Modified Gravity Theories

Systems such as the Bullet Cluster (Clowe et al., 2004), in which weak lensing evidence shows that a significant amount of dark matter has been separated from the baryonic mass of the clusters, have provided strong evidence in favour of dissipationless dark matter over the alternative hypotheses of modified gravity theories. Nevertheless, work is ongoing to formulate modified gravity theories which might be able to account for the lensing signals observed in these systems. As such, it merits analysis of how the results presented in this thesis, which were based on the assumption that dark matter exists, might be interpreted in the alternative paradigm of modified gravity.

There are two possible manners in which our results might be explained under a modified gravity theory: First, since we match galaxies by stellar mass, and measure a difference in lensing signal, which is related to the total mass of galaxies, the difference might be due to an actual difference in the total masses of these galaxies. Since there is no dark matter to explain the difference, and stellar mass is matched between our samples, this difference must be in gas mass. Second, it is possible that the physics of lensing differs depending on the environment, for instance if the strength of gravitational interactions depends on the local gravitational "potential" in addition to its gradient[1], as in "chameleon" models of modified gravity (see Jain and Khoury, 2010), in which gravity is weaker in regions of high-density.

We first consider whether or not a reduction in gas mass in HDE galaxies might be sufficient to explain our measurements in a modified gravity paradigm. Tidal stripping would be expected to remove gas from stripped galaxies, but the question is whether or not a sufficient amount of gas would be removed to account for the observed reduction in mass of our HDE sample. Typical gas mass fractions in young star-forming galaxies are typically $\sim 0.6 - 0.8$, and so to match our calculated retained mass fraction of $\sim 40\%$, nearly all the gas in all satellite galaxies in our sample would have had to be stripped away. However, the error bars in our retained mass fraction are sufficiently large that a retained mass fraction of ~ 0.75 is within the bounds of our error bars. If this were in fact the case, it would require only $\sim 35\%$ of the gas mass in satellites to be

---

[1] Of course, if the strength of interactions behaves in this manner, it cannot be simply characterized as a potential. We use this term only in analogy with classical gravity.

tidally stripped away. This is a reasonable value, and so we cannot rule out a modified gravity explanation from our data at present. However, if future data narrows the error bars on our data without significantly increasing the mean retained mass fraction, this explanation may yet be ruled out.

Alternatively, our results could be explained if gravity were weaker in regions of high density, and thus deep gravitational potential. This general behaviour is consistent with the predictions of "chameleon" models, but the full details of lensing in this regime require calculations and simulations which are beyond the scope of this thesis. Other models of modified gravity may also be consistent with these results, but they will similarly require significant amounts of analysis beyond the scope of this thesis.

4.3   Outlook

In this section we briefly discuss future surveys and techniques, as well as their implications on future measurements. In Section 4.3.1 we discuss upcoming and potential surveys, and how they will aid analysis, and in Section 4.3.2 we discuss alternative lensing techniques which may also provide avenues to analyse dark matter structure within groups in the future.

4.3.1   Future Surveys

As we discussed in Section 4.2, our data implies two very interesting possibilities with regards to tidal stripping: that it may be stronger than simulations have predicted, and that a significant fraction of blue galaxies have likely been stripped. Both of these prospects will require additional data before we might reach a statistically-significant conclusion about either one, and fortunately such data will soon be available.

In the present, there are two notable datasets of shape data and photometry which may be useful useful in our analysis: The SDSS, and the CFHT Stripe 82 survey (Leauthaud et al., 2012b, hereafter CS82). The SDSS has previously been discussed in this thesis, and the data from it is already being analysed. The CS82 is a survey of an equatorial region of the SDSS which has been well-sampled by many surveys. The imaging data provided by this survey gives an effective source density of ~ 10 sources/arcmin^2, and the survey covers 170 deg^2, comparable to the CFHTLenS. As such, data from this survey could readily be analysed and added to our analysis. The addition of this survey would provide sufficient data to limit our analysis to only blue galaxies, for instance, allowing us to determine if tidal stripping can be detected among this subsample. While

the CS82 data are not yet publicly available, a collaboration with an interested party would allow for analysis of the data.

There are additionally many notable lensing surveys which are expected to provide data in the coming years. In the short term, the most notable is KiDS (de Jong et al., 2012), which will provide 1500 deg^2 of 9-band photometry 2 magnitudes deeper than the SDSS when complete, with an estimated 8 sources/arcmin^2. It will also overlap with the spectroscopy of the GAMA-I survey (Driver et al., 2011) in 150 deg^2, allowing analysis using the methods we proposed for measuring tidal stripping in spectroscopically-identified galaxy groups. This analysis will be aided by the data available from the partially-completed GAMA-II survey, which overlaps with the W1 field of the CFHTLenS and will give us a second sample of shape and spectroscopy comparable to the overlap between KiDS and GAMA-I. We project that these combined datasets will allow us to investigate in which group masses tidal stripping occurs, which will hopefully provide insight into how much of a role tidal stripping plays in the changing mass-to-light ratios of galaxies in groups and clusters.

As we have shown in this thesis, both spectroscopic and photometric redshift data can be used to provide information on the local environments of galaxies. Photometric redshift data has the advantage that it is much easier to acquire than spectroscopic redshift data, and for many lensing purposes, its larger errors are an acceptable trade-off for the greater amount of data, particularly as weak lensing errors are typically dominated by shape noise. However, if we wish to analyse how lensing signals vary with group mass, the errors that photometric redshifts introduce into assigning group membership preclude accurate group mass estimates. As such, spectroscopic surveys are necessary for detailed analysis of the effects of tidal stripping within galaxy groups. Although these surveys are expensive in terms of telescope time, they can provide key insights into the behaviour of dark matter in structures more comparable to the Local Group. This will allow us to use weak lensing to test the predictions of the LCDM paradigm on relatively small scales and determine whether or not it needs to be modified to properly account for the distribution of dark matter within galaxy groups.

Further in the future, planned surveys will provide us with an abundance of new lensing data to analyse. The Dark Energy Survey (DES), currently running, plans to image a total of 5,000 deg^2 of the sky to $i \sim 24$, and is planned to be completed some time in 2018. After this, the Euclid telescope is planned to be launched in 2020 for a six-year mission to image 15,000 deg^2 of the sky to $r \sim 24.5$. Finally, the Large Synoptic Survey Telescope (LSST) plans to image 20,000 deg^2 of the sky to $r \sim 24.5$ over a ten-year period, starting in 2019-2020 if funding is secured. The amount of data available in

these surveys will greatly surpass the needs of the science goals discussed here, allowing us to probe even more subtle aspects of dark matter haloes than discussed in this thesis.

4.3.2 Other Lensing Techniques

In addition to shear measurements from weak gravitational lensing, there are two other avenues of analysis that are currently being researched. Shear can be considered the first-order distortion of background images due to galaxies, but it is also possible to use magnification (the zeroth-moment) and flexion (the second-order moment) to investigate dark matter distributions. We will briefly discuss both of these prospects in this section.

Gravitational lensing is predicted to magnify the images of all sources in the background of a lens. Measuring this effect has traditionally been more difficult than shear, as the expectation value for luminosity is non-zero. It is, however, possible to estimate magnification through a couple of methods. One method, as recently used by Hildebrandt et al. (2013) to estimate the masses of submillimetre galaxies, involves measuring the cross-correlation of lens and source positions, and using the shape of this function to estimate magnification, and thus lens mass. This technique is particularly useful at high redshifts ($z \gtrsim 1$), where galaxies are too faint for shear to be accurately measured.

Alternatively, magnification can be directly measured if the intrinsic luminosity of a galaxy can be predicted. For instance, Huff and Graves (2011) propose the method of a "photometric fundamental plane." Using a galaxy's light concentration as a proxy for its velocity dispersion, and combining this with surface brightness allows for an estimate of its intrinsic effective radius. This can then be compared with its measured effective radius to estimate the magnification of a galaxy. This technique is limited to elliptical galaxies, which are the only galaxies observed to lie on this fundamental plane relation, but it is nevertheless projected to attain S/N $\sim 50\%$ as large as shear measurements. As it is an independent measurement from shear, it could be used to increase the S/N of weak lensing measurements by a factor of $\sim 25\%$.

Additionally, flexion, the second-order component to distortion from weak gravitational lensing, seen as a curvature of source images, can provide additional data on dark matter halo distributions (Goldberg and Bacon, 2005, Bacon et al., 2006). Flexion is only apparent in higher-mass regions, and most galaxies have little intrinsic flexion, whatever their orientation of the sky. As such, noise in flexion measurements is dominated by pixel and read noise, and typically only high-significance measurements of flexion can be used for analysis. However, when these instances of flexion are detected, they in turn provide high-significance information about the mass distributions of lens systems.

While techniques for analysing magnification and flexion are less-refined than analysis of shear, they both provide potential to provide additional information to the mass profiles of dark matter haloes. In principle, a combination of these with shear will allow for the most accurate measurements of dark mass distributions, but this will require significant amounts of further work to test and implement.

4.4 Concluding Remarks

In this thesis we have presented evidence to support the hypothesis that tidal stripping occurs in galaxy groups. Further investigation will be needed to determine the typical extent of stripping, which will be possible in current and upcoming surveys. The methods we have proposed for measuring tidal stripping when spectroscopic redshifts are available will potentially allow us to determine the group mass regimes in which tidal stripping occurs.

These results will help us put together a full picture of group and cluster formation. We will soon be able to answer the question of what role tidal stripping plays in group formation, and if it can be responsible for the rising mass-to-light ratios and fraction of red galaxies within galaxy groups. We may even gain insight into the nature of dark matter through comparisons with N-body simulations, or provide further tests of modified gravity theories.

Bibliography

M. G. Abadi, B. Moore, and R. G. Bower. Ram pressure stripping of spiral galaxies in clusters. *MNRAS*, 308:947–954, October 1999. doi: 10.1046/j.1365-8711.1999.02715.x.

F. B. Abdalla, M. Banerji, O. Lahav, and V. Rashkov. A comparison of six photometric redshift methods applied to 1.5 million luminous red galaxies. *MNRAS*, 417:1891–1903, November 2011. doi: 10.1111/j.1365-2966.2011.19375.x.

Z. Ahmed, D. S. Akerib, S. Arrenberg, *et al.* Results from a Low-Energy Analysis of the CDMS II Germanium Data. *Physical Review Letters*, 106(13):131302, April 2011. doi: 10.1103/PhysRevLett.106.131302.

H. Aihara, C. Allende Prieto, D. An, *et al.* The Eighth Data Release of the Sloan Digital Sky Survey: First Data from SDSS-III. *ApJS*, 193:29, April 2011. doi: 10. 1088/0067-0049/193/2/29.

S. M. K. Alam, J. S. Bullock, and D. H. Weinberg. Dark Matter Properties and Halo Central Densities. *ApJ*, 572:34–40, June 2002. doi: 10.1086/340190.

C. Alcock, R. A. Allsman, D. R. Alves, *et al.* The MACHO Project: Microlensing Results from 5.7 Years of Large Magellanic Cloud Observations. *ApJ*, 542:281–307, October 2000. doi: 10.1086/309512.

J. Angle, E. Aprile, F. Arneodo, *et al.* Search for Light Dark Matter in XENON10 Data. *Physical Review Letters*, 107(5):051301, July 2011. doi: 10.1103/PhysRevLett. 107.051301.

E. Aprile, M. Alfonsi, K. Arisaka, *et al.* Dark Matter Results from 225 Live Days of XENON100 Data. *Physical Review Letters*, 109(18):181301, November 2012. doi: 10.1103/PhysRevLett.109.181301.

V. Avila-Reese, P. Colín, O. Valenzuela, E. D'Onghia, and C. Firmani. Formation and Structure of Halos in a Warm Dark Matter Cosmology. *ApJ*, 559:516–530, October 2001. doi: 10.1086/322411.

D. J. Bacon, D. M. Goldberg, B. T. P. Rowe, and A. N. Taylor. Weak gravitational flexion. *MNRAS*, 365:414–428, January 2006. doi: 10.1111/j.1365-2966.2005.09624.x.

I. K. Baldry. Hubble's galaxy nomenclature. *Astronomy and Geophysics*, 49(5):050000–5, October 2008. doi: 10.1111/j.1468-4004.2008.49525.x.

M. L. Balogh, S. L. Morris, H. K. C. Yee, R. G. Carlberg, and E. Ellingson. Differential Galaxy Evolution in Cluster and Field Galaxies at z~0.3. *ApJ*, 527:54–79, December 1999. doi: 10.1086/308056.

M. L. Balogh, I. K. Baldry, R. Nichol, *et al.* The Bimodal Galaxy Color Distribution: Dependence on Luminosity and Environment. *ApJL*, 615:L101–L104, November 2004. doi: 10.1086/426079.

Michael L. Balogh and Simon L. Morris. Hα photometry of Abell 2390. *MNRAS*, 318 (3):703–714, 2000. ISSN 1365-2966. doi: 10.1046/j.1365-8711.2000.03826.x.

E. A. Baltz, P. Marshall, and M. Oguri. Analytic models of plausible gravitational lens potentials. *JCAP*, 1:15, January 2009. doi: 10.1088/1475-7516/2009/01/015.

N. Benítez. Bayesian Photometric Redshift Estimation. *ApJ*, 536:571–583, June 2000. doi: 10.1086/308947.

R. Bernabei, P. Belli, F. Cappella, *et al.* First results from DAMA/LIBRA and the combined results with DAMA/NaI. *European Physical Journal C*, 56:333, August 2008. doi: 10.1140/epjc/s10052-008-0662-y.

R. Bernabei, P. Belli, F. Cappella, *et al.* New results from DAMA/LIBRA. *European Physical Journal C*, 67:39–49, May 2010. doi: 10.1140/epjc/s10052-010-1303-9.

F. Bernardeau, L. van Waerbeke, and Y. Mellier. Weak lensing statistics as a probe of Ω and power spectrum. *A&A*, 322:1–18, June 1997.

G. M. Bernstein and M. Jarvis. Shapes and Shears, Stars and Smears: Optimal Measurements for Weak Lensing. *AJ*, 123:583–618, February 2002. doi: 10.1086/338085.

E. Bertschinger. Path integral methods for primordial density perturbations - Sampling of constrained Gaussian random fields. *ApJL*, 323:L103–L106, December 1987. doi: 10.1086/185066.

R. Bielby, P. Hudelot, H. J. McCracken, *et al.* The WIRCam Deep Survey. I. Counts, colours, and mass-functions derived from near-infrared imaging in the CFHTLS deep fields. *A&A*, 545:A23, September 2012. doi: 10.1051/0004-6361/201118547.

J. Binney and S. Tremaine. *Galactic Dynamics*. Princeton University Press, 2008.

R. D. Blandford, A. B. Saust, T. G. Brainerd, and J. V. Villumsen. The distortion of distant galaxy images by large-scale structure. *MNRAS*, 251:600–627, August 1991.

M. R. Blanton and S. Roweis. K-Corrections and Filter Transformations in the Ultraviolet, Optical, and Near-Infrared. *AJ*, 133:734–754, February 2007. doi: 10.1086/510127.

P. Bode, J. P. Ostriker, and N. Turok. Halo Formation in Warm Dark Matter Models. *ApJ*, 556:93–107, July 2001. doi: 10.1086/321541.

I. A. Bond, A. Udalski, M. Jaroszyński, *et al.* OGLE 2003-BLG-235/MOA 2003-BLG-53: A Planetary Microlensing Event. *ApJL*, 606:L155–L158, May 2004. doi: 10.1086/420928.

S. Borgani, A. Masiero, and M. Yamaguchi. Light gravitinos as mixed dark matter. *Physics Letters B*, 386:189–197, February 1996. doi: 10.1016/0370-2693(96)00956-2.

O. Boulade, X. Charlot, P. Abbon, *et al.* MegaCam: the new Canada-France-Hawaii Telescope wide-field imaging camera. 4841:72–81, March 2003. doi: 10.1117/12.459890.

A. Boyarsky, J. Lesgourgues, O. Ruchayskiy, and M. Viel. Realistic Sterile Neutrino Dark Matter with KeV Mass does not Contradict Cosmological Bounds. *Physical Review Letters*, 102(20):201304, May 2009a. doi: 10.1103/PhysRevLett.102.201304.

A. Boyarsky, O. Ruchayskiy, and M. Shaposhnikov. The Role of Sterile Neutrinos in Cosmology and Astrophysics. *Annual Review of Nuclear and Particle Science*, 59: 191–214, November 2009b. doi: 10.1146/annurev.nucl.010909.083654.

T. G. Brainerd. Multiple Weak Deflections in Galaxy-Galaxy Lensing. *ApJ*, 713:603–614, April 2010. doi: 10.1088/0004-637X/713/1/603.

T. G. Brainerd, R. D. Blandford, and I. Smail. Weak Gravitational Lensing by Galaxies. *ApJ*, 466:623, August 1996. doi: 10.1086/177537.

J. Brinchmann, S. Charlot, S. D. M. White, *et al.* The physical properties of star-forming galaxies in the low-redshift Universe. *MNRAS*, 351:1151–1179, July 2004. doi: 10.1111/j.1365-2966.2004.07881.x.

J. M. Budzynski, S. E. Koposov, I. G. McCarthy, S. L. McGee, and V. Belokurov. The radial distribution of galaxies in groups and clusters. *MNRAS*, 423:104–121, June 2012. doi: 10.1111/j.1365-2966.2012.20663.x.

J. S. Bullock. Notes on the Missing Satellites Problem. *ArXiv e-prints*, September 2010.

H. Butcher and A. Oemler. The evolution of galaxies in clusters. V - A study of populations since Z approximately equal to 0.5. *ApJ*, 285:426–438, October 1984. doi: 10.1086/162519.

P. Capak, L. L. Cowie, E. M. Hu, *et al.* A Deep Wide-Field, Optical, and Near-Infrared Catalog of a Large Area around the Hubble Deep Field North. *AJ*, 127:180–198, January 2004. doi: 10.1086/380611.

CDMS Collaboration, R. Agnese, Z. Ahmed, *et al.* Dark Matter Search Results Using the Silicon Detectors of CDMS II. *ArXiv e-prints*, April 2013.

CDMS II Collaboration, Z. Ahmed, D. S. Akerib, *et al.* Dark Matter Search Results from the CDMS II Experiment. *Science*, 327:1619–, March 2010. doi: 10.1126/science. 1186112.

D. Clowe, A. Gonzalez, and M. Markevitch. Weak-Lensing Mass Reconstruction of the Interacting Cluster 1E 0657-558: Direct Evidence for the Existence of Dark Matter. *ApJ*, 604:596–603, April 2004. doi: 10.1086/381970.

D. Coe, A. Zitrin, M. Carrasco, *et al.* CLASH: Three Strongly Lensed Images of a Candidate z ∼ 11 Galaxy. *ApJ*, 762:32, January 2013. doi: 10.1088/0004-637X/762/ 1/32.

P. Colín, V. Avila-Reese, and O. Valenzuela. Substructure and Halo Density Profiles in a Warm Dark Matter Cosmology. *ApJ*, 542:622–630, October 2000. doi: 10.1086/ 317057.

Adrian A. Collister and Ofer Lahav. ANNz: estimating photometric redshifts using artificial neural networks. *Publ.Astron.Soc.Pac.*, 116:345–351, 2004.

C. Conroy, R. H. Wechsler, and A. V. Kravtsov. Modeling Luminosity-dependent Galaxy Clustering through Cosmic Time. *ApJ*, 647:201–214, August 2006. doi: 10.1086/ 503602.

P. Cote, N. Arimoto, M. L. Balogh, and *et al.* Feasibility study report for the next generation cfht. i. science. Technical report, ngCFHT Feasibility Study Science Team, 2012. URL http://casca.ca/wp-content/uploads/2013/04/ngCFHT_ Feasibility_Science.pdf.

J. Coupon, M. Kilbinger, H. J. McCracken, *et al.* Galaxy clustering in the CFHTLS-Wide: the changing relationship between galaxies and haloes since z 1.2. *A&A*, 542: A5, June 2012. doi: 10.1051/0004-6361/201117625.

P. Crane, R. Albrecht, C. Barbieri, *et al.* First results from the Faint Object Camera - Images of the gravitational lens system G2237 + 0305. *ApJL*, 369:L59–L61, March 1991. doi: 10.1086/185958.

Darren J. Croton, Volker Springel, Simon D. M. White, *et al.* The many lives of active galactic nuclei: cooling flows, black holes and the luminosities and colours of galaxies. *Mon.Not.Roy.Astron.Soc.*, 365:11–28, 2006.

M. Davis, F. J. Summers, and D. Schlegel. Large-scale structure in a universe with mixed hot and cold dark matter. *Nature*, 359:393–396, October 1992. doi: 10.1038/359393a0.

J. T. A. de Jong, G. A. Verdoes Kleijn, K. H. Kuijken, and E. A. Valentijn. The Kilo-Degree Survey. *Experimental Astronomy*, page 34, August 2012. doi: 10.1007/s10686-012-9306-1.

Gabriella De Lucia and Jeremy Blaizot. The hierarchical formation of the brightest cluster galaxies. *Monthly Notices of the Royal Astronomical Society*, 375(1):2–14, 2007. ISSN 1365-2966. doi: 10.1111/j.1365-2966.2006.11287.x. URL http://dx.doi.org/10.1111/j.1365-2966.2006.11287.x.

J. P. Dietrich, T. Erben, G. Lamer, *et al.* BLOX: the Bonn lensing, optical, and X-ray selected galaxy clusters. I. Cluster catalog construction. *A&A*, 470:821–834, August 2007. doi: 10.1051/0004-6361:20077281.

A. Dressler. Galaxy morphology in rich clusters - Implications for the formation and evolution of galaxies. *ApJ*, 236:351–365, March 1980. doi: 10.1086/157753.

M. Drewes. The Phenomenology of Right Handed Neutrinos. *ArXiv e-prints*, March 2013.

S. P. Driver, D. T. Hill, L. S. Kelvin, *et al.* Galaxy and Mass Assembly (GAMA): survey diagnostics and core data release. *MNRAS*, 413:971–995, May 2011. doi: 10.1111/j.1365-2966.2010.18188.x.

A. A. Dutton, F. C. van den Bosch, and A. Dekel. On the origin of the galaxy star-formation-rate sequence: evolution and scatter. *MNRAS*, 405:1690–1710, July 2010. doi: 10.1111/j.1365-2966.2010.16620.x.

F. W. Dyson, A. S. Eddington, and C. Davidson. A Determination of the Deflection of Light by the Sun's Gravitational Field, from Observations Made at the Total Eclipse of May 29, 1919. *Royal Society of London Philosophical Transactions Series A*, 220: 291–333, 1920. doi: 10.1098/rsta.1920.0009.

George Efstathiou, Carlos S. Frenk, Simon D. M. White, and Marc Davis. Gravitational clustering from scale-free initial conditions. *MNRAS*, 235:715–748, 1988.

T. Erben, H. Hildebrandt, M. Lerchster, *et al.* CARS: the CFHTLS-Archive-Research Survey. I. Five-band multi-colour data from 37 sq. deg. CFHTLS-wide observations. *A&A*, 493:1197–1222, January 2009. doi: 10.1051/0004-6361:200810426.

T. Erben, H. Hildebrandt, L. Miller, *et al.* CFHTLenS: the Canada-France-Hawaii Telescope Lensing Survey - imaging data and catalogue products. *MNRAS*, 433:2545–2563, August 2013. doi: 10.1093/mnras/stt928.

O. Fakhouri, C.-P. Ma, and M. Boylan-Kolchin. The merger rates and mass assembly histories of dark matter haloes in the two Millennium simulations. *MNRAS*, 406:2267–2278, August 2010. doi: 10.1111/j.1365-2966.2010.16859.x.

R. Feldmann, C. M. Carollo, C. Porciani, *et al.* The Zurich Extragalactic Bayesian Redshift Analyzer and its first application: COSMOS. *MNRAS*, 372:565–577, October 2006. doi: 10.1111/j.1365-2966.2006.10930.x.

J. Ford, H. Hildebrandt, L. Van Waerbeke, *et al.* Magnification by Galaxy Group Dark Matter Halos. *ApJ*, 754:143, August 2012. doi: 10.1088/0004-637X/754/2/143.

C. S. Frenk, S. D. M. White, M. Davis, and G. Efstathiou. The formation of dark halos in a universe dominated by cold dark matter. *ApJ*, 327:507–525, April 1988. doi: 10.1086/166213.

L. Gao, S. D. M. White, A. Jenkins, F. Stoehr, and V. Springel. The subhalo populations of λcdm dark haloes. *Monthly Notices of the Royal Astronomical Society*, 355(3):819–834, 2004. ISSN 1365-2966. doi: 10.1111/j.1365-2966.2004.08360.x. URL http://dx.doi.org/10.1111/j.1365-2966.2004.08360.x.

R. Gavazzi, T. Treu, J. D. Rhodes, *et al.* The Sloan Lens ACS Survey. IV. The Mass Density Profile of Early-Type Galaxies out to 100 Effective Radii. *ApJ*, 667:176–190, September 2007. doi: 10.1086/519237.

R. Genzel, L. J. Tacconi, J. Gracia-Carpio, *et al.* A study of the gas-star formation relation over cosmic time. *MNRAS*, 407:2091–2108, October 2010. doi: 10.1111/j.1365-2966.2010.16969.x.

M. R. George, A. Leauthaud, K. Bundy, *et al.* Galaxies in X-Ray Groups. II. A Weak Lensing Study of Halo Centering. *ApJ*, 757:2, September 2012. doi: 10.1088/0004-637X/757/1/2.

B. R. Gillis and M. J. Hudson. Group-finding with photometric redshifts: the photo-z probability peaks algorithm. *MNRAS*, 410:13–26, January 2011. doi: 10.1111/j.1365-2966.2010.17415.x.

B. R. Gillis, M. J. Hudson, T. Erben, *et al.* CFHTLenS: the environmental dependence of galaxy halo masses from weak lensing. *MNRAS*, 431:1439–1452, May 2013a. doi: 10.1093/mnras/stt274.

B. R. Gillis, M. J. Hudson, S. Hilbert, and J. Hartlap. Probing satellite haloes with weak gravitational lensing. *MNRAS*, 429:372–384, February 2013b. doi: 10.1093/mnras/sts341.

M. D. Gladders and H. K. C. Yee. A New Method For Galaxy Cluster Detection. I. The Algorithm. *AJ*, 120:2148–2162, October 2000. doi: 10.1086/301557.

O. Y. Gnedin, L. Hernquist, and J. P. Ostriker. Tidal Shocking by Extended Mass Distributions. *ApJ*, 514:109–118, March 1999. doi: 10.1086/306910.

D. M. Goldberg and D. J. Bacon. Galaxy-Galaxy Flexion: Weak Lensing to Second Order. *ApJ*, 619:741–748, February 2005. doi: 10.1086/426782.

F. Governato, A. Zolotov, A. Pontzen, *et al.* Cuspy no more: how outflows affect the central dark matter and baryon distribution in Λ cold dark matter galaxies. *MNRAS*, 422:1231–1240, May 2012. doi: 10.1111/j.1365-2966.2012.20696.x.

Q. Guo, S. White, C. Li, and M. Boylan-Kolchin. How do galaxies populate dark matter haloes? *MNRAS*, 404:1111–1120, May 2010. doi: 10.1111/j.1365-2966.2010.16341.x.

J. Guzik and U. Seljak. Virial masses of galactic haloes from galaxy-galaxy lensing: theoretical modelling and application to Sloan Digital Sky Survey data. *MNRAS*, 335:311–324, September 2002. doi: 10.1046/j.1365-8711.2002.05591.x.

T. Hamana, S. Miyazaki, N. Kashikawa, *et al.* Subaru Weak-Lensing Survey II: Multi-Object Spectroscopy and Cluster Masses. *PASJ*, 61:833–, August 2009.

E. Hayashi, J. F. Navarro, C. Power, *et al.* The inner structure of ΛCDM haloes - II. Halo mass profiles and low surface brightness galaxy rotation curves. *MNRAS*, 355:794–812, December 2004. doi: 10.1111/j.1365-2966.2004.08359.x.

L. Hernquist. An analytical model for spherical galaxies and bulges. *ApJ*, 356:359–364, June 1990. doi: 10.1086/168845.

C. Heymans, L. Van Waerbeke, L. Miller, *et al.* CFHTLenS: the Canada-France-Hawaii Telescope Lensing Survey. *MNRAS*, 427:146–166, November 2012. doi: 10.1111/j.1365-2966.2012.21952.x.

C. Heymans, E. Grocutt, A. Heavens, *et al.* CFHTLenS tomographic weak lensing cosmological parameter constraints: Mitigating the impact of intrinsic galaxy alignments. *MNRAS*, May 2013. doi: 10.1093/mnras/stt601.

S. Hilbert and S. D. M. White. Abundances, masses and weak-lensing mass profiles of galaxy clusters as a function of richness and luminosity in ΛCDM cosmologies. *MNRAS*, 404:486–501, May 2010. doi: 10.1111/j.1365-2966.2010.16310.x.

S. Hilbert, J. Hartlap, S. D. M. White, and P. Schneider. Ray-tracing through the Millennium Simulation: Born corrections and lens-lens coupling in cosmic shear and galaxy-galaxy lensing. *A&A*, 499:31–43, May 2009. doi: 10.1051/0004-6361/200811054.

H. Hildebrandt, S. Arnouts, P. Capak, *et al.* PHAT: PHoto-z Accuracy Testing. *A&A*, 523:A31, November 2010. doi: 10.1051/0004-6361/201014885.

H. Hildebrandt, T. Erben, K. Kuijken, *et al.* CFHTLenS: improving the quality of photometric redshifts with precision photometry. *MNRAS*, 421:2355–2367, April 2012. doi: 10.1111/j.1365-2966.2012.20468.x.

H. Hildebrandt, L. van Waerbeke, D. Scott, *et al.* Inferring the mass of submillimetre galaxies by exploiting their gravitational magnification of background galaxies. *MNRAS*, 429:3230–3237, March 2013. doi: 10.1093/mnras/sts585.

G. Hinshaw, D. Larson, E. Komatsu, *et al.* Nine-Year Wilkinson Microwave Anisotropy Probe (WMAP) Observations: Cosmological Parameter Results. *ArXiv e-prints*, December 2012.

H. Hoekstra, M. Franx, K. Kuijken, *et al.* Weak-Lensing Study of Low-Mass Galaxy Groups: Implications for Ω_m. *ApJL*, 548:L5–L8, February 2001. doi: 10.1086/318917.

H. Hoekstra, H. K. C. Yee, and M. D. Gladders. Properties of Galaxy Dark Matter Halos from Weak Lensing. *ApJ*, 606:67–77, May 2004. doi: 10.1086/382726.

M. J. Hudson, S. D. J. Gwyn, H. Dahle, and N. Kaiser. Galaxy-Galaxy Lensing in the Hubble Deep Field: The Halo Tully-Fisher Relation at Intermediate Redshift. *ApJ*, 503:531, August 1998. doi: 10.1086/306026.

E. M. Huff and G. J. Graves. Magnificent Magnification: Exploiting the Other Half of the Lensing Signal. *ArXiv e-prints*, November 2011.

O. Ilbert, P. Capak, M. Salvato, *et al.* COSMOS Photometric Redshifts with 30-bands for 2-deg2. *The Astrophysical Journal*, 690:1236–1249, September 2009.

O. Ilbert, M. Salvato, E. Le Floc'h, *et al.* Galaxy Stellar Mass Assembly Between $0.2 < z < 2$ from the S-COSMOS Survey. *ApJ*, 709:644–663, February 2010. doi: 10.1088/0004-637X/709/2/644.

B. Jain and J. Khoury. Cosmological tests of gravity. *Annals of Physics*, 325:1479–1516, July 2010. doi: 10.1016/j.aop.2010.04.002.

Y. P. Jing and Y. Suto. Triaxial Modeling of Halo Density Profiles with High-Resolution N-Body Simulations. *ApJ*, 574:538–553, August 2002. doi: 10.1086/341065.

D. E. Johnston, E. S. Sheldon, R. H. Wechsler, *et al.* Cross-correlation Weak Lensing of SDSS galaxy Clusters II: Cluster Density Profiles and the Mass–Richness Relation. *ArXiv e-prints*, September 2007.

N. Kaiser. Weak gravitational lensing of distant galaxies. *ApJ*, 388:272–286, April 1992. doi: 10.1086/171151.

G. Kauffmann, S. D. M. White, and B. Guiderdoni. The Formation and Evolution of Galaxies Within Merging Dark Matter Haloes. *MNRAS*, 264:201, September 1993.

G. Kauffmann, T. M. Heckman, S. D. M. White, *et al.* The dependence of star formation history and internal structure on stellar mass for 10^5 low-redshift galaxies. *MNRAS*, 341:54–69, May 2003. doi: 10.1046/j.1365-8711.2003.06292.x.

D. Kawata and J. S. Mulchaey. Strangulation in Galaxy Groups. *ApJL*, 672:L103–L106, January 2008. doi: 10.1086/526544.

S. Kazantzidis, L. Mayer, C. Mastropietro, *et al.* Density Profiles of Cold Dark Matter Substructure: Implications for the Missing-Satellites Problem. *ApJ*, 608:663–679, June 2004. doi: 10.1086/420840.

M. Kilbinger, L. Fu, C. Heymans, *et al.* CFHTLenS: combined probe cosmological model comparison using 2D weak gravitational lensing. *MNRAS*, 430:2200–2220, April 2013. doi: 10.1093/mnras/stt041.

L. J. King, N. Jackson, R. D. Blandford, *et al.* A complete infrared Einstein ring in the gravitational lens system B1938 + 666. *MNRAS*, 295:L41, April 1998. doi: 10.1046/j.1365-8711.1998.295241.x.

T. D. Kitching, L. Miller, C. E. Heymans, L. van Waerbeke, and A. F. Heavens. Bayesian galaxy shape measurement for weak lensing surveys - II. Application to simulations. *MNRAS*, 390:149–167, October 2008. doi: 10.1111/j.1365-2966.2008.13628.x.

M. Kleinheinrich, P. Schneider, H.-W. Rix, *et al.* Weak lensing measurements of dark matter halos of galaxies from COMBO-17. *A&A*, 455:441–451, August 2006. doi: 10.1051/0004-6361:20042606.

A. Klypin, A. V. Kravtsov, O. Valenzuela, and F. Prada. Where Are the Missing Galactic Satellites? *ApJ*, 522:82–92, September 1999. doi: 10.1086/307643.

J.-P. Kneib, R. S. Ellis, I. Smail, W. J. Couch, and R. M. Sharples. Hubble Space Telescope Observations of the Lensing Cluster Abell 2218. *ApJ*, 471:643, November 1996. doi: 10.1086/177995.

Benjamin P. Koester, Timothy A. McKay, James Annis, *et al.* MaxBCG: A Red Sequence Galaxy Cluster Finder. *The Astrophysical Journal*, 660:221–238, 2009.

Andrey V. Kravtsov, Oleg Y. Gnedin, and Anatoly A. Klypin. The tumultuous lives of galactic dwarfs and the missing satellites problem. *Astrophys.J.*, 609:482–497, 2004.

M. R. Krumholz, A. K. Leroy, and C. F. McKee. Which Phase of the Interstellar Medium Correlates with the Star Formation Rate? *ApJ*, 731:25, April 2011. doi: 10.1088/0004-637X/731/1/25.

R. Kuzio de Naray, S. S. McGaugh, and W. J. G. de Blok. Mass Models for Low Surface Brightness Galaxies with High-Resolution Optical Velocity Fields. *ApJ*, 676:920–943, April 2008. doi: 10.1086/527543.

R. Laureijs, J. Amiaux, S. Arduini, *et al.* Euclid Definition Study Report. *ArXiv e-prints*, October 2011.

A. Leauthaud, A. Finoguenov, J.-P. Kneib, *et al.* A Weak Lensing Study of X-ray Groups in the COSMOS Survey: Form and Evolution of the Mass-Luminosity Relation. *ApJ*, 709:97–114, January 2010. doi: 10.1088/0004-637X/709/1/97.

A. Leauthaud, J. Tinker, K. Bundy, *et al.* New Constraints on the Evolution of the Stellar-to-dark Matter Connection: A Combined Analysis of Galaxy-Galaxy Lensing, Clustering, and Stellar Mass Functions from z = 0.2 to z =1. *ApJ*, 744:159, January 2012a. doi: 10.1088/0004-637X/744/2/159.

A. Leauthaud, M. White, D. Schlegel, *et al.* Overview of New Results from the Stripe 82 Equatorial Field. In *American Astronomical Society Meeting Abstracts #219*, volume 219 of *American Astronomical Society Meeting Abstracts*, page 324.06, January 2012b.

I. H. Li and H. K. C. Yee. Finding Galaxy Groups in Photometric-Redshift Space: The Probability Friends-of-Friends Algorithm. *AJ*, 135:809–822, March 2008. doi: 10.1088/0004-6256/135/3/809.

M. Limousin, J. P. Kneib, S. Bardeau, *et al.* Truncation of galaxy dark matter halos in high density environments. *A&A*, 461:881–891, January 2007. doi: 10.1051/0004-6361: 20065543.

Y.-T. Lin, J. J. Mohr, and S. A. Stanford. K-Band Properties of Galaxy Clusters and Groups: Luminosity Function, Radial Distribution, and Halo Occupation Number. *ApJ*, 610:745–761, August 2004. doi: 10.1086/421714.

M. R. Lovell, V. Eke, C. S. Frenk, *et al.* The haloes of bright satellite galaxies in a warm dark matter universe. *MNRAS*, 420:2318–2324, March 2012. doi: 10.1111/j. 1365-2966.2011.20200.x.

Y. Lu, H. J. Mo, N. Katz, and M. D. Weinberg. On the origin of cold dark matter halo density profiles. *MNRAS*, 368:1931–1940, June 2006. doi: 10.1111/j.1365-2966.2006.10270.x.

A. D. Ludlow, J. F. Navarro, M. Boylan-Kolchin, *et al.* The mass profile and accretion history of cold dark matter haloes. *MNRAS*, 432:1103–1113, June 2013. doi: 10.1093/mnras/stt526.

A. V. Macciò, S. Paduroiu, D. Anderhalden, A. Schneider, and B. Moore. Cores in warm dark matter haloes: a Catch 22 problem. *MNRAS*, 424:1105–1112, August 2012. doi: 10.1111/j.1365-2966.2012.21284.x.

R. Mandelbaum, U. Seljak, R. J. Cool, *et al.* Density profiles of galaxy groups and clusters from SDSS galaxy-galaxy weak lensing. *MNRAS*, 372:758–776, October 2006a. doi: 10.1111/j.1365-2966.2006.10906.x.

R. Mandelbaum, U. Seljak, G. Kauffmann, C. M. Hirata, and J. Brinkmann. Galaxy halo masses and satellite fractions from galaxy-galaxy lensing in the Sloan Digital Sky Survey: stellar mass, luminosity, morphology and environment dependencies. *MNRAS*, 368:715–731, May 2006b. doi: 10.1111/j.1365-2966.2006.10156.x.

R. Mandelbaum, U. Seljak, and C. M. Hirata. A halo mass–concentration relation from weak lensing. *JCAP*, 8:6, August 2008. doi: 10.1088/1475-7516/2008/08/006.

C. Marinoni and M. J. Hudson. The Mass-to-Light Function of Virialized Systems and the Relationship between Their Optical and X-Ray Properties. *ApJ*, 569:101–111, April 2002. doi: 10.1086/339319.

C. Marinoni, M. J. Hudson, and G. Giuricin. The Optical Luminosity Function of Virialized Systems. *ApJ*, 569:91–100, April 2002.

C. L. Martin. Properties of Galactic Outflows: Measurements of the Feedback from Star Formation. *ApJ*, 513:156–160, March 1999. doi: 10.1086/306863.

S. P. Martin. A Supersymmetry Primer. In G. L. Kane, editor, *Perspectives on Supersymmetry*, page 1, 1998.

R. Massey, J. Rhodes, A. Leauthaud, *et al.* COSMOS: Three-dimensional Weak Lensing and the Growth of Structure. *ApJS*, 172:239–253, September 2007. doi: 10.1086/516599.

D. Merritt. Relaxation and tidal stripping in rich clusters of galaxies. I. Evolution of the mass distribution. *ApJ*, 264:24–48, January 1983. doi: 10.1086/160571.

L. Miller, T. D. Kitching, C. Heymans, A. F. Heavens, and L. van Waerbeke. Bayesian galaxy shape measurement for weak lensing surveys - I. Methodology and a fast-fitting algorithm. *MNRAS*, 382:315–324, November 2007. doi: 10.1111/j.1365-2966.2007.12363.x.

L. Miller, C. Heymans, T. D. Kitching, *et al.* Bayesian Galaxy Shape Measurement for Weak Lensing Surveys - III. Application to the Canada-France-Hawaii Telescope Lensing Survey. *ArXiv e-prints*, October 2012.

J. Miralda-Escude. Gravitational lensing by clusters of galaxies - Constraining the mass distribution. *ApJ*, 370:1–14, March 1991a. doi: 10.1086/169789.

J. Miralda-Escude. The correlation function of galaxy ellipticities produced by gravitational lensing. *ApJ*, 380:1–8, October 1991b. doi: 10.1086/170555.

B. Moore, N. Katz, G. Lake, A. Dressler, and A. Oemler. Galaxy harassment and the evolution of clusters of galaxies. *Nature*, 379:613–616, February 1996. doi: 10.1038/379613a0.

B. Moore, S. Ghigna, F. Governato, *et al.* Dark Matter Substructure within Galactic Halos. *ApJL*, 524:L19–L22, October 1999a. doi: 10.1086/312287.

B. Moore, T. Quinn, F. Governato, J. Stadel, and G. Lake. Cold collapse and the core catastrophe. *MNRAS*, 310:1147–1152, December 1999b. doi: 10.1046/j.1365-8711.1999.03039.x.

J. S. Mulchaey and A. I. Zabludoff. The Properties of Poor Groups of Galaxies. II. X-Ray and Optical Comparisons. volume 496, pages 73–+, March 1998. doi: 10.1086/305356.

P. Natarajan, G. De Lucia, and V. Springel. Substructure in lensing clusters and simulations. *MNRAS*, 376:180–192, March 2007. doi: 10.1111/j.1365-2966.2007.11399.x.

P. Natarajan, J.-P. Kneib, I. Smail, *et al.* The Survival of Dark Matter Halos in the Cluster Cl 0024+16. *ApJ*, 693:970–983, March 2009. doi: 10.1088/0004-637X/693/1/970.

J. F. Navarro, C. S. Frenk, and S. D. M. White. A Universal Density Profile from Hierarchical Clustering. *ApJ*, 490:493, December 1997. doi: 10.1086/304888.

Angelo F. Neto, Liang Gao, Philip Bett, *et al.* The statistics of CDm halo concentrations. *MNRAS*, 381(4):1450–1462, 2007. ISSN 1365-2966. doi: 10.1111/j.1365-2966.2007.12381.x.

M. Oguri and T. Hamana. Detailed cluster lensing profiles at large radii and the impact on cluster weak lensing studies. *MNRAS*, 414:1851–1861, July 2011. doi: 10.1111/j.1365-2966.2011.18481.x.

N. D. Padilla, C. Lagos, and S. A. Cora. Galaxy satellites; building blocks and the hierarchical clustering paradigm. *Boletin de la Asociacion Argentina de Astronomia La Plata Argentina*, 52:213–216, 2009.

T. Padmanabhan. *Theoretical Astrophysics - Volume 3, Galaxies and Cosmology.* December 2002.

T. Padmanabhan. *Structure Formation in the Universe.* Cambridge University Press, 1993.

L. C. Parker, M. J. Hudson, R. G. Carlberg, and H. Hoekstra. Mass-to-Light Ratios of Galaxy Groups from Weak Lensing. *ApJ*, 634:806–812, December 2005. doi: 10.1086/497117.

E. Pastor Mira, S. Hilbert, J. Hartlap, and P. Schneider. Probing the dark-matter halos of cluster galaxies with weak lensing. *A&A*, 531:A169, July 2011. doi: 10.1051/0004-6361/201116851.

Planck Collaboration, P. A. R. Ade, N. Aghanim, *et al.* Planck 2013 results. XVI. Cosmological parameters. *ArXiv e-prints*, March 2013.

E. Polisensky and M. Ricotti. Constraints on the dark matter particle mass from the number of Milky Way satellites. *PhRvD*, 83(4):043506, February 2011. doi: 10.1103/PhysRevD.83.043506.

A. Pontzen and F. Governato. How supernova feedback turns dark matter cusps into cores. *MNRAS*, 421:3464–3471, April 2012. doi: 10.1111/j.1365-2966.2012.20571.x.

William H. Press and Paul Schechter. Formation of galaxies and clusters of galaxies by self-similar gravitational condensation. *Astrophysical Journal*, 187:425–438, 1974.

Vicent Quilis, Ben Moore, and Richard Bower. Gone with the wind: the origin of S0 galaxies in clusters. *Science*, 288:1617–1620, 2000.

R. Reyes, R. Mandelbaum, J. E. Gunn, *et al.* Optical-to-virial velocity ratios of local disc galaxies from combined kinematics and galaxy-galaxy lensing. *MNRAS*, 425: 2610–2640, October 2012. doi: 10.1111/j.1365-2966.2012.21472.x.

D. O. Richstone. Collisions of galaxies in dense clusters. II - Dynamical evolution of cluster galaxies. *ApJ*, 204:642–648, March 1976. doi: 10.1086/154213.

A. S. G. Robotham, P. Norberg, S. P. Driver, *et al.* Galaxy and Mass Assembly (GAMA): the GAMA galaxy group catalogue (G^{3}Cv1). *MNRAS*, 416:2640–2668, October 2011. doi: 10.1111/j.1365-2966.2011.19217.x.

G. B. Rybicki and A. P. Lightman. *Radiative Processes in Astrophysics.* Wiley-VCH, 1986.

J. Schaye. Star Formation Thresholds and Galaxy Edges: Why and Where. *ApJ*, 609: 667–682, July 2004. doi: 10.1086/421232.

P. Schneider, C.S. Kochanek, G. Meylan, *et al. Gravitational Lensing: Strong, Weak and Micro: Saas-Fee Advanced Course 33.* Saas-Fee Advanced Courses. Springer, 2006. ISBN 9783540303107.

E. S. Sheldon, C. E. Cunha, R. Mandelbaum, J. Brinkmann, and B. A. Weaver. Photometric Redshift Probability Distributions for Galaxies in the SDSS DR8. *ApJS*, 201: 32, August 2012. doi: 10.1088/0067-0049/201/2/32.

P. Sikivie. Dark Matter Axions. *International Journal of Modern Physics A*, 25:554–563, 2010. doi: 10.1142/S0217751X10048846.

R. A. Skibba, F. C. van den Bosch, X. Yang, *et al.* Are brightest halo galaxies central galaxies? *MNRAS*, 410:417–431, January 2011. doi: 10.1111/j.1365-2966.2010.17452. x.

V. Springel, S. D. M. White, G. Tormen, and G. Kauffmann. Populating a cluster of galaxies - I. Results at $z = 0$. *MNRAS*, 328:726–750, December 2001. doi: 10.1046/j. 1365-8711.2001.04912.x.

V. Springel, T. Di Matteo, and L. Hernquist. Modelling feedback from stars and black holes in galaxy mergers. *MNRAS*, 361:776–794, August 2005a. doi: 10.1111/j. 1365-2966.2005.09238.x.

V. Springel, J. Wang, M. Vogelsberger, *et al.* The Aquarius Project: the subhaloes of galactic haloes. *MNRAS*, 391:1685–1711, December 2008. doi: 10.1111/j.1365-2966. 2008.14066.x.

Volker Springel, Simon D. M. White, Adrian Jenkins, *et al.* Simulating the joint evolution of quasars, galaxies and their large-scale distribution. *Nature*, 2005:629–636, 2005b.

S. H. Suyu and A. Halkola. The halos of satellite galaxies: the companion of the massive elliptical lens SL2S J08544-0121. *A&A*, 524:A94, December 2010. doi: 10. 1051/0004-6361/201015481.

V. Szebehely and E. Grebenikov. Theory of Orbits-The Restricted Problem of Three Bodies. *Astronomicheskii Zhurnal*, 46:459, 1969.

M. Takada. Subaru Hyper Suprime-Cam Project. In N. Kawai and S. Nagataki, editors, *American Institute of Physics Conference Series*, volume 1279 of *American Institute of Physics Conference Series*, pages 120–127, October 2010. doi: 10.1063/1.3509247.

D. S. Taranu, M. J. Hudson, M. L. Balogh, *et al.* Quenching star formation in cluster galaxies. *ArXiv e-prints*, November 2012.

J. E. Taylor and A. Babul. The evolution of substructure in galaxy, group and cluster haloes - I. Basic dynamics. *MNRAS*, 348:811–830, March 2004. doi: 10.1111/j.1365-2966.2004.07395.x.

R. Teyssier, A. Pontzen, Y. Dubois, and J. I. Read. Cusp-core transformations in dwarf galaxies: observational predictions. *MNRAS*, 429:3068–3078, March 2013. doi: 10.1093/mnras/sts563.

J. L. Tinker, M. R. George, A. Leauthaud, *et al.* The Correlated Formation Histories of Massive Galaxies and Their Dark Matter Halos. *ApJL*, 755:L5, August 2012. doi: 10.1088/2041-8205/755/1/L5.

B. M. Tinsley and R. B. Larson. Stellar population explosions in proto-elliptical galaxies. *MNRAS*, 186:503–517, February 1979.

C. A. Tremonti, T. M. Heckman, G. Kauffmann, *et al.* The Origin of the Mass-Metallicity Relation: Insights from 53,000 Star-forming Galaxies in the Sloan Digital Sky Survey. *ApJ*, 613:898–913, October 2004. doi: 10.1086/423264.

J. A. Tyson, G. P. Kochanski, and I. P. dell'Antonio. Detailed Mass Map of CL 0024+1654 from Strong Lensing. *ApJ*, 498:L107, May 1998. doi: 10.1086/311314.

A. Vale and J. P. Ostriker. Linking halo mass to galaxy luminosity. *MNRAS*, 353: 189–200, September 2004. doi: 10.1111/j.1365-2966.2004.08059.x.

G. van de Ven, R. Mandelbaum, and C. R. Keeton. Galaxy density profiles and shapes - I. Simulation pipeline for lensing by realistic galaxy models. *MNRAS*, 398:607–634, September 2009. doi: 10.1111/j.1365-2966.2009.15167.x.

F. C. van den Bosch, D. Aquino, X. Yang, *et al.* The importance of satellite quenching for the build-up of the red sequence of present-day galaxies. *MNRAS*, 387:79–91, June 2008. doi: 10.1111/j.1365-2966.2008.13230.x.

E. van Uitert, H. Hoekstra, M. Velander, *et al.* Galaxy-galaxy lensing constraints on the relation between baryons and dark matter in galaxies in the Red Sequence Cluster Survey 2. *A&A*, 534:A14, October 2011. doi: 10.1051/0004-6361/201117308.

S. Vegetti, L. V. E. Koopmans, A. Bolton, T. Treu, and R. Gavazzi. Detection of a dark substructure through gravitational imaging. *MNRAS*, 408:1969–1981, November 2010. doi: 10.1111/j.1365-2966.2010.16865.x.

M. Velander, E. van Uitert, H. Hoekstra, *et al.* CFHTLenS: The relation between galaxy dark matter haloes and baryons from weak gravitational lensing. *ArXiv e-prints*, April 2013.

G. Verdoes Kleijn, J. T. A. de Jong, E. A. Valentijn, *et al.* Astro-WISE for KiDS survey production and quality control. *ArXiv e-prints*, December 2011.

M. Viel, G. D. Becker, J. S. Bolton, and M. G. Haehnelt. Warm dark matter as a solution to the small scale crisis: New constraints from high redshift Lyman-α forest data. *PhRvD*, 88(4):043502, August 2013. doi: 10.1103/PhysRevD.88.043502.

R. H. Wechsler, J. S. Bullock, J. R. Primack, A. V. Kravtsov, and A. Dekel. Concentrations of Dark Halos from Their Assembly Histories. *ApJ*, 568:52–70, March 2002. doi: 10.1086/338765.

A. R. Wetzel, J. L. Tinker, C. Conroy, and F. C. van den Bosch. Galaxy evolution in groups and clusters: satellite star formation histories and quenching time-scales in a hierarchical Universe. *MNRAS*, 432:336–358, June 2013. doi: 10.1093/mnras/stt469.

Simon D. M. White. Formation and Evolution of Galaxies: Les Houches Lectures. *ArXiv Astrophysics e-prints*, 2009.

B. Willman. In Pursuit of the Least Luminous Galaxies. *Advances in Astronomy*, 2010: 285454, 2010. doi: 10.1155/2010/285454.

X. Yang, H. J. Mo, and F. C. van den Bosch. Constraining galaxy formation and cosmology with the conditional luminosity function of galaxies. *MNRAS*, 339:1057–1080, March 2003. doi: 10.1046/j.1365-8711.2003.06254.x.

X. Yang, H. J. Mo, F. C. van den Bosch, Y. Zhang, and J. Han. Evolution of the Galaxy-Dark Matter Connection and the Assembly of Galaxies in Dark Matter Halos. *ApJ*, 752:41, June 2012. doi: 10.1088/0004-637X/752/1/41.

D. H. Zhao, H. J. Mo, Y. P. Jing, and G. Börner. The growth and structure of dark matter haloes. *MNRAS*, 339:12–24, February 2003. doi: 10.1046/j.1365-8711.2003.06135.x.

Appendix A

Approximations Used

A.1 Deriving Halo Mass from Stellar Mass

In Section 2.2.2.1, we found it necessary to estimate the mass of a galaxy's dark matter halo, given its stellar mass. While Equation (2.3) can be easily used to estimate a galaxy's stellar mass if its halo mass is known, the equation is not invertible. We accomplish our task of estimating M_{halo} through an iterative process:

1. Begin with an estimate of the galaxy's halo mass, M_{init}. For this, we use the M_{200} value for the galaxy given in De Lucia and Blaizot (2007)'s database.

2. Set M_{-1}, M_{-2}, M_{-3}, and M_{-4} all equal to M_{init}.

3. Set M_{test} equal to $(M_{-1} + M_{-2} + M_{-3} + M_{-4})/4$.

4. Determine M_{new} through:

$$M_{\text{new}} = \frac{M_{\text{stellar}}}{0.129} \left(\left(\frac{M_{\text{test}}}{10^{11.4} \ \text{M}_\odot} \right)^{-0.926} \right.$$
$$\left. + \left(\frac{M_{\text{test}}}{10^{11.4} \ \text{M}_\odot} \right)^{0.261} \right)^{2.44}. \tag{A.1}$$

5. If M_{new}, M_{-1}, M_{-2}, M_{-3}, and M_{-4} all differ by no more than 0.1%, return M_{new} as M_{halo}.

6. Set $M_{-4} = M_{-3}$, $M_{-3} = M_{-2}$, $M_{-2} = M_{-1}$, and $M_{-1} = M_{\text{new}}$

7. Repeat steps 3 to 6 until M has converged, for a maximum of 1,000 loops

8. If M has not converged, return M_{init} as M_{halo}

The use of multiple past estimates of M_{halo} in our code was found to be necessary in order to ensure convergence, as when fewer past estimates were averaged and used, the algorithm would often end up alternating between two vastly different estimates for M_{halo}. With the algorithm as written, M_{halo} was found to converge in every case tested in a sample 4×4 deg.[2] field.

A.2 Altering Concentration of NFW Profiles to Preserve Cusp Distribution

In Section 2.2.2.1, we mentioned an alteration we made to the NFW mass profile which leaves the density profile unchanged near the centre, but is lower than the initial profile at large radii. To illustrate how this works, examine the formula for the NFW density profile, with δ_c, r_s, and x expanded:

$$\rho(x) = \frac{M_{200} * (\ln(1+c) - c/(1+c))^{-1}}{4\pi \left(\frac{r_{200}}{c}\right)^3} * \\ \frac{1}{\left(\frac{rc}{r_{200}}\right)\left(1 + \left(\frac{rc}{r_{200}}\right)\right)^2}. \tag{A.2}$$

In the limit $r \ll r_{200}/c$, this becomes:

$$\rho(x) = \frac{M_{200}}{4\pi r_{200}^2} \frac{1}{r} \frac{c^2}{\ln(1+c) - c/(1+c)}. \tag{A.3}$$

Since we modify the NFW profile by introducing a scale factor f_r to the profile and modifying c, Equation (2.8) must be satisfied for the density in the core region to remain unchanged. As this equation is not solvable for c', we use the following approximation:

$$c' = 0.117lc^4 - 1.70lc^3 + 11.10lc^2 - 30.7lc + 32.8, \tag{A.4}$$

where:

$$lc = \ln\left(c^2 / \left((\ln(1+c) - c/(1+c)) * f_r\right)\right). \tag{A.5}$$

This approximation has less than 2% error for $3 < lc < 7$, as can be seen in Fig. A.1, which covers the range of lc possible for $4 < c < 15$ and $0.1 < f_r < 1$.
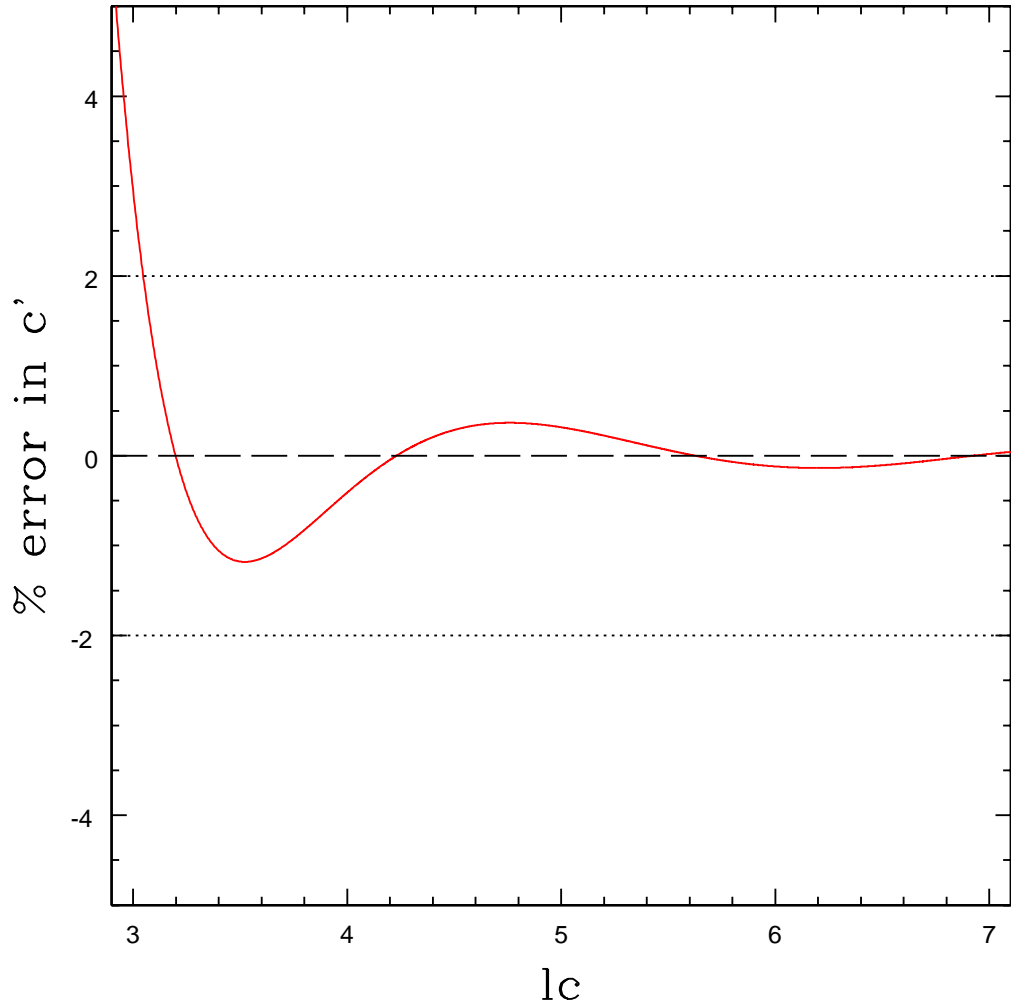
FIGURE A.1: Percentage error in our estimates of c', as calculated from Equation (A.4), as a function of lc (defined in Equation (A.5)). The error is less than 2% for all reasonable values for the group's initial concentration c and the fraction of mass f_r retained by the group's halo. Significant error is only seen for extremely low concentration haloes, which are not modeled in our simulations.

Appendix B

Preliminary SDSS DR8 Analysis

In this appendix we present a preliminary analysis of data from the Sloan Digital Sky Survey, Data Release 8 (Aihara et al., 2011, hereafter SDSS DR8) using the same methodology as outlined in Chapter 2. In Section B.1, we discuss the data used for this analysis, and in Section B.2, we present preliminary results from this analysis.

B.1 Data

B.1.1 Observations

The SDSS (Aihara et al., 2011) is the widest survey with full photometric ($ugriz$) imaging to date, with over 8,000 deg.^{2} imaged to a depth of $r \lesssim 21.8$, giving an effective ~ 3.6 sources per arcmin^2, for a total of $\sim 1.1 \times 10^8$ sources at a mean redshift of ~ 0.36. Photometric redshifts have been prepared for most galaxies detected to this depth by Sheldon et al. (2012) and made publicly available. The SDSS also includes spectroscopic redshift measurements for approximately one million objects. This spectroscopic sample is not large enough for the lensing analysis we wish to perform, but it does allow us to calibrate our photometric redshift and stellar mass estimates.

In Section B.1.1.1, we discuss how we prepare our lens sample from the SDSS, and in Section B.1.1.2, we discuss how we prepare our source sample.

B.1.1.1 Lens Sample

For our lens sample, we use all galaxies included in Sheldon et al. (2012)'s publicly-available photometric redshift catalogue, which comprises all galaxies with $r < 21.8$

which pass quality cuts. This results in approximately ~ 1.8 lenses per square arcmin, and $\sim 5.4 \times 10^7$ lenses total, at a mean redshift of 0.36, with typical photo-z error of $\sigma(z) \approx 0.12$.

We additionally require stellar mass estimates for our lens sample, which we estimate using the r-band magnitude (k-corrected to redshift 0), redshift, and colour of each galaxy. For each galaxy, we first calculate k-corrections using the publicly-available kcorrect v4.2 package (Blanton and Roweis, 2007). We then calculate a quantity l, proportional to the luminosity of the galaxy, defined as:

$$l = R\,[z(1+z)]^2\,, \tag{B.1}$$

where R is the k-corrected r-band magnitude of the galaxy converted to nanomaggies, and z is the redshift of the galaxy (spectroscopic if available, otherwise photometric). We divide the galaxies into samples of "red" (k-corrected $g-r > 0.8$) and "blue" (k-corrected $g-r \leq 0.8$) galaxies. This division between "red" and "blue" galaxies was based on an analysis of mass-to-light ratios from the subsample of galaxies for which stellar masses were available from the MPA/JHU group (Kauffmann et al., 2003, Tremonti et al., 2004, Brinchmann et al., 2004), in which it was found that the mass-to-light ratio showed a prominent change in relationship at $g-r \sim 0.8$. Using this information, we then apply the following formulae to estimate the galaxies' stellar masses:

$$\text{Red} : \log(m) = 8.90 + 0.761\log(l) + 2.265(g-r)$$
$$\text{Blue} : \log(m) = 7.69 + 0.799\log(l) + 3.839(g-r), \tag{B.2}$$

where $g-r$ is the k-corrected $g-r$ colour of the galaxy and m is its stellar mass in units of $M_\odot$. We determined these formulae through linear regressions, comparing our l and colours with the stellar mass estimates of the MPA/JHU group for the subset of galaxies in our sample with spectroscopic redshifts. The $g-r$ colour was found to give the best correlation ($R^2 = 0.7850(\text{Red}), 0.9001(\text{Blue})$) when used in combination with l, so it is used in our formulae. For the sample of spectroscopic galaxies, these formulae have negligible bias ($< 10^{-6}$ in log-space) and scatter of $\sigma(\log(m)) \sim 0.11(\text{Red}), 0.19\text{Blue}$.

B.1.1.2 Source Sample

We select our source sample from the SDSS DR8 in the same manner as detailed in Appendix A of Reyes et al. (2012). In summary, we select galaxies which:

- Are not likely to be misidentified stars or cosmic rays.

- Have a 5σ detection in either the i- or r-band

- Do not have significant problems that would prohibit accurate shear measurement (eg. saturated or masked pixels)

In order to calculate ellipticities for sources, we apply the following procedure, based on the algorithms outlined by Bernstein and Jarvis (2002). All variable names in square brackets refer to columns in the "Galaxies" context of the SDSS DR8, and their meanings are explained in detail at http://www.sdss3.org/dr8/algorithms/classify.php#photo_adaptive:

1. For the r-band, calculate resolution R_r from the sum of second-order moments and the fourth-order moment for the measurement and point-spread function (PSF) of the observation as:

$$R_r = 1 - \frac{[\texttt{mRrCcPSF\_r}] * (4 - [\texttt{mCr4PSF\_r}])/[\texttt{mCr4PSF\_r}]}{[\texttt{mRrCc\_r}] * (4 - [\texttt{mCr4\_r}])/[\texttt{mCr4\_r}]}. \tag{B.3}$$

2. Correct $e'_{1,r}$ and $e'_{2,r}$ for the PSF by:

$$e'_{1,r} = ([\texttt{mE1\_r}] - R_r * [\texttt{mE1PSF\_r}]) / (1 - R\_r)$$
$$e'_{2,r} = ([\texttt{mE2\_r}] - R_r * [\texttt{mE2PSF\_r}]) / (1 - R\_r) \tag{B.4}$$

3. Calculated the weight for the r-band measurement as its inverse-square variance:

$$W_r = \frac{(1 - R_r)^2}{[\texttt{mE1E1Err\_r}]^2 + [\texttt{mE2E2Err\_r}]^2} \tag{B.5}$$

4. Repeat the above steps for the i-band.

5. Combine the r- and i-band measurements as:

$$e'_1 = \frac{e'_{1,r} W_r + e'_{1,i} W_i}{W_r + W_i}$$
$$e'_2 = \frac{e'_{2,r} W_r + e'_{2,i} W_i}{W_r + W_i} \tag{B.6}$$

The above procedure gives (e'_1, e'_2) in the coordinates of the CCD it was detected with. In order to rotate to the RA-Dec frame of reference, we use the astrometry for the galaxy's position and a position shifted by one pixel in the "x" direction of the CCD with the equations detailed at http://www.sdss3.org/dr8/algorithms/astrometry.php#eqn to determine the proper rotation angle ϕ. We then rotate (e'_1, e'_2) by 2ϕ to determine

(e_1, e_2) in the RA-Dec frame of reference. These rotations were tested and confirmed by visual inspection of a sample of galaxies.

We then supplement our source catalogue with redshift information, using the following priority:

1. If spectroscopic redshifts are available, those are preferentially used ($< 1\%$ of sources)

2. Otherwise, if the galaxy is in Sheldon et al. (2012)'s photo-z catalogue, we use that estimate ($\sim 80\%$ of sources)

3. Otherwise, we estimate the galaxy's redshift using the publicly-available code BPZ (Benítez, 2000) for photo-z estimation (Remaining $\sim 20\%$ of sources).

Through comparing redshift estimates from BPZ to spectroscopic redshifts for the subset of galaxies where spectro-zs are available, we found that the estimates from BPZ had a notable bias relative to the spectro-zs. We therefore apply an empirical correction to all redshifts estimated with BPZ:

$$z_{new} = -0.0211 + 0.8356 * z_{\mathrm{BPZ}}. \qquad (B.7)$$

This correction results in negligible bias between the photo-z estimate and typical error of $\sigma_z \approx 0.07$ for the subset of galaxies with spectroscopic redshifts. The mean photo-z error for all sources is ~ 0.12.

B.1.2 Catalogue Analysis

Fig. B.1 shows the distributions of stellar mass and redshift for the HDE and LDE samples of lens galaxies in the SDSS DR8. As is the case with the CFHTLenS dataset, the matching scheme results in a nearly identical distribution of stellar masses for HDE and LDE galaxies, and a very similar distribution of redshifts.

Table B.1 shows statistics for lens galaxies in the HDE and LDE samples in the SDSS DR8. While we use a different method to determine whether galaxies are red or blue here compared to with the CFHTLenS (Here, galaxies with $g - r > 0.8$ are red, and the rest are blue), the overall trend is the same: The red fraction increases with increasing stellar mass, and the HDE sample has a higher fraction of red galaxies than does the LDE sample.

Fig. B.2 shows the distributions of galaxy types for the mock HDE and LDE samples drawn from the Millennium Simulation, simulating the SDSS DR8 photometry and
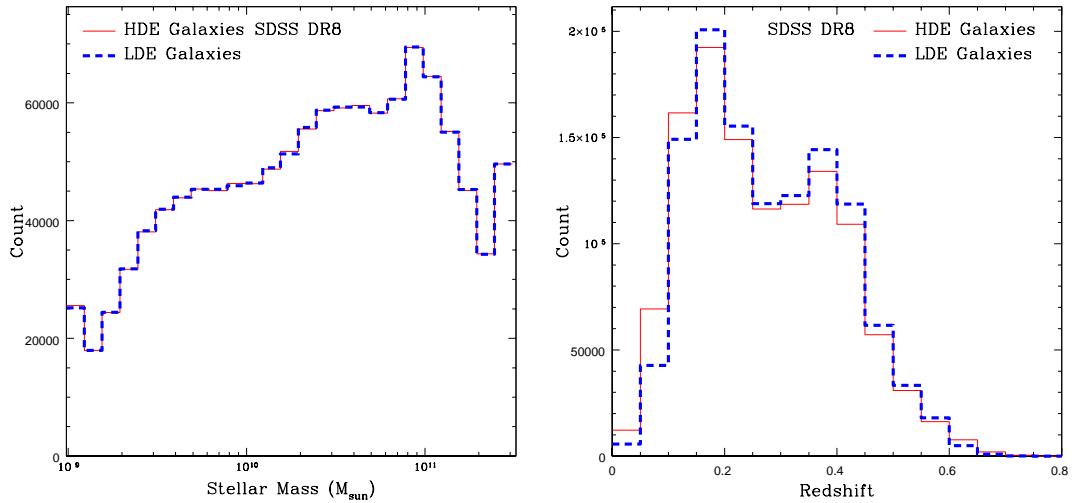
FIGURE B.1: The distributions of stellar mass (left) and redshift (right) for the samples of HDE (solid line) and LDE (dashed line) galaxies in the SDSS DR8 catalogues, which, because of our matching algorithm, are virtually identical. The redshift distributions differ slightly between HDE and LDE galaxies, but there is no apparent trend to the deviation.

SDSS DR8					
		HDE		LDE	
$\log m$	$\overline{z}$	f_{red}	f_{blue}	f_{red}	f_{blue}
9–9.5	0.17	0.01	0.99	0.01	0.99
9.5–10	0.21	0.06	0.94	0.05	0.95
10–10.5	0.23	0.54	0.46	0.50	0.50
10.5–11	0.24	0.95	0.05	0.94	0.06
11–11.5	0.27	1.00	0.00	1.00	0.00
9–10.5	0.22	0.40	0.60	0.38	0.62

TABLE B.1: Statistics of galaxies in various stellar mass bins in the SDSS DR8, as a function of environment. $\overline{z}$ is the mean redshift of the bin. f_{red} is the fraction of galaxies that are red ($g - r > 0.8$), and f_{blue} is the fraction that are blue ($g - r \leq 0.8$). All average values and fractions assume galaxies are weighted by their stellar masses.

spectra, and, for the satellite galaxies within each sample, the distribution of the masses of the groups in which they reside. Table B.2 shows the distributions of galaxy types for the HDE and LDE samples for various stellar mass bins. As was the case with the simulated CFHTLenS dataset, the fraction of satellites in the HDE sample remains roughly constant with stellar mass and decreases slightly with stellar mass in the LDE sample. For both samples, the fraction of centrals rises with stellar mass, while the fraction of field galaxies falls. No sample shows any significant change with stellar mass in the mean mass of the host groups for satellites. HDE satellites are observed to reside in groups of $\sim 9.3 \times 10^{13}$ $M_{\odot}$. In contrast, for the small fraction of LDE galaxies that are satellites, the characteristic host halo mass is $\sim 3.3 \times 10^{13}$ $M_{\odot}$. These host-group masses are a factor of ~ 2 greater than the host-group masses found for satellites in
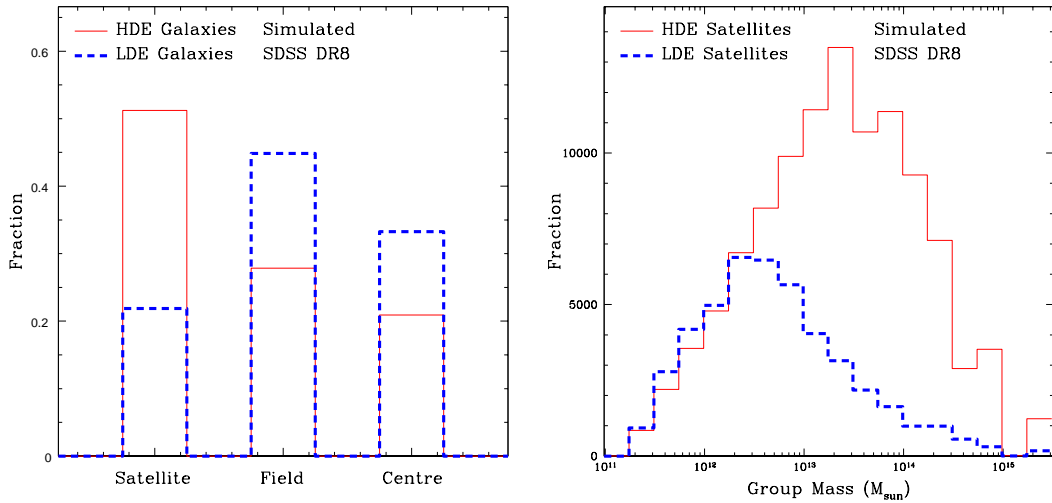
FIGURE B.2: The distributions of the types of galaxies classified as HDE and LDE in the simulations (left), and, of those classified as satellites, the distributions of the masses of the groups in which they reside (right). Plots assume detection limits and photo-z quality similar to the SDSS DR8.

			Simulated SDSS DR8								
			HDE				LDE			
$\log m$	$\overline{M}$	$\overline{z}$	f_{sat}	f_{field}	f_{cen}	$\overline{M_{host}}$	f_{sat}	f_{field}	f_{cen}	$\overline{M_{host}}$
9–9.5	17	0.17	0.49	0.46	0.05	13000	0.23	0.70	0.07	4800
9.5–10	32	0.26	0.52	0.32	0.16	11000	0.23	0.52	0.25	3100
10–10.5	81	0.34	0.56	0.14	0.30	8500	0.21	0.26	0.53	3100
10.5–11	400	0.37	0.46	0.03	0.51	10000	0.17	0.08	0.76	4400
9–10.5	65	0.31	0.55	0.20	0.25	9300	0.22	0.35	0.43	3300

TABLE B.2: Statistics of galaxies in the Millennium simulation for various stellar mass bins, using our models for estimating halo mass and environment, and assuming similar detection limits and photo-z quality to the SDSS DR8. $\log m$ is the stellar mass bin. $\overline{M}$ is the mean halo mass of the galaxies in this bin in units of $10^{10} M_{\odot}$, and $\overline{z}$ is their mean redshift. f_{sat}, f_{field}, and f_{cen} are the fractions of galaxies that are satellites, field galaxies, and group centrals, respectively. $\overline{M_{host}}$ is the mean mass of the host group for satellite galaxies in units of $10^{10} M_{\odot}$. All values assume galaxies are weighted by their stellar masses.

the CFHTLenS catalogue. This is likely a result of the poorer photometry in the SDSS DR8 as compared to the CFHTLenS; satellites within poorer groups are less likely to be in our HDE sample than they would if the photometry were better, resulting in an increased mean host-group mass.
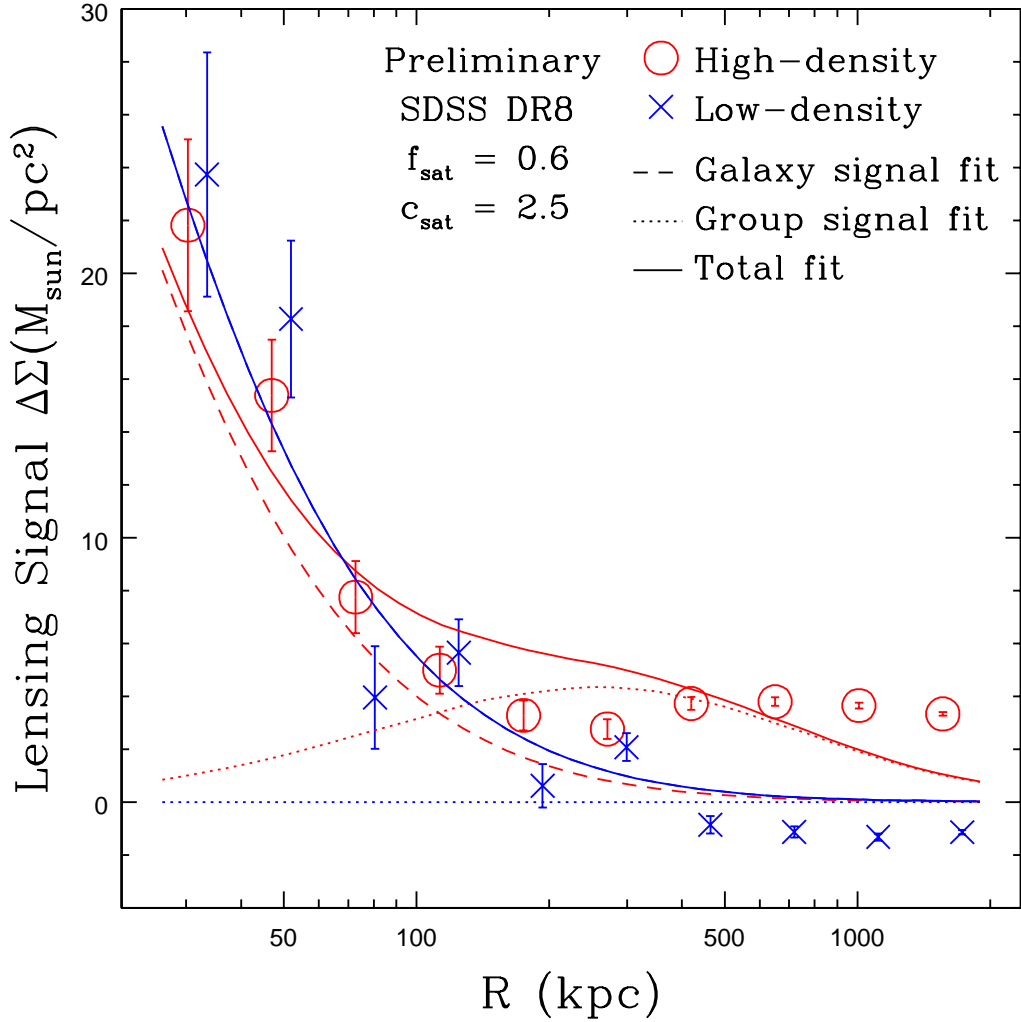
FIGURE B.3: Measured lensing signal and model fits for data from the SDSS DR8, including all galaxies with $10^9 < m < 10^{10.5} M_\odot$. HDE (red) and LDE (blue) lensing signals and fits are illustrated, as well as the HDE data with the fitted offset-group-halo term subtracted off (green). The dashed line shows the one-halo model fit to the HDE sample, and the dotted line shows the HDE offset-group-halo term. The one-halo mass fit for the HDE sample is found to be lower than for the LDE sample.

B.2 Preliminary Results

Fig. B.3 shows the lensing signals for the HDE and LDE samples taken from the SDSS DR8, including all galaxies with $10^9 M_\odot < m < 10^{10.5}\ M_\odot$, with the best-fit models plotted on top. For this broad mass bin, the fits show that the HDE one-halo term is lower than the LDE term, at 1.65σ significance ($p = 0.0979$). However, while the LDE model is a decent fit to the data ($\chi^2_{\rm red} = 1.60$), the HDE model is a very poor fit ($\chi^2_{\rm red} = 15.4459$, due primarily to a poor fit of the offset group halo). More work will be required to determine the reason for this. Some possible explanations include:

- Our model does not include the two-halo component, which is more important for this sample, as the offset group halo term does not dominate it to the same extent that it does in the CFHTLenS.

- Our model for the offset group halo term may not be appropriate for this sample. In particular, the term $P_{HDE}(R_s)$ used in Equation (2.16), representing the probability that a satellite will be included in our HDE sample, may need to be modeled in a different manner for this sample. We previously assumed a relatively sharp cut-off in the probability, but with the poorer photo-zs of the SDSS DR8, a much shallower cut-off may be more appropriate.

- Our estimated fraction of galaxies in the HDE sample which are satellites (0.55 for the stellar mass range illustrated here) may be an overestimate. A test fit with a fraction of 0.2 had a much better $\chi^2_{red} = 2.19$, which may indicate that our simulated data overestimates the fraction of galaxies which are satellites.

Further investigation will be necessary to determine which, if any, of these scenarios is the case.

In addition, there are various other tasks that need to be performed in order to optimize and properly analyse our results, including:

- Applying an appropriate weighting scheme to our source sample.

- Applying a weighting scheme to all lens-source pairs based on the probability that the source in fact lies at a higher redshift than the lens.

- Investigating the predicted lensing signals for the HDE and LDE samples with simulated galaxy catalogues.

- Testing fits to the HDE sample using alternative satellite fractions and concentrations.

- Testing alternative fits to the HDE sample, to see if it is better fit by a change in one-halo concentration or truncation radius.

Once these tasks have been completed, the SDSS dataset will provide a useful test of the results presented in the thesis. The significance of a result from it may not be as strong as with the CFHTLenS, but when used in combination with the CFHTLenS data, it can still potentially improve the significance of the detection presented here.